Ultrafast Magnetization dynamics of magnetic nanostructures

Hasan Kesserwan

UNIVERSITÉ DE STRASBOURG

THESE

Pour obtenir le titre de

DOCTEUR DE L'UNIVERSITE DE STRASBOURG

Spécialité

PHYSIQUE DE LA MATIERE CONDENSEE

Présentée par

KESSERWAN HASAN

Dynamique d'aimantation ultra-rapide de nanostructures magnétiques

Directeur de Thèse : BIGOT Jean-Yves

Soutenue le 08 Juillet 2011 devant le Jury composé de :

Jean Oberlé	Rapporteur externe
Christophe Petit	Rapporteur externe
Pierre Gilliot	Examinateur interne
Valérie Halté	Invité
Giovanni Manfredi	Invité

to the greatest fathers and mother...
to him who is coming soon...
trying to do my best to be with him...
I present this work ...

Acknowledgements

A simple "thank you" word will never be sufficient to express my great feelings of gratitude to my PhD thesis supervisor *Jean-Yves Bigot*. Thank you for offering this valuable chance to perform my PhD studies under your worthful and precious supervision. Thank you for you efforts, scientific instructions and discussions that you provided me with in order to well achieve my Thesis.

I am also grateful to thank *Valérie Halté*. You Know Valérie it is always difficult to talk about respectful and kind persons in simple words. Valérie helped me to do my first studies in femto−magnetism in 2008, so I owe her a super thank you. I would never forget the scientific discussions that we had, and her support and encouragement during these three years.

I feel indebted to *Giovanni Manfredi*, who helped me to realize the theoretical part of my thesis. *Giovanni* always supported me with valuable instructions about numerical simulations. Also, I would like to thank *Paul-Antoine Hervieux* for his efforts during this theoretical work.

Amani and *Hélène* or *Hélène* and *Amani*, it was so advantageous to have discussed with you a wide variety of scientific as well as non-scientific issues. Thanks a lot for your help to prepare the French report of my PhD thesis.

Thanks for my teammates in FEMTOMAG team: *Mircea*, *Michèle*, *Marie*, *Monica* and *Jiwan*. Thanks for all the technical staff at the IPCMS who helped me to achieve my PhD studies.

And then, great thanks to my parents *Mahmoud* and *Amena*, my fiancee *Zeinab*, my parents Im *Hasan* and Abu *Hasan*, my brothers

(*Ali*, *Hussein*, *Ahmed* and the lovely *Mouhammad*), to my single sister *Zahraa* and to all my family.
To thank her in two lines is a difficult task since about her, my words clash with my feelings. I might say, many persons may give you many thing, but only a warm heart can give you everything. *Zeinab* my warm heart thanks for your encouragement and your beautiful presence in my life.
More Profoundly, thanks to *Hussein*, who is always ready to support, encourage and overall to help me to accomplish jobs and tasks that I should do it.
Special thanks to each and every one of my friends for the good moments that we had together including: *Mostafa Rizk*, *Hussein Hijazei*, *Mouhammad Haidar*, *Ali Hameih*, *Ali Hallal* and his wife *Fatima*, *Abed Ghaddar*, *Ali Jaafar*, *Mouhammad khalil*, *Mouhammad Hameih*, *Wassem Jaber* and *Mouhammad Mokadam*.
In the memory of my friend *Hussein Alzagheer* .
I will end up with a grateful to thank to sir *Mahdi Hasan Ali* with my sincere hopes to see him as soon as possible.

Contents

List of Figures

Chapter 1

Introduction

Many years later after the primary discussions on magnetism, Orsted in the nineteenth century did the first serious progress toward the understanding of magnetism where he discovered that an electric current generates a magnetic field (Fowler [1997]). Since then, the phenomenon of magnetism was intensively tackled from the theoretical side by different scientists like Gauss, Maxwell, Faraday. However, the proper description of magnetism arrived later on in the twentieth century with the work of Curie, Weiss, Bloch, Landau, Stoner, Néel, Brown ..... A description that opened the way for the application of magnetism in modern technology.

The physical origin of magnetism is related to the angular momentum as it is deduced from the famous Einstein-De Haas experiment "rotation by magnetization"(Einstein and De Haas [1915a,b]; Frenkel [1979]), and its inverse effect "magnetization by rotation"(Barnett [1915]).

It is evident that in magnetic materials, there exit two major sources of the angular moment :

- the orbiting electrons around the nucleus ⇒ orbital angular momentum.
- the magnetic moments or the spins ⇒ intrinsic angular momentum.

1.1 Types of Magnetic Materials

According to the alignment of the magnetic moments, the magnetic materials can be classified into different groups as illustrated on the following figure :

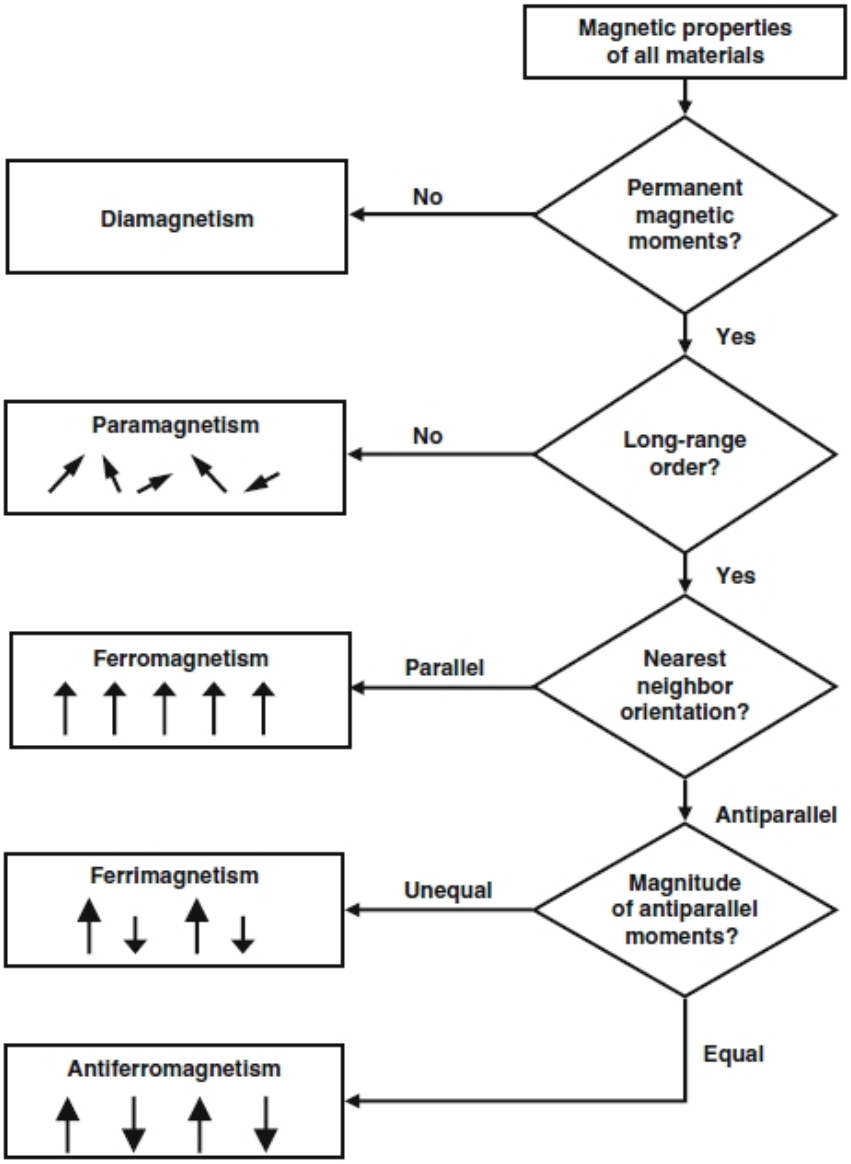

Figure 1.1: The major classifications of magnetic properties of media.(Stancil and Prabhakar [2009])

1.1.1 Diamagnetic Materials

Virtually, all the magnetic materials have a diamagnetic behavior, so it is believed that diamagnetism is a universal effect. The diamagnetic atoms do not have permanent magnetic moments because the electrons are paired, thus their magnetization arises only from the orbital angular momentum.
In an external applied magnetic field, the diamagnetic materials are magnetized in an opposite direction to the field. Such behavior is well described by the microscopic application of Lenz's law (Schmitt [2002]). Examples of diamagnetic materials are the noble metals: Copper, Gold, Silver.

1.1.2 Paramagnetic Materials

Paramagnetic materials' atoms have permanent magnetic moments. In an external magnetic field, these materials are magnetized in the direction of the field. However, as soon as the field is switched off the magnetic moments loose their alinement and become randomly oriented so that they produce a zero net total magnetization at thermal equilibrium. Supposing that all the magnetic moments are aligned, then the magnetization of the paramagnetic substance is given by the langevin function (Kittel [1986]) :

$$M = Ng\mu_B J \cdot L(x) \tag{1.1}$$

- N is the number of atoms per unit volume.
- total angular momentum.
- g the landé −factor.
- μ_B the Bohr magneton.
- L(x) is the langevin function

$$L(x) = \coth(x) - \frac{1}{x}$$

- x is the ratio of the Zeeman energy of the magnetic moment in the external field to the thermal energy K_BT :

$$x = \frac{g\mu_B JB}{K_BT}$$

At high temperatures, the paramagnetic magnetization is given by the Curie law

$$M = \frac{C}{T}H \tag{1.2}$$

where $C = \frac{Ng^2J(J+1)\mu_B^2}{3K_B}$ is the curie constant.
Examples of paramagnetic materials are : Magnesium, Lithium, Tungsten, Sodium.

1.1.3 Ferromagnetic Materials

Even in a zero applied magnetic field, a ferromagnetic material possesses a certain magnetization. This is well understood in terms of the concepts of the molecular field and the magnetic domains introduced by Weiss (Weiss [1907]).
The molecular field aligns the magnetic moments against the thermal fluctuations, so that they keep their directions and thus the materials remain magnetized. In the absence of an applied magnetic field, a ferromagnet is constituted of magnetic domains. Inside each domain, the magnetic moment are aligned parallel, so that the domain acts like a tiny magnet. As soon as an external magnetic field is applied, the magnetic domains align parallel to the field directions.
However, a ferromagnetic material will loose its magnetization above a critical temperature called the curie temperature T_c and therefore behaves as a paramagnet. Above T_c, the magnetization is given by the curie−weiss law (Kittel [1986]) :

$$M = \frac{C}{T - T_c}H. \tag{1.3}$$

where $C = \frac{g\mu BM_s(J+1)}{3K_B}$ and $T_c = \frac{\mu_B}{K_B}M_s$ with M_s being the saturation magnetization.
Due to their interesting magnetic properties such as the hysteresis behavior M(H), the ferromagnetic materials are widely used in the data storage industry. Exam-

ples of ferromagnetic materials are the transition metals: Nickel, Iron, Cobalt.

1.1.4 Why is it interesting to Study the Magnetization Dynamics ?

The magnetic materials are strongly present in our daily life due their wide applications in modern technology. They are everywhere and at different sizes from big magnets to nano−sized materials. As an astonishing example of big magnets is the maglev train put on rails by the Japanese in 1997 (see figure 1.2). This train is very fast, moving at 480 Km/hr.

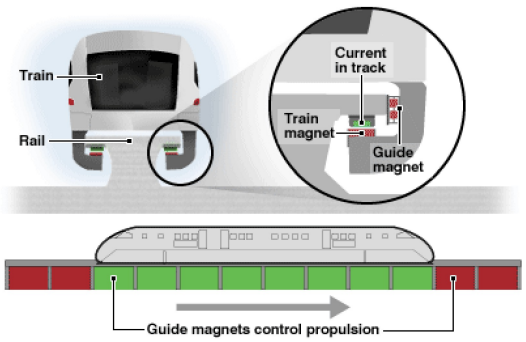

Figure 1.2: The Maglev train.(http://news.bbc.co.uk)

The magnetic nanostructures are used in many domains shown on figure 1.3, for example : in medicine for magnetic therapy, magnetic sensors, credit cards, most importantly in data storage. Especially, the magnetic nanoparticles have been receiving a remarkably increasing interest not only due to their significant application in modern nanotechnology but also for fundamental research.

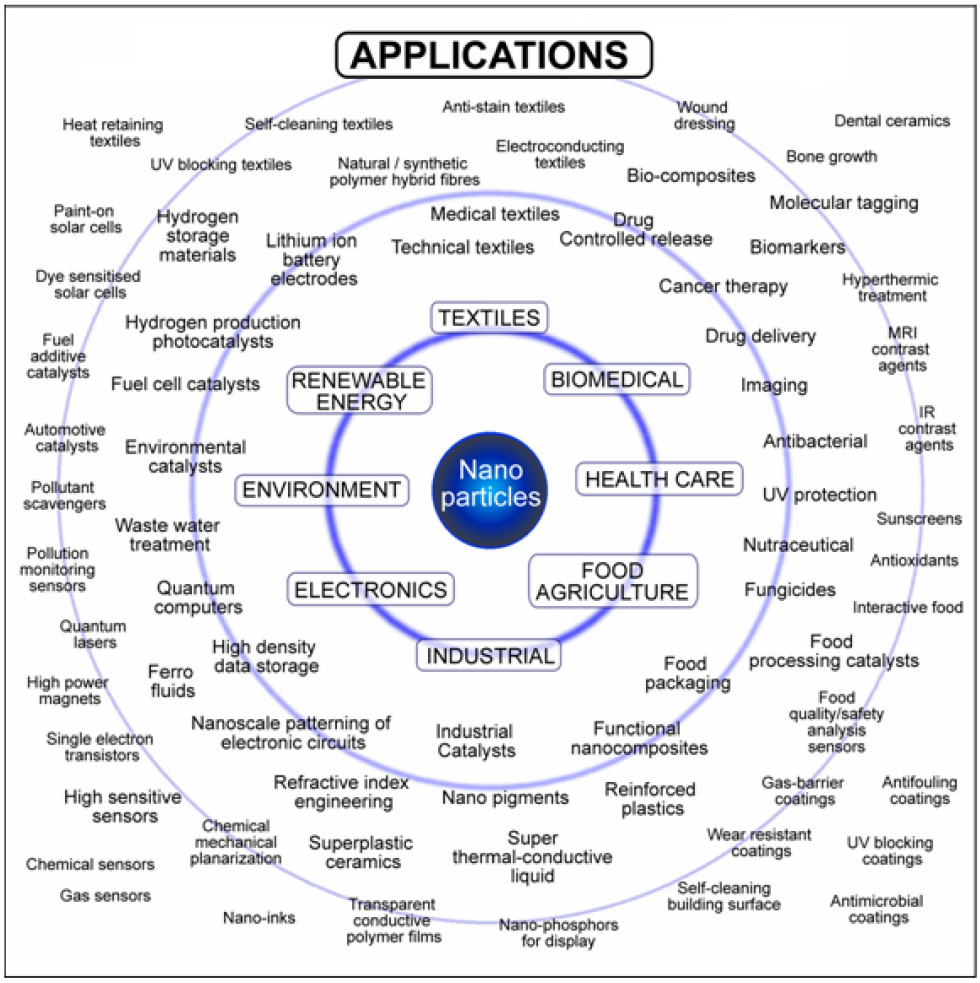

Figure 1.3: Scheme showing the different domains of applications of magnetic nanostructures.(http://www.deakin.edu.au)

In magnetic storage, a magnetic field is used to read or to write a magnetic data bit. The bit is a tiny magnetized region on the recording medium, conventionally labeled "1" or "0" depending on the direction of its magnetization. To write a bit, a strong local magnetic field is generated using an electric current traversing the coil (see figure 1.4) of the write head (Kleemann [2009]). This field modifies the patterns of the bit; more precisely it switches the direction of the magnetization from "1" to "0" and vice−versa. These modifications are detected

through the read head.

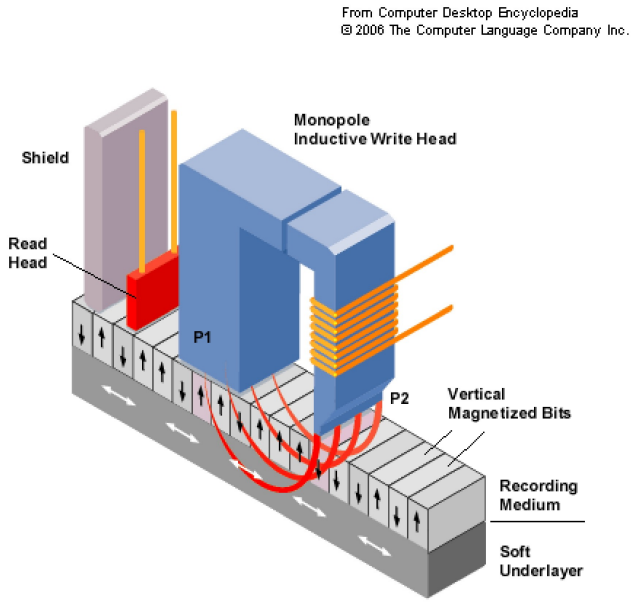

Figure 1.4: The read/write process.(Computer Desktop Encyclopedia), © 2006 The Computer Language Center Inc

However, it is reported that the frequency of the generated field pulse is limited to GHz (Acremann et al. [2000]; Devolder et al. [2006]; Gerrits et al. [2002]) corresponding to $\sim$ 1 ns reading time. Thus, future improvements of the speed of these processes (reading/writing) rely on the possibility to generate shorter and stronger magnetic fields.

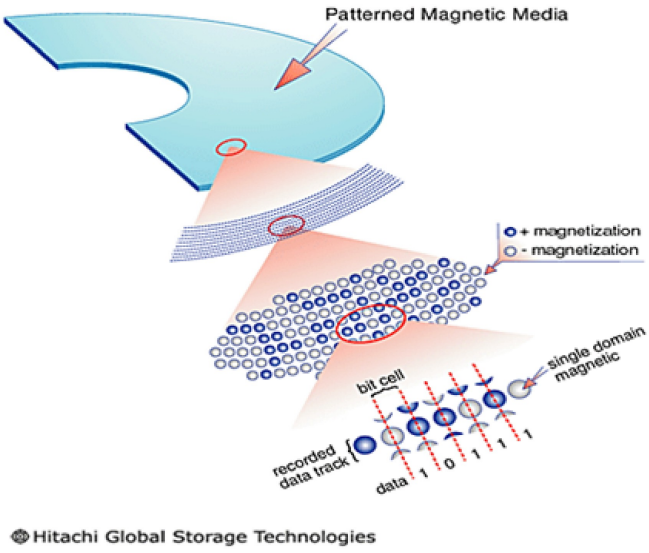

Figure 1.5: Nanoparticles−based data storage disc.(https://www1.hitachigst.com)

Concerning the the storing media, the use of magnetic nanoparticles promises to increase the data storage density to several petabits per square centimeter much more than the most advanced computer hard discs. Generally, the idea bases on the use of very small size magnetic nanoparticles (down to 1 nm diameter). However, with the continuous miniaturization in the size of the nanoparticles, the system is arriving at the limit where the stability of the magnetic information against the thermal effects becomes questionable. In other words, the particles will show a paramagnetic behaviour a phenomenon known as superparamgnetism (Brown [1963]; Néel [1949]).
Therefore, a detailed study of the ultrafast induced magnetization dynamics in magnetic nanoparticles is necessary. In fact, this a basic goal of the present work. Basically, what we call ultrafast induced magnetization dynamics includes all the changes in the magnetization of a given material induced with an intense femtosecond laser pulse taking place at very short time scales (1 fs − 1 ns). The characteristic time of these changes depends on the type of excitation, the material parameters as well as the spatial dimensions of the magnetic system.

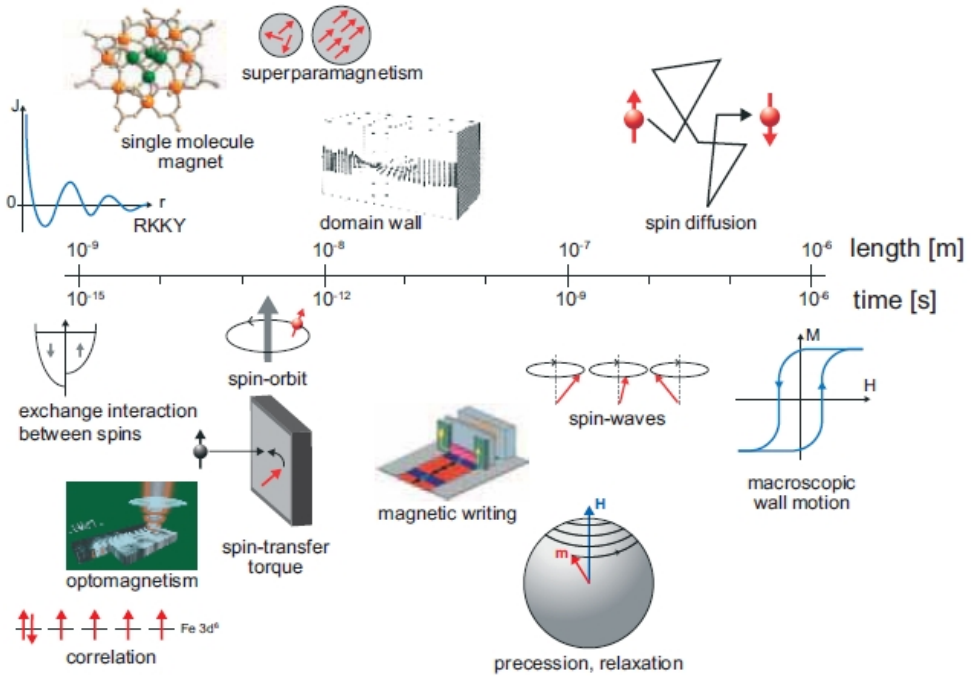

Figure 1.6: Different magnetic phenomena taking place at short time and space constants.

1.1.5 Femtosecond Spectroscopy

Since the famous experiment of 1996 performed in our team (Beaurepaire et al. [1996]), the Time Resolved Magneto−Optical Kerr Effect (TR−MOKE) in pump probe configuration or simply femtosecond spectroscopy continues to prove itself as an ultimate tool to study the magnetization dynamics in magnetic nanostructures. The femtosecond spectroscopy has the following advantages :

- Spatial resolution : for example, the confocal microscope developed in our group (Laraoui et al. [2007]), provides a spatial resolution of $\sim$ 300 nm giving the possibility to study individual magnetic nanoparticles.
- Temporal resolution : studying processes taking place at sub−100 fs time scales up to ns.(Guidoni et al. [2002])
- Spectral resolution : one can study the dynamics of magnetic structures

exciting and probing the materials as a function of wavelength, including the X-ray spectral range (Boeglin et al. [2010]).

1.2 This Thesis−Synopsis

In this thesis, we focused on the dynamics of phenomena like superparamagnetism and ferromagnetism in nanostructures. We also studied effects like annealing on the magnetism of nanoparticles. On the theoretical side we addressed interactions like the dipole−dipole interaction and the effect of anisotropy.
In the first part of the PHD, we performed Time Resolved Magneto-Optical Kerr Effect (TR-MOKE) measurements with 150 fs laser pulses at 400 nm pump and 800 nm probe to study the magnetization dynamics of Cobalt Platinum (CoPt) nanoparticles. The studied samples are 3D arrangements of $\sim$ 6.5 nm core/shell CoPt nanoparticles assembled into pellets where $\sim$ 5 nm Co nanoparticles resides at the core and is surrounded by $\sim$1.5 nm platinum shell. The samples are obtained by transmetalation processes (Park and Cheon [2001]).
Using the TR−MOKE spectroscopy, we are able to study the magnetization dynamics as well as the charge dynamics.
The general observed magnetization dynamics constitutes of an ultrafast demagnetization followed by a partial re−magnetization. Annealing the samples (heating up to 650 K), conducted a magnetic phase transition from superparamagnetism with a blocking temperature of 66 K into ferromagnetism with a blocking temperature above the room temperature (>350 K). On the annealed samples, the dynamical processes such as spin thermalization and relaxation are observed to be slower in comparison with the non annealed samples. On the long time scales, on these samples it is possible to induce a precession of the magnetization vector around the effective field. This precession did not exist on the non-annealed samples. The physical interpretations of the obtained results could be in general referred to the ferromagnetic nature of the annealed samples, or to the existence of the $CoPt_3$ particles or even to the enhanced dipolar interactions.
On the reflectivity measurements, both the non−annealed and the annealed samples showed an "ordinary" electron dynamics. To summarize briefly, after the laser excitation, the electrons are driven above the Fermi level, then they ther-

malize into a hot distribution due to electron-electron scattering processes, then they relax to the lattice via electron-phonon scattering processes, and finally the hot lattice diffuses its heat into the environment. During the relaxation process, we have reported $\sim$ 2 ps oscillation corresponding to the breathing mode of the individual nanoparticles.

On the non−annealed samples, we characterized a collective oscillation of the nanoparticles with a period of $\sim$ 146 ps interpreted as the supra−crystalline oscillations. We think that the supra−crystalline order is a local effect due to a mild annealing induced by the intense laser pulses. The oscillations disappeared when the samples were annealed indicating the existence of a disorder induced by the large temperature increase of the assembly of nanoparticles.

We devoted the second part of the thesis to the numerical simulations of the magnetization dynamics in superparamagnetic nanoparticles. In isolated single domain nanoparticles, the magnetization reversal by thermal activation is well described by the leading theoretical models of Stoner-Wohlfarth (Stoner and Wohlfarth [1948]) and Néel−Brown (Brown [1963]; Néel [1949]). According to this model, the magnetization of the nanoparticles spontaneously fluctuates from one equilibrium direction to another with a characteristic time given by an Arrhenius formula:

$$\frac{1}{\tau} = \frac{1}{\tau_0} exp\Big(- \frac{KV}{K_B T}\Big) \tag{1.4}$$

A question that we have addressed is to know what happens to the relaxation time when the interparticle dipolar interactions are included.

Actually, the effect of the dipolar interactions on the magnetization reversal processes in fine ferromagnetic nanoparticles (monodomains) is a debated question. Therefore, we have studied their effects on the magnetization dynamics of the nanoparticles. As our experimental results held significant signatures of a possible role of the dipolar interaction by suppressing the superparamagnetic effects.

In order to calculate the relaxation times of the magnetization reversal processes in isolated and interacting nanoparticles, we have solved numerically the Brown Fokker Planck equation (Brown [1963]) for magnetic nanoparticles with uniaxial anisotropy.

For the isolated nanoparticles, we have found that at low temperatures, the relax-

ation times are well described by the Arrhenius law provided by the Néel-Brown Model. However, for the interacting particles, deviations from this law are observed.
To account for the dipolar interactions, we have introduced a mean field approach where it is considered that each particle feels the average dipolar field due to the other nanoparticles. We have studied the effects of the interparticle distance and the density of the particles on the reversal process. In general we have found that the dipolar interactions tend to accelerate the reversal process in correspondence with other numerical results (Mørup and Elisabeth [1994]). Moreover, the numerical relaxation times are consistent with the experimentally measured values.

In summary, in this work our fundamental studies show that the core/shell CoPt nanoparticles are an interesting system to be used potentially as a data storage medium. We have shown that it is possible to suppress the effects of superparamagnetism on the spin dynamics in these systems simply by annealing them, inducing a ferromagnetic behavior at temperatures above 300 K. Also, we have shown that it is possible to order the nanoparticles in supra−crystalline assemblies using a mild laser annealing. These results stress out performing the time resolved femtosecond MOKE measurements to study the dynamical processes in magnetic nanostructures is a powerful technique.
For the numerical studies, we have introduced a simple and effective model to account for the dipolar interactions. Our results are consistent with the observed behaviour of interacting nanoparticles showing that the Brown-Néel stochastic approach allows understanding the main aspects of the magnetization dynamics for temporal scales when the spins are thermalized.

Chapter 2

Basic Facts

In this chapter, we present a general overview of the different physical models and concepts that form the physical background of the thesis.

2.1 Energy in a Magnetic system

The exchange energy, the magnetic anisotropy energy, the dipolar interaction energy , and the Zeeman energy are the main contributions in the total energy of a magnetic system.

2.1.1 Exchange Energy

To explain the ferromagnetic ordering, Pierre Weiss (Weiss [1907]) introduced the *Molecular field* or the Weiss field. However, the origin of the field remained obscure until 1928 (Heisenberg [1928]), when Heisenberg explained it to be due to the exchange of electrons among electronic levels. These interactions are of quantum origin and are called the exchange interactions. They have no analogue in classical mechanics .
It is well established in quantum mechanics that the total wave function of an electron has two parts : space and spin. Following the Pauli exclusion principle, the total wave function of an electron should be anti−symmetric. This shows that there are two possibilities for the space and spin parts of the wave function:

- A symmetric space wave function and an anti−symmetric spin one resulting in bringing closer the electrons and an anti−parallel alignment of the spins i.e. a singlet state.

$$\mid s,m\rangle :\mid 0,0\rangle = \frac{1}{\sqrt{2}}(\mid\uparrow\downarrow\rangle - \mid\downarrow\uparrow\rangle$$

- An anti−symmetric space wave function and a symmetric spin one resulting in a repulsion of the electrons and a parallel alignment of the spins i.e. a triplet state.

$$\mid s,m\rangle : \begin{cases} \mid 1,1\rangle = \mid\uparrow\uparrow\rangle \\ \mid 1,0\rangle = \frac{1}{\sqrt{2}}(\mid\uparrow\downarrow\rangle + \mid\downarrow\uparrow\rangle \\ \mid 1,-1\rangle = \mid\downarrow\downarrow\rangle \end{cases}$$

This splitting into singlets and triplets is due to the exchange interaction. For a system of N spins, the energy of the interactions is given by the Heisenberg Hamiltonian (Kittel [1986]):

$$E_{ex} = -\sum_{\substack{i,j \\ i\neq j}}^{N} J_{ij}\,\overrightarrow{S}_i \cdot \overrightarrow{S}_j \tag{2.1}$$

The indices *i,j* stand for the nearest neighbors. The constant J or the exchange integral, accounts for the magnitude of the splitting between the states. In other words, it reflects the energy associated with a change of quantum states between two electrons. J could be positive or negative. It can be shown that:

- **J**>0 : the spins are aligned parallel ⇒ ferromagnetic ordering.
- **J**<0 : the spins are aligned anti−parallel ⇒ anti−ferromagnetic ordering.

The exchange interaction is isotropic and does not impose any privileged direction of magnetization.

2.1.2 Magnetic Anisotropy energy

The magnetic anisotropy energy describes the dependence of the internal energy on the direction of spontaneous magnetization creating easy and hard axes. The total magnetization of a system will prefer to lie along the easy axis. Thus, the anisotropy energy could be defined as the energy it takes for a magnetization rotation from the easy axis to the hard one. Anisotropy can arise from several sources such as : electric field of the crystal, shape of the magnetic body, mechanical stress or strain, crystal symmetry....
Magneto−crystalline anisotropy favors magnetization along a particular crystallographic direction due to the spin-orbit coupling. Shape anisotropy favors magnetization within the plane of a thin film due to the long range dipolar coupling of magnetic moments.
The simplest forms of magnetic anisotropy are the uniaxial anisotropy and the cubic anisotropy.

2.1.2.1 Uniaxial Anisotropy

Uniaxial anisotropy is the existence of only one easy direction of magnetization. The corresponding energy is (Kittel [1986]):

$$E_{ani} = K_1 V sin^2\theta + K_2 V sin^4\theta \tag{2.2}$$

where $\mathbf{K}_1$ and $\mathbf{K}_2$ are the anisotropy constants and V is the volume. In the case of a ferromagnet K_2 is very small, then the energy reduces to:

$$E_{ani} = KV \sin^2\theta \tag{2.3}$$

N.B.: in the case of shape anisotropy $K = \frac{1}{2}\mu_0 M_s^2(N_x - N_z)$ where N_x and N_z are the components of the demagnetization tensor, where M_s is the saturation magnetization.

2.1.2.2 Cubic Anisotropy

In crystals with cubic symmetry, it happens that privileged directions of the magnetization exist. The anisotropy in this case is called the cubic anisotropy. The cubic anisotropy energy can be written in terms of the directions of the internal magnetization with respect to the three edges of the cubes in a ferromagnet (Kittel [1986]):

$$E_{ani} = KV(\alpha_1^2\alpha_2^2 + \alpha_2^2\alpha_3^2 + \alpha_3^2\alpha_1^2) \tag{2.4}$$

where $\alpha_1 = \sin\theta\cos\phi$,$\alpha_2 = \sin\theta\sin\phi$,$\alpha_3 = \cos\theta$,$\theta$ is the polar angle and ϕ the azimuthal angle.

2.1.3 Dipole-Dipole interaction energy

Unlike the exchange interaction, the dipole-dipole interaction (or the dipolar interaction) is anisotropic and has a long range behavior (Morrish [1966]). The dipolar interaction energy is :

$$E_d = \frac{1}{2}\sum_{\substack{i,j \\ i\neq j}}^{N}\left(\frac{\vec{m}_i \cdot \vec{m}_j}{r_{ij}^3} - \frac{3(\vec{m}_i \cdot \vec{r}_{ij})(\vec{m}_j \cdot \vec{r}_{ij})}{r_{ij}^5}\right) \tag{2.5}$$

where $\vec{r}_{ij} = |\vec{r}_i - \vec{r}_j|$ is the distance from the center of the i−th particle to the center of the j−th particle.

2.1.4 Zeeman energy

It is the energy of interaction between the magnetic moments and the external applied magnetic field :

$$E_z = -\mu_0 \vec{m} \cdot \vec{H}_0 \tag{2.6}$$

2.2 Single Domain nanoparticles

A ferromagnetic material in its demagnetized state is divided into a number of small regions called domains (Weiss [1907]). The magnetization directions of different domains need not be parallel. Domains are also present in other types

of materials such as anti−ferromagnetics, ferro−electrics....In a strong applied external magnetic field, the domain's magnetization rotates toward the direction of the field.(see figure 2.1)

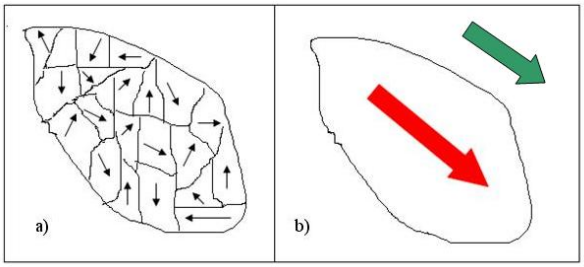

Figure 2.1: Domains and Domain walls: in absence of (a) and presence (b) of applied external magnetic field. For (b) the green arrow stands for the direction of the external applied field.

The domain structure in a ferromagnetic material comes out as a natural consequence of the various contributions to the energy: exchange energy and anisotropy energy. Actually, the origin of domains lies in the possibility of lowering the energy of a system by going from a saturated configuration with high magnetic energy to a domain configuration with a lower energy (Kittel [1986]) (figure 2.2).

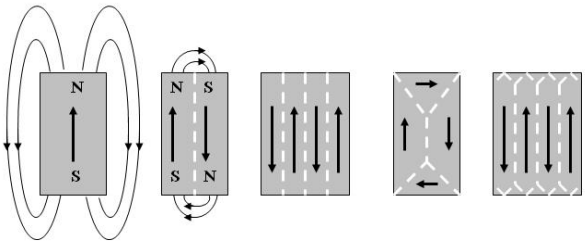

Figure 2.2: The origin of domains.

The smaller the size of magnetic materials is made, the simplest the domain structure is obtained so that below a critical size a particle of ferromagnetic materials is expected to consist of a single domain. A single domain particle or monodomain acts as a giant moment which depends on the volume, number of

atoms and type of materials of the particles.
The critical radius r_c below which a particle becomes a monodomain is estimated to be (Chikazumi and Charap [1964]):

$$r_c \approx \frac{9\sqrt{JK_u}}{\mu_0 M_s^2}. \tag{2.7}$$

where J is the exchange constant and K_u the uniaxial anisotropy constant, M_s: is saturation magnetization and μ_0 is the vacuum permeability.

2.3 Super-paramagnetism

As the size of ferromagnetic nanoparticles is reduced below 10 nm, the thermal energy K_BT becomes comparable with the anisotropy energy KV inducing random fluctuations of the magnetization in these particles resulting in a zero net magnetization when averaged over a typical time scale τ of these fluctuations. This phenomenon is called super-paramagnetism.
The relaxation time describes how fast does it take for a magnetization reversal between two energy minima separated by an anisotropy (shape, magneto−crystalline,..) energy barrier. The relaxation time given by Néel−Brown's model is (Brown [1963]; Néel [1949]):

$$\frac{1}{\tau} = \frac{1}{\tau_0} exp\Big(- \frac{\Delta E}{K_B T}\Big) \tag{2.8}$$

From a mechanical model and considering the elastic properties of ferromagnets, Néel deduced that τ_0 ranges from 10^{-10} to 10^{-12} s for magnetic nanoparticles.

The theory of super-paramagnetism indicates that in the absence of an applied external field, the magnetic moments will be randomly oriented in a way similar to paramagnetic atoms but with a much larger magnetic susceptibility. This implies that for such particles, the field dependence of magnetization is not hysteretic but rather described by a Brillouin function; furthermore, the temperature dependence of the magnetic susceptibility follows a Curie law behavior.

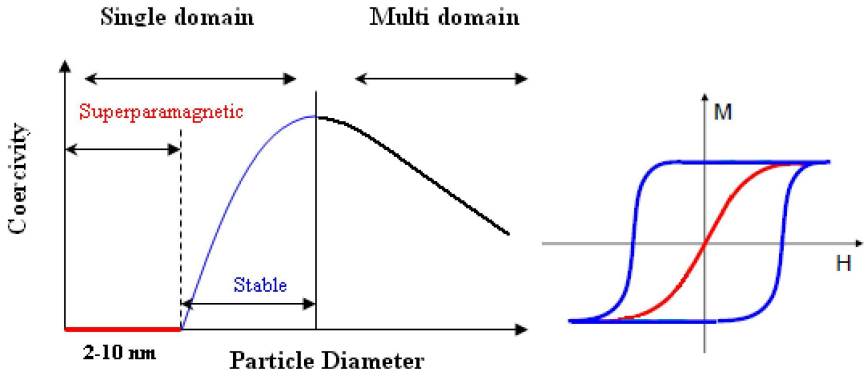

Figure 2.3: The variation of coercivity with the particle's diameter.

In terms of comparison between the anisotropy energy **KV** and the thermal energy $K_B\mathbf{T}$, there are two major types of super-paramagnetism:

- If the thermal energy is large enough i.e. $K_bT \gg \mathbf{KV}$, then the magnetic moments is said to be freely fluctuating. The treatment of the thermal equilibrium magnetization properties of an ensemble of such particles is similar to the Langevin treatment of atomic paramagnetism. Such behavior is called isotropic super-paramagnetism

- If the two energies are comparable i.e $K_b\mathbf{T} \leq \mathbf{KV}$, then the magnetic moment will be blocked up to a given temperature called blocking temperature $\mathbf{T}_b$, above which the direction of magnetization will fluctuate between the two easy directions with a characteristic time τ (equation 2.8). Such behavior is called anisotropic or blocked super−paramagnetism.

2.3.1 Blocking temperature

Introduced by Néel in 1949, the blocking temperature is a characteristic temperature of super−paramagnetic particles which serves as a threshold temperature above which the paramagnetic behavior appears. Below $\mathbf{T}_b$ hysteretic response of the moments is observed for the reason that the thermal activation is not

sufficient to allow the immediate alignment of these moments with the external applied field. In other words, below $\mathbf{T}_b$, due to the anisotropy the magnetic moments are blocked from responding freely to the external applied field.
It should be noted that for a specific sample, $\mathbf{T}_b$ is not uniquely defined and it depends on the size and the shape of the particles, the substrate as well as on the time scale of observation.

2.4 Dynamical equations

In fine ferromagnetic nanoparticles, the magnetization dynamics could be addressed either by solving the stochastic langevin equation, which is the Landau-lifshitz-Gilbert equation, or by solving the equivalent Fokker Planck equation derived by Brown.

2.4.1 Landau-Lifshitz-Gilbert equation

From quantum mechanics, we know that an ensemble of magnetic moments will undergo a precessional motion if placed in a magnetic field. Applying the theorem of angular momentum, we calculate the equation of motion of these moments :

$$\frac{d\overrightarrow{L}}{dt} = \frac{d\overrightarrow{m}}{dt} = -\gamma \overrightarrow{m} \wedge \overrightarrow{H} \tag{2.9}$$

with $\overrightarrow{L}$ being the angular momentum of the total magnetic moment $\overrightarrow{m}$ ($m = \sum_i m_i$). Provided that, the magnetization $\overrightarrow{M}$=$\overrightarrow{m}$/V, where V is the volume of the ensemble, we write down the equation of motion of the magnetization vector of this ensemble :

$$\frac{d\overrightarrow{M}}{dt} = -\gamma \overrightarrow{M} \wedge \overrightarrow{H} \tag{2.10}$$

where $\gamma = g\frac{|e|}{2m_e}$ is the gyromagnetic coefficient.
In magnetic materials, the evolution of the magnetization vector in time and space is well described by the phenomenological equation of Landau-Lifshitz (Landau and Lifshitz [1935]) or Landau-Lifshitz-Gilbert (Gilbert [1955]).
The model is based on the above derived dynamical equation (2.10), but with

a driving field $\overrightarrow{H}_{eff}$ that takes into account the external applied field and the quantum mechanical effects (exchange), and the anisotropy (magneto−crystalline and shape) :

$$\overrightarrow{H}_{eff} = \overrightarrow{H}_{ex} + \overrightarrow{H}_{an} + \overrightarrow{H}_{0}$$

However, the magnetization dynamics in real systems is often damped. The damping could result from the complex interactions of the electron's magnetic moment with: the crystal lattice (impurities, defects ,...), other electrons, phonon, etc...(Aharoni [1996]).
To account for this damping, Landau−Lifshitz introduced a phenomenological term to the equation 2.10 of the form :

$$-\frac{\alpha\gamma'\mu_0}{M_s}\overrightarrow{M} \wedge \left(\overrightarrow{M} \wedge \overrightarrow{H}_{eff}\right)$$

where $\gamma' = \gamma/(1+\alpha^2)$ and α: damping constant.
Then, the Landau−Lifshitz dynamical equation of magnetization vector reads :

$$\frac{\partial\overrightarrow{M}}{\partial t} = -\gamma'\mu_0\left(\overrightarrow{M} \wedge \overrightarrow{H}_{eff}\right) - \frac{\lambda\gamma'\mu_0}{M_s}\left(\overrightarrow{M} \wedge \left[\overrightarrow{M} \wedge \overrightarrow{H}_{eff}\right]\right) \tag{2.11}$$

Later on, Gilbert introduced a damping term that acts not only on the reorientation of magnetization towards the effective field but on the precessional motion itself :

$$-\frac{\alpha}{M_s}\overrightarrow{M} \wedge \frac{\partial\overrightarrow{M}}{\partial t}$$

The Gilbert equation of motion reads :

$$\frac{\partial\overrightarrow{M}}{\partial t} = -\gamma\mu_0\left(\overrightarrow{M} \wedge \overrightarrow{H}_{eff}\right) - \frac{\alpha}{M_s}\left(\overrightarrow{M} \wedge \frac{\partial\overrightarrow{M}}{\partial t}\right) \tag{2.12}$$

The damping constant α is very significant since it parameterizes the relaxation of the magnetization vector towards the equilibrium direction. In other words, it corresponds to the energy dissipation per precession period. For α=0 (no damping), the magnetization will infinitely precess around the effective field. It is of the order $10^{-4} - 10^{-2}$ in garnets and 10^{-2} in cobalt or permalloy (Mayergoyz et al. [2009]; Respaud et al. [1999]). Therefore, the Landau-Lifshitz-Gilbert equation is

:

$$\frac{\partial \overrightarrow{M}}{\partial t} = -\frac{\gamma\mu_0}{(1+\alpha^2)M_s}\left(\overrightarrow{M} \wedge \overrightarrow{H}_{eff}\right) - \frac{\gamma\alpha\mu_0}{(1+\alpha^2)M_s}\left(\overrightarrow{M} \wedge \left[\overrightarrow{M} \wedge \overrightarrow{H}_{eff}\right]\right) \quad (2.13)$$

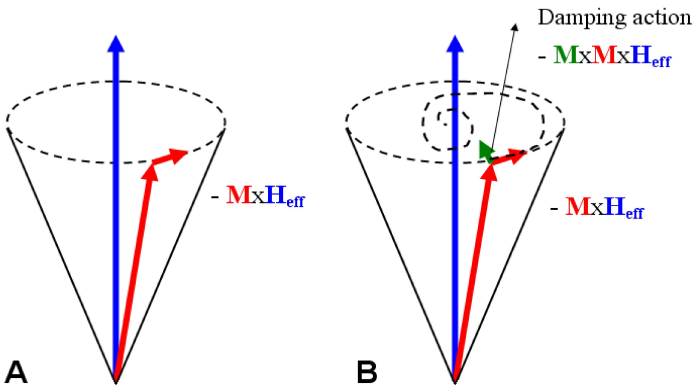

Figure 2.4: The precession of the magnetization vector (red) around the effective field (blue) : A- No damping; B- with damping.

From a physical point of view, the first term of equation 2.13 corresponds to a torque exerted by the effective field $\overrightarrow{H}_{eff}$ on $\overrightarrow{M}$ forcing it to precess (figure 2.4−A) while, the second term represents another torque that pushes $\overrightarrow{M}$ in the direction of $\overrightarrow{H}_{eff}$ (figure 2.4−B).

2.4.2 Fokker Planck equation

In a statistical mechanical formalism, the time evolution of the probability distribution **P** of the magnetization orientation is given by the following Fokker Planck equation (Garcia-Palacios [2000]):

$$\begin{aligned}\frac{\partial P}{\partial t} &= -\frac{\partial}{\partial \overrightarrow{M}} \cdot \left[\left(-\frac{\gamma\mu_0}{(1+\alpha^2)M_s}\left(\overrightarrow{M} \wedge \overrightarrow{H}_{eff}\right) - \frac{\gamma\alpha\mu_0}{(1+\alpha^2)M_s}\left(\overrightarrow{M} \wedge \left[\overrightarrow{M} \wedge \overrightarrow{H}_{eff}\right]\right)\right.\right. \\ &+ \left.\left.\frac{1}{2\tau_N}\overrightarrow{M} \wedge \left(\overrightarrow{M} \wedge \frac{\partial \overrightarrow{M}}{\partial t}\right)\right)P\right] \quad (2.14)\end{aligned}$$

τ_N is the Néel free diffusion time which is a characteristic time of diffusion in the absence of the energy barrier. Knowing that the boltzmann distribution :

$$P_e(\overrightarrow{M}) \propto exp(-\beta E(\overrightarrow{M})) \tag{2.15}$$

is a stationary solution of the Fokker Planck equation with $E(\overrightarrow{M})$ being the total energy of the system, we find that (Garcia-Palacios [2000]) :

$$\tau_N = 2D\frac{\gamma^2}{1+\alpha^2}$$

The factor D determines the amplitude of the thermal or random field introduced by Brown.

$$D = \frac{\alpha K_B T}{\mu_0 \gamma M_s V} \tag{2.16}$$

2.5 Néel-Brown's Model

Due to the important practical application of monodomains in data storage, the full understanding of magnetization reversal and the knowledge of the corresponding relaxation times are essential.
At low temperatures, the magnetization reversal in isolated monodomain particles takes place either under an external applied field which suppresses the energy barrier, or due to thermal effects which produce statistical fluctuations.
In an external applied field, the magnetization reversal process is well described by Stoner-Wohlfarth model (Stoner and Wohlfarth [1948]). The mains assumptions underlying this model are:

- Macro-spin approximation where the atomic magnetic moments (spins) are treated as a giant magnetic moment (giant spin).
- Coherent rotation of magnetization in each particle where the atomic spins remain parallel as they rotate to new magnetic moment orientation.

The magnetization reversal by thermal activation was first proposed by Néel in 1949 (Néel [1949]) and further developed by Brown (Brown [1963]). The Néel−Brown model states that at any finite temperature T, thermal fluctuations

cause the spins to undergo a Brownian-like motion about the easy axis, with a finite probability that the moment will flip from one easy direction to another.

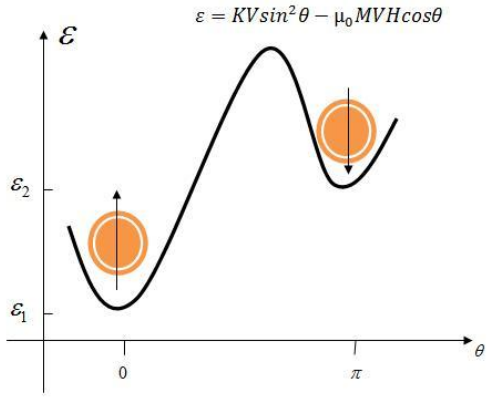

Figure 2.5: Dependence of energy of uniaxial anisotropic particles.

2.5.1 Néel Model

In a semi−classical model, Néel introduced the first calculations of the relaxation time in monodomains with uniaxial anisotropy. The model is based on the approximations of coherent rotation, macrospins and discrete orientation model.

- **Macrospin approximation**: in a monodomain nanoparticle, all the magnetic moments (spins) are rigidly coupled so that they form a giant moment. The resulting total magnetic moment is given by $m = VM_s$.

- **Discrete orientation model**:
  In the discrete orientation model, a monodomain nanoparticle at a given energy minimum (see figure 2.5), would be magnetized along a given axis as long as the energy barrier separating any two minima is large compared to the thermal energy i.e $(E_{max} - E_{min}) >> K_BT$.
  Consider an ensemble of n particles distributed, according to their directions up or down, on two semi-spheres separated by an equatorial plane where the +x-axis and the −x-axis form the easy axes of magnetization.
  This is equivalent to the case where the particles are distributed at two

energy minima separated with an anisotropy energy barrier as in figure 2.5. For a particle with orientation 1 along +x, there is a probability ν_{12}dt to jump to orientation 2 along −x in a time interval dt. In the same time interval, there will be a probability ν_{21} for a particle to undergo an inverse transition i.e. from −x direction to +x direction.
Assuming that there exist n_1 particles at the first energy minimum (with direction up) and n_2 particles at the second minimum (with direction down), then the approach to statistical equilibrium is described by the following equation:

$$\dot{n}_1 = -\dot{n}_2 = n_2\nu_{21} - n_1\nu_{12}. \tag{2.17}$$

The transition or jump probability is given by Boltzmann statistics :

$$\nu_{ij} = c_{ij}exp\Big(- (E_m - E_i)/K_BT\Big) \tag{2.18}$$

It is worth to mention that this simple model will break down eventually as V/T tends to 0, because the distribution will no longer be sufficiently concentrated near 0 and π.

2.5.1.1 Calulation of the relaxation time τ

The relaxation time is the inverse of the probability per unit time for a spin to flip its direction and depends on the number of particles which traverse the equatorial plane in the two directions.

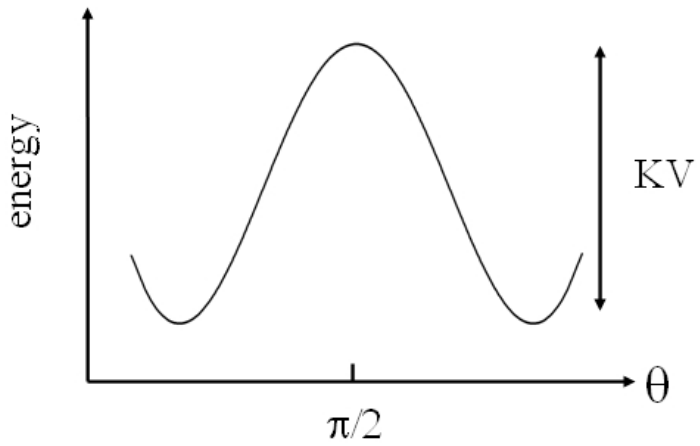

Figure 2.6: Dependence of energy of uniaxial anisotropic particles in absence of external field.

In the absence of an external magnetic field, the transition probability $\nu_{12} = \nu_{21} = \nu$:

$$\nu = \frac{KV}{K_B T} exp\Big(- \frac{KV}{K_B T}\Big)$$

Consequently, equation 2.17 could be re-written as follows :

$$\dot{n}_1 = -\dot{n}_2 = \frac{n_2}{2\tau} - \frac{n_1}{2\tau}$$

In a further approximation, Néel assumed that $\dot{n}_1$ particles cross the barrier in one direction only:

$$\dot{n}_1 = \frac{n_1}{2\tau} \tag{2.19}$$

The validity of this one-direction crossover of the barrier will be discussed in section 2.5.2.

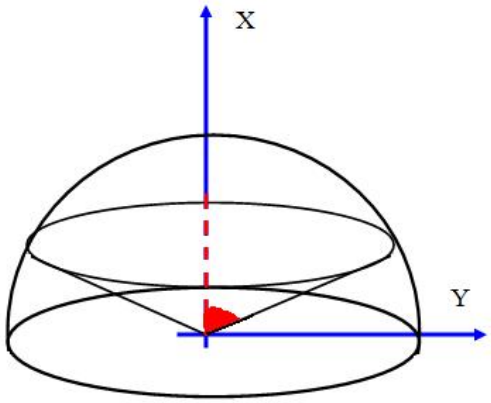

Figure 2.7: Spins in a cone at the equatorial plane.

In the equatorial plane, $\dot{n}_1$ is by definition equivalent to the number of particles contained in the cone of angle $\frac{\pi}{2} - \mid \frac{\overline{d\theta}}{dt} \mid dt$ with $\mid \frac{\overline{d\theta}}{dt} \mid > 0$ (see figure 2.7). Thus, $\dot{n}_1 = n_1 \nu \mid \frac{\overline{d\theta}}{dt} \mid$, then using equation 2.19 the relaxation time is given by :

$$\frac{1}{\tau} = \frac{2KV}{K_B T} \mid \frac{\overline{d\theta}}{dt} \mid exp\Big(- \frac{KV}{K_B T}\Big) \tag{2.20}$$

Calculation of $\mid \frac{\overline{d\theta}}{dt} \mid$:

The macro−spin can be approximated as a gyroscope with angular moment per unit volume :

$$\overrightarrow{m} = \overrightarrow{M} = \frac{g\mu_B}{\hbar}\overrightarrow{\sigma} \quad then \quad \overrightarrow{\sigma} = \frac{2m}{eg}\overrightarrow{M} \tag{2.21}$$

where e and m are the charge and the mass of an electron respectively, g is Landé factor and M is the spontaneous magnetization.
The passage across the barrier is animated by the perturbing forces which are capable to transfer the thermal agitation energy of the lattice to the macro-spins. The perturbing forces or the coupling forces with the lattice are equivalent to a torque $\overrightarrow{\Gamma}$ situated in the equatorial plan and perpendicular to $\overrightarrow{M}$. The magnitude of $\overrightarrow{\Gamma}$ is :

$$\Gamma \;=\; -\frac{\partial E_a}{\partial \theta}$$

$$= -\Big(\frac{\partial}{\partial\theta}KV\sin^2\theta\Big)$$
$$= -2K\sin\theta\cos\theta$$

To calculate $|\,\frac{\overline{d\theta}}{dt}\,|$, Néel solved the equation of motion of the gyroscope given by the general theorem of angular momentum :

$$\overrightarrow{\Gamma} = \frac{d\overrightarrow{\sigma}}{dt} = \frac{2m}{eg}\frac{d\overrightarrow{M}}{dt}$$
$$= \frac{2m}{eg}\,|\,\frac{\overline{d\theta}}{dt}\,|\wedge\overrightarrow{M}$$

It follows that

$$|\,\frac{\overline{d\theta}}{dt}\,| = \frac{2eK}{mM_s}\cos\theta$$
$$= \frac{e}{mM_s\sin\theta}\,|\,\overline{\Gamma}\,|$$

But in the equatorial plane, $\theta = \pi/2$, thus

$$|\,\frac{\overline{d\theta}}{dt}\,| = \frac{e}{mM_s}\,|\,\overline{\Gamma}\,| \tag{2.22}$$

Therefore, the first expression of the relaxation time is:

$$\frac{1}{\tau} = \frac{2KV}{K_BT}\frac{e}{mM_s}\,|\,\overline{\Gamma}\,|\,exp\Big(-\frac{KV}{K_BT}\Big) \tag{2.23}$$

Now, the problem reduces to the determination of the average $|\,\overline{\Gamma}\,|$ of the perturbing forces.

What is the origin of the perturbing forces ?

Due to the rotational invariance of the spin ensemble, Heisenberg exchange interactions could be excluded.
Actually, thermal agitations cause deformations in the crystalline lattice. Consequently, these deformations induce magneto-crystalline anisotropy , magneto−elastic

coupling forces with crystalline lattice, and lead to variations of the shape demagnetizing field. All these three effects could be the possible origin of the perturbing forces. However, the analytical calculation of the average $\mid \overline{\Gamma} \mid$ for all types of deformations is not possible. For simplicity, the deformations are assumed to be uniform.
The average torque $\mid \overline{\Gamma_e} \mid$ due to the magneto−elastic forces is:

$$\mid \overline{\Gamma_e} \mid = 3G\lambda\sqrt{\frac{2GK_BT}{\pi V}} \tag{2.24}$$

where G is the drift coefficient and λ is longitudinal magnetostriction at saturation.
The average torque $\mid \overline{\Gamma_d} \mid$ due to the demagnetizing forces is:

$$\mid \overline{\Gamma_d} \mid = FM_s^2\sqrt{\frac{2GK_BT}{\pi V}} \tag{2.25}$$

where F is a constant.
The total average $\mid \overline{\Gamma} \mid$ of the perturbing forces is thus:

$$\mid \overline{\Gamma} \mid = \mid FM_s^2 + 3G\lambda \mid \sqrt{\frac{2GK_BT}{\pi V}} \tag{2.26}$$

Therefore, in the absence of any external magnetic field, the relaxation time in isolated monodomain ferromagnetic nanoparticle is:

$$\frac{1}{\tau} = \frac{2Ke}{mM_s} \mid FM_s^2 + 3G\lambda \mid \sqrt{\frac{2V}{\pi GK_BT}} exp\Big(-\frac{KV}{K_BT}\Big) \tag{2.27}$$

This is the expression obtained by Néel in his fundamental work of 1949 (Néel [1949]).

2.5.2 Brown Model

In gyromagnetic system, the only effect of the large torque is to produce a precession about the polar axis so that a representative point moves along a parallel of latitude and it is not obvious that a passage to the new pole is more probable

than a return to the old one (Brown [1959]).
To avoid this dilemma Brown approached the problem in a more general way based on the theory of stochastic processes and Brownian motion. Each particle or macro−spin has a uniform magnetization vector $\overrightarrow{M}$ of constant magnitude but variable orientation. It is only the direction of $\overrightarrow{M}$ that is influenced by the thermal fluctuations while the magnitude is conserved. The changes in the direction obey a LLG equation:

$$\frac{\partial \overrightarrow{M}}{\partial t} = -\frac{\mu_0 \gamma_0}{M_s(1+\alpha^2)} \overrightarrow{M} \times [\overrightarrow{H} + \alpha \overrightarrow{M} \times \overrightarrow{H}]. \tag{2.28}$$

To account for the thermal agitation or fluctuation Brown introduced a random field to the LLG equation, so that the equation describing the dynamics of the moments is:

$$\frac{\partial \overrightarrow{M}}{\partial t} = -\frac{\mu_0 \gamma_0}{M_s(1+\alpha^2)} \overrightarrow{M} \times [(\overrightarrow{H} + \overrightarrow{h(t)}) + \alpha \overrightarrow{M} \times (\overrightarrow{H} + \overrightarrow{h(t)})] \tag{2.29}$$

where the field is given by $\overrightarrow{H} = \frac{\partial E}{\partial \overrightarrow{M}}$ and E is the total energy. Despite that Brown had not discussed the origin of the random field, however he introduced a detailed study of its statistical properties. The concept of the random field will be discussed in the following paragraph.

2.5.2.1 The random field

The random or thermal field is a gaussian stationary stochastic process that stands for the effects of interactions of the magnetic moment with the microscopic degrees of freedom (phonons, conducting electrons, nuclear spins...) which cause the fluctuations in orientation of the moments (Garcia-Palacios [2000]).

$$< \overrightarrow{h}(t) >= 0 \quad and \quad < \overrightarrow{h}_i(t) \overrightarrow{h}_j(t') >= 2D\delta_{ij}\delta(t-t'). \tag{2.30}$$

The constant D given by equation 2.16, measures the strength of the thermal fluctuations and (i=1,2,3) are the components of the field.
The Gaussian property of the fluctuations arises from the interaction of the moment with a large number of microscopic degrees of freedom with equivalent

statistical properties. Besides, the thermal field is assumed to be a $'white'$ noise meaning that it is not correlated to its values at earlier or later times so that, its autocorrelation function is a delta Dirac function (Garcia-Palacios [2000]). The autocorrelation function has two possible interpretations: a mathematical one given by Itô and a physical one given by Stratonovich.

- **Itô interpretation**: the noise is instantaneous and it is a delta dirac function and thus it has no physical realization.
- **Stratonovich interpretation**: there exist an interval of time much shorter than the response time of the system over which the noise is not instantaneous.

Brown adopted the physical interpretation proposed by Stratonovich.

2.5.2.2 Derivation of the Fokker Planck equation

A particle with instantaneous moment orientation (θ, ϕ) can be represented by a point over a unit sphere and a statistical ensemble of such particles can be represented by a distribution of points over a unit sphere with surface density $W(\theta, \phi, t)$.
The movement of the representative points on the surface of the sphere due to the changes in the direction of the moments, induces a net surface current density $J(\theta, \phi)$:

$$\overrightarrow{J} = W\overrightarrow{v} - k'\overrightarrow{\nabla}W. \tag{2.31}$$

Given that $\acute{k}$ is a positive constant.
The first term accounts for the motion of the representative points with velocity $\overrightarrow{v}$ while the second term accounts for the thermal agitation. Writing continuity equation 2.14 in spherical coordinates and setting $P = W\sin\theta$, we get the current density components :

$$\begin{aligned} J_\theta &= -\Big(h'\frac{\partial E}{\partial \theta} - g'\frac{1}{\sin\theta}\frac{\partial E}{\partial \phi}\Big)W + k'\frac{\partial W}{\partial \theta} \\ J_\phi &= -\Big(g'\frac{\partial E}{\partial \theta} + h'\frac{1}{\sin\theta}\frac{\partial E}{\partial \phi}\Big)W + k'\frac{1}{\sin\theta}\frac{\partial W}{\partial \phi} \end{aligned}$$

where

$$h' = \frac{\alpha\gamma_0}{(1+\alpha^2)\mu_0 V M_s}; \quad g' = h'/\alpha; \quad k' = h'/\beta$$

Then the general FP equation for a monodomain magnetic nanoparticle is given by:

$$\begin{aligned} \frac{\partial W}{\partial t} &= \frac{1}{\sin\theta}\frac{\partial}{\partial\theta}\Big(\sin\theta\Big[\Big(h'\frac{\partial E}{\partial\theta} - g'\frac{1}{\sin\theta}\frac{\partial E}{\partial\phi}\Big)W + k'\frac{\partial W}{\partial\theta}\Big]\Big) \\ &+ \frac{1}{\sin\theta}\frac{\partial}{\partial\phi}\Big[\Big(g'\frac{\partial E}{\partial\theta} + h'\frac{1}{\sin\theta}\frac{\partial E}{\partial\phi}\Big)W + k'\frac{1}{\sin\theta}\frac{\partial W}{\partial\phi}\Big]. \end{aligned} \tag{2.32}$$

The general solution of the FP equation is of the form:

$$W = W_0 + \sum_{n=1}^{\infty} A_n F_n(\theta,\phi) exp(-p_n t) \tag{2.33}$$

with $W_0 = Aexp(-\beta E)$ being the equilibrium solution and $\beta = (K_B T)^{-1}$.

2.5.2.3 Kramer's Method and High Energy Barrier

The analytical solution of the general FP equation is only possible for nanoparticles with uniaxial anisotropy i.e. when ϕ is constant.
The general FP equation reduces to :

$$\frac{\partial W}{\partial t} = \frac{1}{\sin\theta}\frac{\partial}{\partial\theta}\Big(\sin\theta\Big[h'\frac{\partial E}{\partial\theta}W + k'\frac{\partial W}{\partial\theta}\Big]\Big) \tag{2.34}$$

And the total energy:

$$E = E(\theta) = KV\sin^2\theta - \mu_0 V M_s H\cos\theta$$

where the external field is applied parallel or anti−parallel to the easy axis.

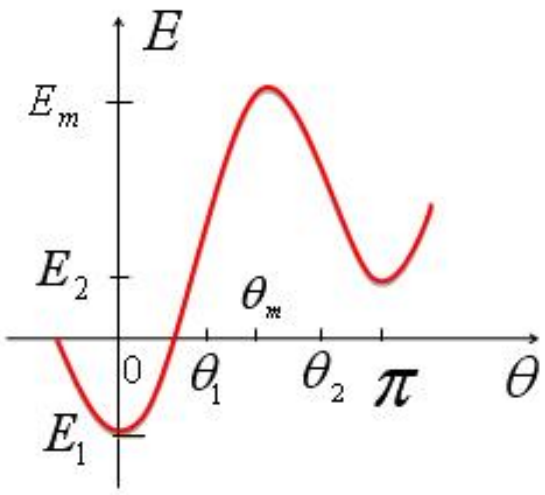

Figure 2.8: Energy Distribution.

Between the two energy minima 0 and π, choose two regions $0 \leq \theta \leq \theta_1$ and $\theta_2 \leq \theta \leq \pi$ under the following two conditions:

- From the outset, the equilibrium is being achieved in these regions.
- $e^{-\beta E_m} \ll e^{-\beta E(\theta_i)} \ll e^{-\beta E_i}$ this condition is satisfied by the high energy barrier approximation where $\beta(E_m - E_i) \gg 1$.

Knowing that the total number of particles is given by $n = \int W d\Omega$, then:

- in the region $(0, \theta_1)$ the number of particles n_1 is:

$$n_1 = 2\pi W_1 e^{\beta E_1} I_1 \quad with \quad I_1 = \int_0^{\theta_1} e^{-\beta E(\theta)} \sin\theta d\theta \quad and \quad W_1 = W(0) \quad (2.35)$$

- in the region $(0, \theta_2)$ the number of particles n_2 is:

$$n_2 = 2\pi W_2 e^{\beta E_2} I_2 \quad with \quad I_2 = \int_{\theta_2}^{\pi} e^{-\beta E(\theta)} \sin\theta d\theta \quad and \quad W_2 = W(\pi) \quad (2.36)$$

To proceed, we may replace $E(\theta)$ by its Taylor's series about 0 truncated at the second order. This is justified by the second condition which indicates that there

exists a rapid decrease of the exponential factor with distance from the minimum of energy. Also, because θ is small we may replace $\sin\theta$ by θ, then:

$$I_i = e^{-\beta E_i}/\beta k_i \quad with \quad k_1 \equiv E^{''}(0) \quad and \quad k_2 \equiv E^{''}(\pi) \tag{2.37}$$

Despite the fact that W is very small between (θ_1, θ_2), it is sufficient to maintain a small net flow of points from the overpopulated to the under-populated region. This flow can be approximated by a steady divergenceless current:

$$I = 2\pi sin\theta J_\theta \tag{2.38}$$

But

$$J_\theta = -\Big(h'\frac{\partial E}{\partial \theta}W + k'\frac{\partial W}{\partial \theta}\Big)$$

and $k' = h'/\beta$, then:

$$\frac{\partial W}{\partial \theta} + \beta\frac{\partial E}{\partial \theta}W = -\frac{\beta I}{2\pi h' \sin\theta} \tag{2.39}$$

By multiplying equation 2.39 by $e^{-\beta E}$ and integrating between θ_1 and θ_2, we get:

$$W_2 e^{-\beta E_2} - W_1 e^{-\beta E_1} = -\frac{\beta I}{2\pi h'} I_m \quad where \quad I_m = \int_{\theta_1}^{\theta_2} e^{\beta E}\frac{d\theta}{\sin\theta} \tag{2.40}$$

As for I_i, we expand $E(\theta)$ around θ_m and then replace $\sin\theta$ by $\sin\theta_m$, we get:

$$I_m = \frac{e^{\beta E_m}}{\sin\theta_m}\sqrt{\frac{2\pi}{\beta k_m}} \quad where \quad k_m \equiv -E''(\theta_m) \tag{2.41}$$

From equations 2.35, 2.36, 2.39 and 2.40 and knowing that $I = \dot{n}_1 = -\dot{n}_2$,we get:

$$\dot{n}_1 = -\dot{n}_2 = \frac{h'}{\beta I_m}\Big(\frac{n_2}{I_2} - \frac{n_1}{I_1}\Big) \tag{2.42}$$

The high energy barrier approximation validates the discrete orientation model 2.17, then:

$$\nu_{ij} = \frac{h'}{\beta I_m I_i} \quad where \quad (i = 1, j = 2 \; or \; i = 2, j = 1) \tag{2.43}$$

From equations 2.37 and 2.43, we can write down the final expression of the

transition probability:

$$\nu_{ij} = c_{ij} e^{-\beta(E_m - E_i)} \quad with \quad c_{ij} = h' k_i \sin\theta_m \sqrt{\frac{\beta k_m}{2\pi}} \tag{2.44}$$

In the very early stages of an approach to equilibrium, the inverse of the longest finite time constant is determined by the smallest non-vanishing eigenvalue of the FP equation corresponding to n=1 in equation 2.33.

$$\frac{1}{\tau} = \nu_{12} + \nu_{21} \quad with \quad \nu_{12} = c_{12} e^{-\beta(E_m - E_1)} \quad and \quad \nu_{21} = c_{21} e^{-\beta(E_m - E_2)} \tag{2.45}$$

Provided that $\cos\theta_m = \varepsilon = \frac{H}{H_c}$ where $H_c = \frac{2K}{\mu_0 M_s}$ is the coercive field, then the energy at the maximum of the barrier (figure 2.8) $E_m = KV(1-\varepsilon^2)$, and the energies at the two minima are $E_{\frac{1}{2}} = \pm\mu_0 HMV$.
The constants $K_m = 2KV(1-\varepsilon^2)$ and $K_{\frac{1}{2}} = 2KV(1\pm\varepsilon)$.
The height of the energy barrier can be calculated as follows:

$$\Delta E = KV(1 - \frac{H_0}{H_c})^2 \tag{2.46}$$

where H_0 is the external applied field and $H_c = \frac{2K}{\mu_0 M_s}$ is the coercive field.
Finally, the relaxation time in isolated monodomain ferromagnetic nanoparticle is:

$$\frac{1}{\tau} = \frac{\alpha}{1+\alpha^2} \frac{\gamma_0}{M_s V} \frac{(2KV)^{3/2}}{(2\pi K_B T)^{1/2}} (1-\varepsilon^2) \Big[(1+\varepsilon) e^{-\frac{KV}{K_B T}(1+\varepsilon)^2} + (1-\varepsilon) e^{-\frac{KV}{K_B T}(1-\varepsilon)^2} \Big] \tag{2.47}$$

- K= anisotropy constant; V= Volume of the particle;
- M_s= saturation magnetization; α= damping constant

The formula derived by brown calculations is similar to Néel and the difference between the two approaches is restricted in the pre−factor.

2.5.2.4 Non-axially symmetric particles

When an external magnetic field is applied with a given angle ψ to the easy axis then the total energy of the particle is modified (Stoner and Wohlfarth [1948]):

$$E = E(\theta) = KV \sin^2\theta - \mu_0 V M_s H \cos(\theta - \psi)$$

The relaxation times in monodomain nanoparticles with an oblique external field, can be calculated in the same way as for the axially symmetric case provided that the minima of energy corresponds to $0 < \theta_A$ and $\theta_B = \pi\text{-}\theta_A < \pi$. The height of the energy barrier can be approximated as follows (Coffey et al. [1995]):

$$\Delta E = KV(1 - \frac{H_0}{H_c})^{0.86+1.14h_c(\psi)} \tag{2.48}$$

where

- $$h_c(\psi) = \frac{1}{(\cos(\psi)^{2/3} + \sin(\psi)^{2/3})^{3/2}}$$
- $$H_c = \frac{2K}{\mu_0 M_s} \cdot h_c\psi$$

$$\begin{aligned} \frac{1}{\tau} &= \frac{h'}{2\pi}\sin(\theta_m)\sqrt{-E''(\sin(\theta_m))}\Big[\frac{\sqrt{E''(\sin(\theta_A))}}{\sin(\theta_A)}e^{-\beta(E(\theta_m)-E(\theta_A))} \\ &- \frac{\sqrt{E''(\sin(\theta_B))}}{\sin(\theta_B)}e^{-\beta(E(\theta_m)-E(\theta_B))}\Big] \end{aligned} \tag{2.49}$$

2.5.2.5 Discussion

To this end, we have presented the approaches of Néel and Brown used to derive analytically the relaxation time of magnetization reversal processes in magnetic nanoparticles. The Néel−Brown's model is restricted to the uniaxial particles with an external field applied along the anisotropy axis. However, other theoretical works using numerical simulations succeeded to calculate the relaxation times for any arbitrary angle of the external applied magnetic field (Coffey et al.

[1995]), as it was discussed in the previous paragraph. Moreover, (Aharoni [1973]) calculated the relaxation times in particles with cubic anisotropy.
Regarding the Néel's calculations, one may remark that it is not clear why the magnetic moments cross the barrier in one direction only and consequently change their orientation knowing that there is no reason for these particles to reoriented toward their initial position.
Brown's calculations seem to be more rigorous, however Brown did not precise the origin of the thermal field. In Brown's calculation, the assumption of constant magnitude of magnetization is also questionable.
For both models, it is assumed that the magnetization undergoes a gyroscopic-like motion during its reversal i.e coherent motion during the reversal. Recently, Andrade et al. [2006] have shown that for superparamagnetic nanoparticles with uniaxial anisotropy (diameter$\leq$4 nm), the assumption of complete coherent rotation is not valid.
The Néel−Brown's model ignores the interactions among the nanoparticles such as the magnetic dipole-dipole interaction which are found to have important effects on the dynamics of nanoparticles (Djurberg et al. [1997]; Mamiya et al. [1999]; Mørup et al. [1983]; Rancourt and Daniels [1984]).
The validity of the Néel−Brown's model to describe the magnetization dynamics in isolated magnetic nanoparticles will be discussed in details in Chapter 6, in addition, we investigate the effects of the dipolar interaction on the reversal dynamics.

Chapter 3

Ultrafast Magnetization Dynamics

So many are the reasons that makes the magnetization dynamics an exciting topic and give it a relevant importance for both fundamental studies and technological applications especially with the increasing demands on high speed magnetic memories with high storage density.
A dynamical response in ferromagnetic materials may be induced either by the application of an external magnetic field or thermally by optical excitations with laser pulses. For the first case, it is obvious that a strong magnetic field will align the magnetic moments parallel to each others along its direction. This stable state will break down as soon as the direction of the field is changed. This perturbation forces the magnetic moments to realign themselves along the new direction of the field via a coherent damped precession around the external field with a GHz frequency. This process may take several picoseconds (ps) to nanoseconds (ns).
Secondly, shining a ferromagnetic material with intense laser pulses will thermally perturb both the charge and the spin populations inducing ultrafast dynamical responses happening on time scales that range from few hundreds of femtosecond (fs) to $\sim$ 1 nanosecond (ns).

3.1 Historical Review

Back to 1984, when the first laser induced magnetization dynamics was done on thin Ni films (50−100 nm) (Agranat et al. [1984]). It was predicted that the spin−lattice relaxation time lies between 1 and 40 ns. Later on,Vaterlaus et al. [1992] estimated a 100 ± 80 ps relaxation time in films of gadolinium. This relaxation time was confirmed by the theoretical predictions of Hübner (Hübner and Bennemann [1996]).

However, the cornerstone experimental observation which triggered out the domain of optical manipulation of magnetization with femtosecond laser pulses was that done in strasbourg in 1996 (Beaurepaire et al. [1996]). The authors performed Kerr Magneto-optical measurements in pump(400 nm)−probe(800 nm) configuration on a 20 nm Ni film, and they reported an ultrafast demagnetization within $\sim$ 2 ps.

This unprecedented result plotted on figure 3.1, was confirmed by the different subsequent experimental works (Bigot [2001]; Bigot et al. [2004]; Güdde et al. [1999]; Hohlfeld et al. [1997]; Ogasawara et al. [2005]; Scholl et al. [1997]). Moreover and on larger time scales, other works showed that it is possible to induce precession of the magnetization vector (Bigot et al. [2005]; Ju et al. [1998]).

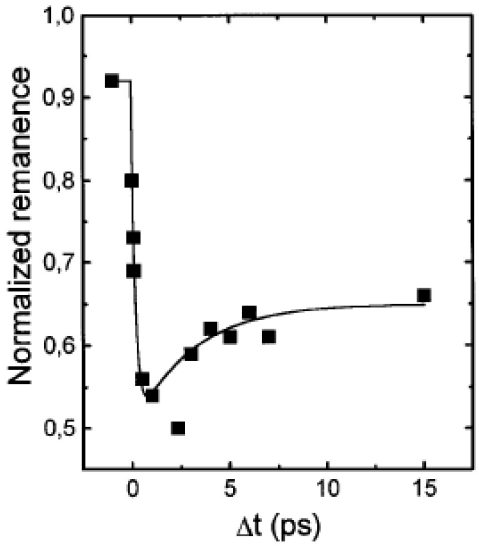

Figure 3.1: The result taken from Ref Beaurepaire et al. [1996] showing a demagnetization in 2 ps.

However in an experiment performed by Koopmans, it is shown that when the electrons are out of equilibrium, the MO signals (ellipticity and rotation) do not follow the same dynamics and therefore, breaking down the proportionality between the magnetization and the voigt vector (Koopmans et al. [2000]). Such conclusions raised questions on the reliability of the interpretation of the experimental result obtained by Beaurepaire et al..The results are reproduced on figure 3.2.

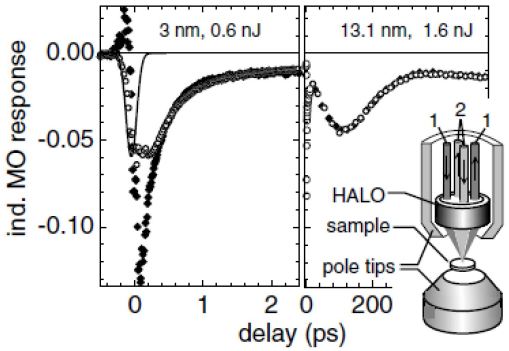

Figure 3.2: Comparison between the induced ellipticity (open circles) and rotation (filled diamonds).Ref (Koopmans et al. [2000])

Two years later, the group of Bigot replied on the criticism. The authors proposed that one should analyze the real and the imaginary parts of the voigt vector ($\mathbf{Q} = q' + iq''$) rather than the Faradays' ellipticity and rotation as Koopmans et al. did. In their work, the authors studied films of $CoPt_3$ using much shorter pulses with 20 fs duration. They showed that after the thermalization of electrons q' and q'' have the same dynamics. However, during the thermalization, the two components follow the different dynamics. The film lost its magnetization on a sub−100 femtosecond time scale where the electrons are not yet thermalized (Guidoni et al. [2002]). Therefore, the raised problem is referred to the used formalism to describe the non−thermalized spin dynamics and this implies new formalisms for the laser induced de−magnetization. For example Boeglin et al. [2010] have shown that during the thermalization of electrons in CoPd samples, an ultrafast change in the spin−orbit coupling leads the quenching of the perpendicular magnetic anisotropy of the samples, thus resulting in a demagnetization of the samples.

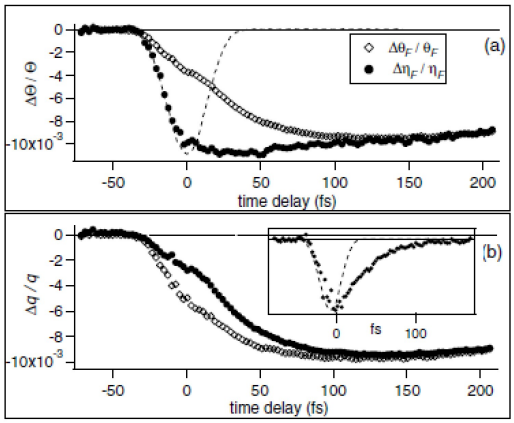

Figure 3.3: (a) Time−resolved Faraday MO signals (ellipticity and rotation). (b) Short−delay relative variations of the voigt vector components.(Guidoni et al. [2002])

3.2 Ultrafast Dynamics

The **T**ime **R**esolved **M**agneto−**O**ptical **K**err **E**ffect (TR−MOKE) measurements with femtosecond pump and probe pulses, is a very powerful tool to study the ultrafast interaction processes that take place between the spins, the charges and the lattice.

3.2.1 Charge Dynamics

The absorption of an intense laser beam by a metallic film within a skin depth of $\sim$ 20 nm will excite the electron-hole pairs that acquire a large kinetic energy far above the Fermi level leading to a nonthermal electronic distribution (figure 3.4−**A**).

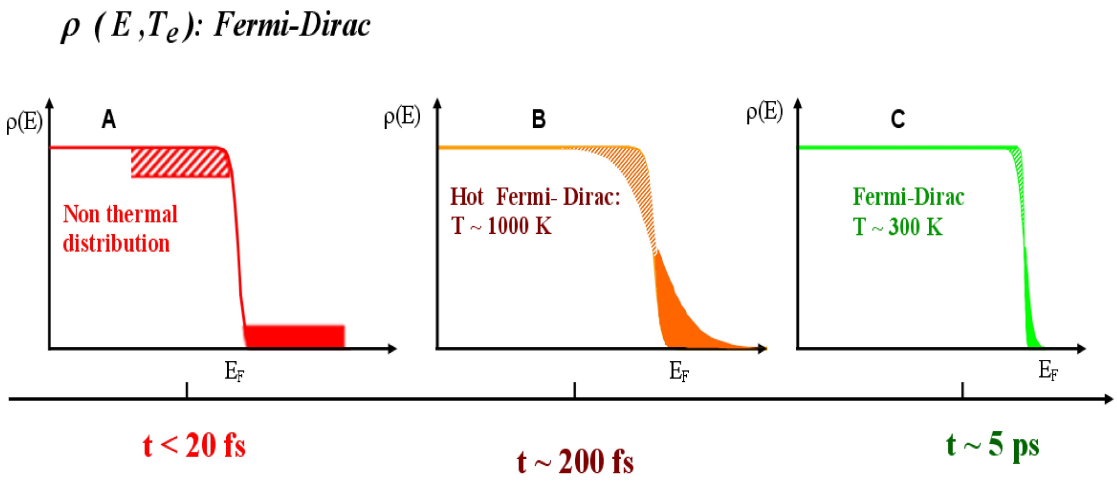

Figure 3.4: Sketch of the electron dynamics in a metal excited with a femtosecond optical pulse.

The quasiparticles then thermalize to a hot Fermi-Dirac distribution (figure 3.4−**B**). This thermalization process is dominated by the scattering between the quasiparticles electron-electron (e-e), hole-hole (h-h) and electron-hole (e-h) and lasts during a few hundreds of femtoseconds. It has been shown that in metals, the electron-phonon scattering also contributes to the electron and hole thermalization (Del Fatti et al. [1998]). The efficient energy transfer between the electrons and the phonons then leads to a cooling of the electronic distribution until an equilibrium between the quasiparticles and lattice temperatures is reached (figure 3.4− **C**). The corresponding timescale depends on the electron-phonon coupling and on the temperature dependent specific heat of the electrons. Typically it occurs within a few picoseconds. The final step is the energy propagation or heat diffusion that depends on the thermal conductivities of the material and surrounding medium with a timescale $\leq$ 1 ns. The relaxation process is well described using the Two−Temperature Model.

3.2.1.1 Two Temperature Model

The two−temperature model (Kaganov et al. [1957]) is widely used to predict the electron and phonon temperature evolution in metals after excitation by ultrashort laser pulses. After the thermalization of the electrons, the metal could be divided into two distinct subsystems, one corresponding to the conduction electrons and one to the lattice phonons.

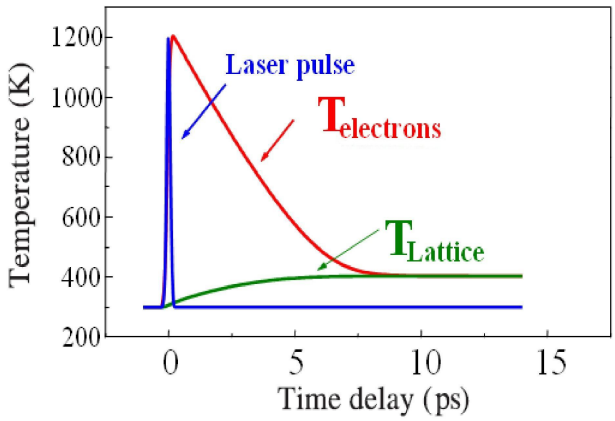

Figure 3.5: The evolution of the electronic and the lattice temperature following a laser excitation.

The dynamics of the electrons and lattice temperatures is given by a set of two coupled differential equations :

$$\begin{aligned} C_e(T_e)\frac{\partial T_e}{\partial t} &= -G_{el}(T_e - T_l) + P(t) - \overrightarrow{\nabla}\kappa_e\overrightarrow{\nabla}T_e(t,\overrightarrow{r}) \\ C_l(T_l)\frac{\partial T_l}{\partial t} &= G_{el}(T_e - T_l) - \overrightarrow{\nabla}\kappa_l\overrightarrow{\nabla}T_l(t,\overrightarrow{r}) \end{aligned} \tag{3.1}$$

where C_e and C_l are respectively the electronic and the lattice specific heats. G_{el} is the coupling constant between the electron and the lattice baths and represents the electron-phonons interactions (Philip [1987]; Suárez et al. [1995]). P(t) is the source term and can be modelled by the envelope of a Gaussian pump pulse with a duration Δt, $P(t) = P_0 exp(-t/\Delta t)$. κ_l and κ_e are the thermal diffusion constants.

For a free electron metal, C_e is a linear function of the temperature and can be written as: $C_e{=}\gamma T_e$, with γ being a constant that depends on the density of electrons and the Fermi temperature (Kittel [1986]).
The Debye Model expresses the lattice specific heat as :

$$C_v = 9NK_B\Big(\frac{T}{\theta_D}\Big)\int_0^{\theta_D/T}\frac{x^4e^x}{(e^x-1)^2}dx \tag{3.2}$$

where $\theta_D = 3NK_B$ is the Debye temperature and K_B is the Boltzmann constant. In the limit $T > \theta_D/3$, the electron phonon relaxation time is (Grimvall [1976]) :

$$\tau_{ep} = 2\pi\lambda\frac{K_BT}{\hbar} \tag{3.3}$$

The constant λ accounts for the mass enhancement due to the electron phonon interactions. Its typical values for metals ranges between 0.1 and 3.
But what about the non thermalized electrons ? how to model the non thermal regime ? and consequently calculate the thermalization time of the electrons ?
In the non−thermalized regime, the electronic distribution is divided into two parts : a thermalized part characterized by its temperature T_e and a non−thermal part characterized by the energy density per volume of the non−thermal electrons. To calculate the thermalization time, we need to solve the following three coupled equations :

$$\begin{aligned}\frac{dN}{dt} &= -\alpha N - \beta N \\ C_e(T_e)\frac{dT_e}{dt} &= -G_{el}(T_e - T_l) + \alpha N \\ C_l(T_l)\frac{dT_l}{dt} &= G_{el}(T_e - T_l) + \beta N\end{aligned} \tag{3.4}$$

where N is the number of excited particles, α and β parameterizes the heat rates of the thermalized electrons and phonons respectively. therefore $\tau_{ther}{=}1/\alpha$.

3.3 Magnetization Dynamics

Soon after the excitation with the intense laser pulse, the magnetic material will loose partially or completely its magnetization. An effect known as ultrafast demagnetization.

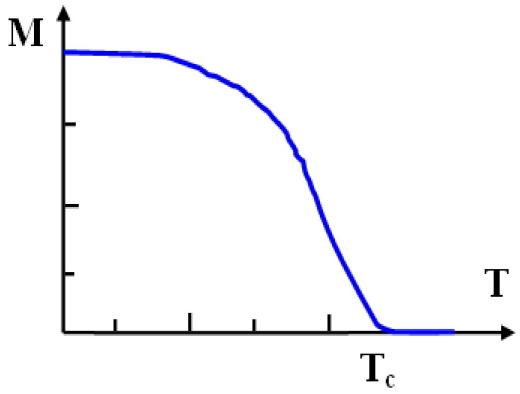

Figure 3.6: variation of the magnetization of a ferromagnet with temperature.

The physical origin of this phenomenon was a debated question for many years. Spin flips induced by the spin orbit coupling could be a possible origin of demagnetization (Bigot [2001]; Zhang et al. [2002]; Zhang and Hübner [2000]). In a recent paper, Bigot et al. showed that it is due to a direct coupling between the light field and the spins populations (Bigot et al. [2009]).
In a second step, the magnetic moments will return to the equilibrium state in a relaxation process known as the re−magnetization process. At high temperatures, the dominant relaxation mechanism of the spins to the lattice is the Raman process sketched on figure 3.7, which can be summarized as follows :

- spin flips.
- absorption of a phonon with frequency ω.
- emission of a phonon with frequency $\omega+\omega_0$.

where ω_0 is the frequency of the direct transition from $\mid b\rangle$ to $\mid a\rangle$.

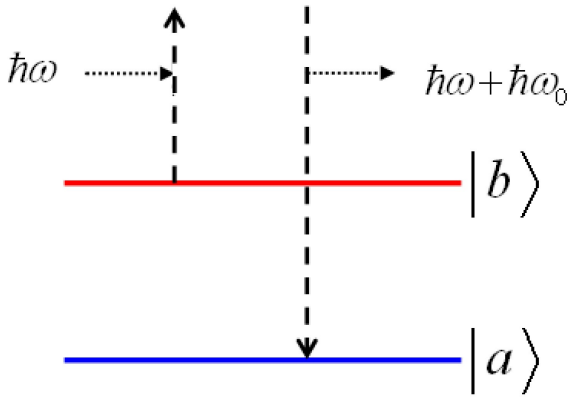

Figure 3.7: Raman Process.

The theoretical modeling of the ultrafast magnetization dynamics is a very complicated problem where the famous models of Heisenberg and Stoner fails to provide sufficient interpretations. However, the first modeling of these ultrafast phenomena was the three temperature model.

3.3.0.2 Three Temperature Model

The three temperature model was introduced in Ref (Beaurepaire et al. [1996]). The basic idea behind this model is to add a third subsystem or reservoir for the spins and consequently a third equation to the system 3.1:

$$\begin{aligned} C_e(T_e)\frac{\partial T_e}{\partial t} &= -G_{el}(T_e - T_l) + P(t) - \overrightarrow{\nabla}\kappa_e\overrightarrow{\nabla}T_e(t,\overrightarrow{r}) \\ C_l(T_l)\frac{\partial T_l}{\partial t} &= G_{el}(T_e - T_l) - \overrightarrow{\nabla}\kappa_l\overrightarrow{\nabla}T_l(t,\overrightarrow{r}) \\ C_s(T_s)\frac{\partial T_s}{\partial t} &= G_{es}(T_e - T_s) - G_{sl}(T_l - T_s) - \overrightarrow{\nabla}\kappa_s\overrightarrow{\nabla}T_s(t,\overrightarrow{r}) \end{aligned} \tag{3.5}$$

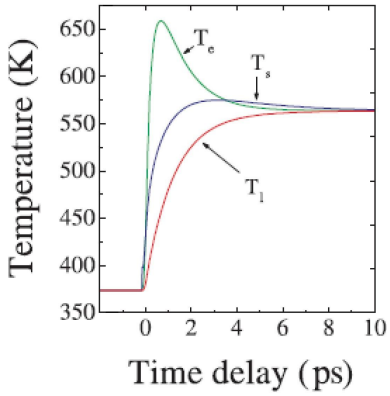

Figure 3.8: Simulated temperature profile for a Ni film excited by an ultrashort laser pulse.

The light is absorbed by the electronic population first, leading to an increase in their temperature (see figure 3.8). Then, the heat will be redistributed among the two other reservoirs. It is also clear that the magnetization will be affected on a time scale where the lattice has not participated in the relaxation yet.

3.3.0.3 Precession of the Magnetization

In addition to the ultrafast demagnetization, the laser excitation may induce a precession of the magnetization vector around an effective field which takes into account the anisotropy and the external fields. In fact, the laser pulse perturbs the direction of the effective field and thus, bringing the magnetic moments out of equilibrium. Their realignment along the new field direction is achieved through a precessional motion.
In general at constant temperature, the precessional motion of the magnetization vector could be modelized using the LLG equation 2.13. But this approach does not hold for a laser induced precession because of the varying temperature. A new approach that takes into account the dynamical change of the modulus of the magnetization vector $\| \vec{M} \|$ is needed. In this essence, Bigot et al. [2005] proposed a phenomenological model of this precession based on the combination of the

Bloch equation (Bloch [1946]) and a term that accounts for the demagnetization.

$$\frac{d\overrightarrow{M}}{dt} = \gamma\Big(\overrightarrow{M} \wedge \overrightarrow{H}_{eff}\Big) - \Big[\frac{d\overrightarrow{M}}{dt}\Big]_{relax} - P(t)\overrightarrow{M}(t) \tag{3.6}$$

where the second term of the right part of equation 3.6 corresponds to the damping. The magnetization modulus dependence on temperature is chosen to be represented by the following equation:

$$\mid \overrightarrow{M}(T_e(t)) \mid = \begin{cases} M_s\sqrt{1-\Big(\frac{T_e(t)}{T_c}\Big)^2} & T_e \leq T_c \\ 0 & T_e > T_c \end{cases} \tag{3.7}$$

where T_e is the electronic temperature calculated from the two temperature model, and T_c the Curie temperature.

For the anisotropy constants there exist different models that account for their variation with the temperature (Staunton et al. [2004]; Zener [1954]). For example, the iron magneto−crystalline dependance on temperature is given by (Morrish [1966]):

$$K_1(T) = K_1(0)\Big[\frac{\mid \overrightarrow{M}(T) \mid}{M(0)}\Big]^{10} \tag{3.8}$$

where $K_1(0)$ and M(0) are the anisotropy and the magnetization at the absolute zero.

In the following, we will be concerned by the laser induced dynamics in magnetic nanoparticles such as the thermalization of the spins taking place at femtosecond timescales, their corresponding relaxation to the equilibrium position. Besides, we aim to explore the precession dynamics of the magnetization vector during its return to its equilibrium position.

Chapter 4

Experimental

4.1 Polarization of Light

Light is treated as a transverse electromagnetic wave. The polarization is a physical property of a wave that describes the orientation of the electric field of an electromagnetic wave as it propagates.

4.1.1 States of Polarization

Basically, three types of polarization states are generally considered: linear, circular and elliptical. Consider two waves traveling in the z−direction with a relative phase difference ε :

$$\begin{aligned} \overrightarrow{E}_x(z,t) &= \overrightarrow{i}\, E_{0x} cos(kz - \omega t) \\ \overrightarrow{E}_y(z,t) &= \overrightarrow{j}\, E_{0y} cos(kz - \omega t + \varepsilon) \end{aligned}$$

The resultant wave is the vector sum of the two waves :

$$\overrightarrow{E}(z,t) = \overrightarrow{E}_x(z,t) + \overrightarrow{E}_y(z,t) \tag{4.1}$$

4.1.1.1 Linear Polarization

The resultant wave is said to be linearly polarized, if the orientation of the field does not change during its propagation with a constant phase ε i.e. ε should be

a multiple of 2π.

- if ε=$\pm 2n\pi \Rightarrow \overrightarrow{E}$(z,t)=($\overrightarrow{i}\,E_{0x}$+$\overrightarrow{j}\,E_{0y}$)cos(kz−$\omega$ t)
- if ε=$\pm 2(n+1)\pi \Rightarrow \overrightarrow{E}$(z,t)=($\overrightarrow{i}\,E_{0x}$-$\overrightarrow{j}\,E_{0y}$)cos(kz−$\omega$ t)

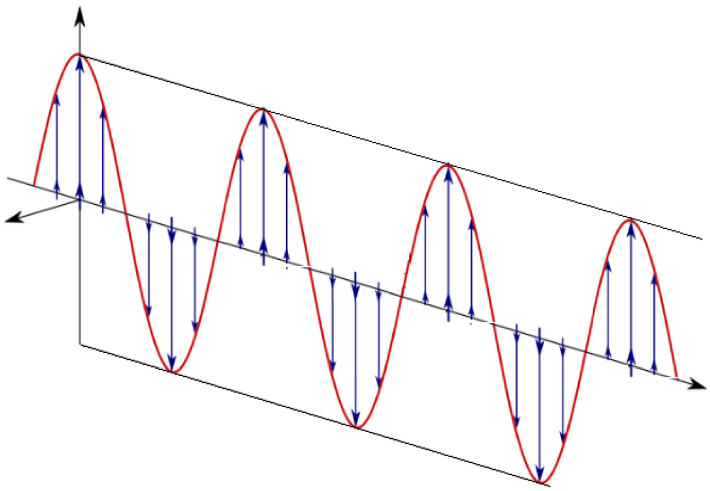

Figure 4.1: A linearly polarized light.

4.1.1.2 Circular Polarization

If the orientation of the electric field rotates with a constant magnitude, then the resultant wave will be circularly polarized. Depending on the direction of rotation, we distinguish between two types of circular polarization :

- **Right circular polarized light** :

$$\varepsilon = +\tfrac{\pi}{2} \Rightarrow \overrightarrow{E}(z,t) = \overrightarrow{E}_0(z,t)(\overrightarrow{i}\cos(kz-\omega t) + \overrightarrow{j}\sin(kz-\omega t)$$

- **Left circular polarized light** :

$$\varepsilon = -\tfrac{\pi}{2} \Rightarrow \overrightarrow{E}(z,t) = \overrightarrow{E}_0(z,t)(\overrightarrow{i}\cos(kz-\omega t) - \overrightarrow{j}\sin(kz-\omega t)$$

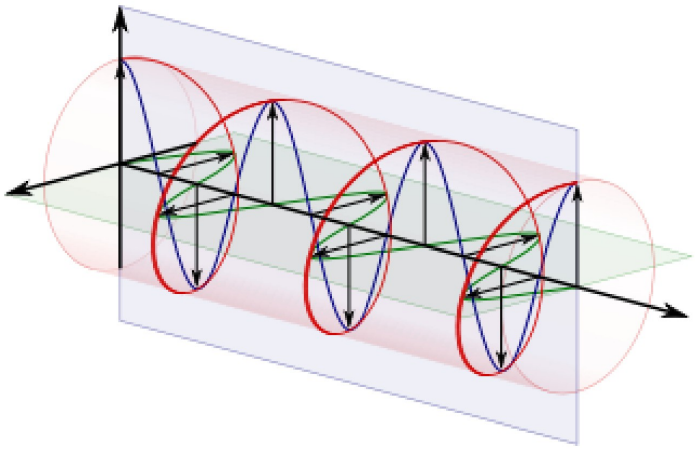

Figure 4.2: A circularly polarized light.

4.1.1.3 Elliptical Polarization

The linear and the circular polarizations are two special cases of the elliptical polarization. The orientation of the electric field rotates and the magnitude changes as well during the propagation of the wave. The polarization of the resultant wave describes an ellipse making an angle α with (E_x, E_y) whose equation is :

$$\left(\frac{E_x}{E_{0x}}\right)^2 + \left(\frac{E_y}{E_{0y}}\right)^2 - 2\left(\frac{E_x}{E_{0x}}\right)\left(\frac{E_y}{E_{0y}}\right)\cos(\varepsilon) = \sin^2(\varepsilon) \tag{4.2}$$

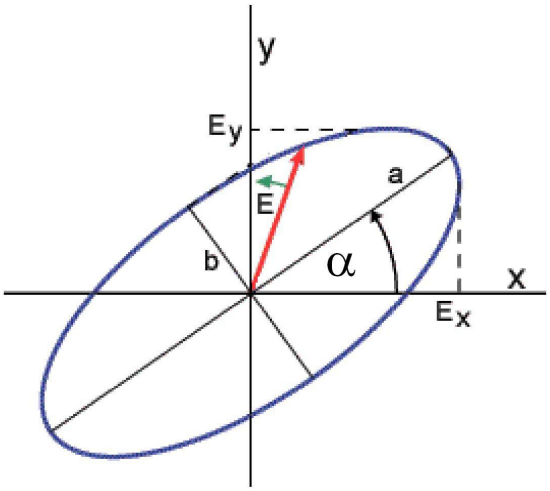

Figure 4.3: An elliptically polarized light.

the angle alpha is given by

$$tang(2\alpha) = \frac{2E_{0x}E_{0y}\cos(\varepsilon)}{E_{0x}^2 E_{0y}^2} \tag{4.3}$$

According to the values of ε, we distinguish between two types of elliptical polarization :

- $0 < \varepsilon < \pi \Rightarrow$ counter-clock wise elliptical polarization.
- $\pi < \varepsilon < 2\pi \Rightarrow$ clock wise elliptical polarization.

4.1.2 Some Useful Definitions

In this section, we present some useful definitions of some keywords used throughout this Chapter :

1. **Rotation** : is the rotation angle of the plane of polarization of a linearly polarized light as it passes through a magnetized material.
2. **Ellipticity** : is ratio of the major axis to the minor axis of an ellipse.

3. **Birefringence** : is the decomposition of a light ray into two rays ordinary and extraordinary when it traverses certain anisotropic materials. It was first observed by Rasmus Bartholin in 1669 in calcite.

4. **Circular Dichroism** : is the differential absorption of the left circular polarized light (LCP) and the right circular polarized light (RCP). It was discovered by Jean−Baptiste Biot, Augustin Fresnel, and Aimé Cotton.

4.2 Magneto−Optical Effects

Magneto−Optical effect is now a widely used physical method to explore the properties of magnetic materials. The Magneto−Optical effects described here were first discovered by Michael Faraday , (FARADAY EFFECT) observed in transmission through a glass (Faraday [1846]) and the reverend J. C. Kerr (KERR EFFECT) observed on the reflection off a metal (Kerr [1877]) . Therefore, the effects for transmitted light are called Faraday effects and for reflected light are called Kerr effects.

4.2.1 Faraday Effects

The experiment of Faraday consisted in measuring the transmission of an incident polarized light through a glass rod under an applied magnetic field. In particular, he observed that the polarization plane rotates by a angle depending on the magnetic field (see figure 4.4). The Faraday effect was one of the earliest indications of the interaction between magnetism and light (Hecht [2002]).

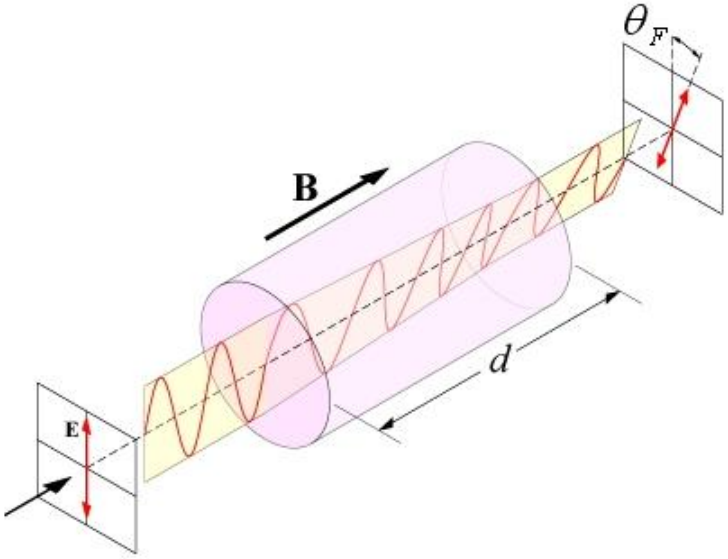

Figure 4.4: The Magneto−Optical Faraday effect where θ_F is the angle of rotation (in radians), B is the magnetic flux density in the direction of propagation (in tesla), d is the length of the path (in meters) where the light and magnetic field interact.(http://en.wikipedia.org/wiki/Optical isolator)

4.2.2 Kerr Effects

In 1877, the Rev. John Kerr observed that when linearly polarized light is reflected from the polished surface of a magnetized sample, its polarization rotates and becomes slightly elliptical (see figure 4.5). Although these effects are important in magnetic media (ferro−magnetic or ferri−magnetic), they are still small and often difficult to detect.

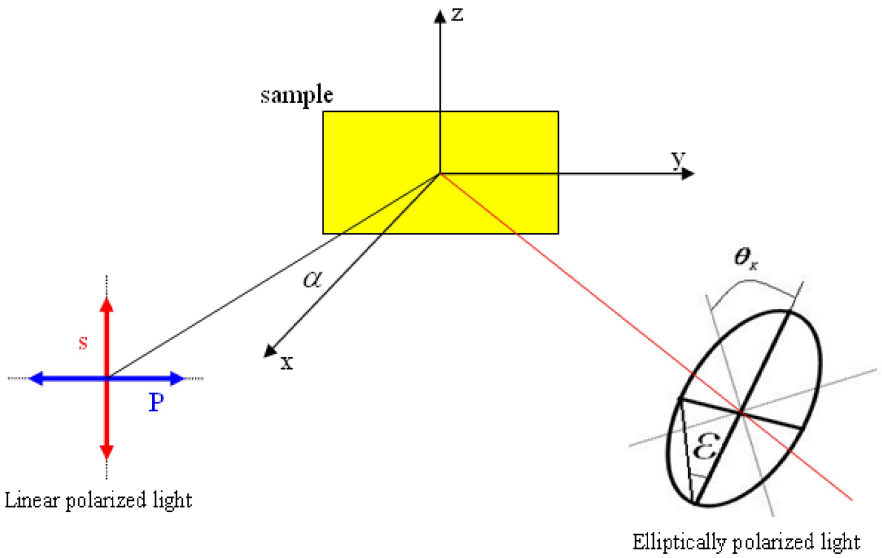

Figure 4.5: The Magneto−Optical Kerr effect.

4.2.3 The Physics of the Magneto−Optical Effects

Microscopically, it is the spin orbit interaction that stands behind the MO effects in metals. The hamiltonian of this interaction is of the form :

$$\boldsymbol{H}_{SO} = \frac{\hbar}{4m^2c^2}(\overrightarrow{\nabla}V \wedge \overrightarrow{P}) \cdot \overrightarrow{\sigma} \tag{4.4}$$

As long as the MO effects are related to the electric current produced by the mobile electrons, the Heisenberg exchange interactions cannot explain such effects because the Molecular field influences the alignment of the moments rather than the motion of the electrons.
In 1932, Hulme stated that the spin−orbit interaction couples the electron magnetic moment $\overrightarrow{\sigma}$ with the magnetic field $(\overrightarrow{\nabla}V \wedge \overrightarrow{P})$that the electron 'sees' when moving with a momentum $\overrightarrow{P}$ through the electric field $-\overrightarrow{\nabla}V$ inside a medium (Argyres [1955]; Hulme [1932]). This coupling of the motion of an electron to its magnetic moment could be responsible for the connection of the optical and magnetic properties of ferromagnets.

In a more general description, the induced ellipticity and rotation of the reflected or transmitted light beam may be referred to the birefringence and circular dichroism in the magnetic materials. Indeed, a linearly polarized light may be written as a superposition of RCP and LCP waves. In a magnetic material, these two waves propagate with different velocities, leading to a rotation of the plane of polarization of the light beam. In addition, these two waves undergo different absorption rates causing the wave to acquire a finite ellipticity.
Starting from the Maxwell's equations, we write down the equation of propagation of a monochromatic wave $\overrightarrow{E}(\overrightarrow{r},\omega)$ with frequency ω in a thin magnetic film:

$$\overrightarrow{\nabla}\wedge\overrightarrow{\nabla}\wedge\overrightarrow{E}(\overrightarrow{r},\omega)=-\frac{\omega^2}{c^2}\left(\overrightarrow{E}(\overrightarrow{r},\omega)+4\pi\overrightarrow{P}(\overrightarrow{r},\omega)+\frac{4\pi ci}{\omega}\overrightarrow{\nabla}\wedge\overrightarrow{M}(\overrightarrow{r},\omega)\right) \quad (4.5)$$

The polarization could be separated into optical $\overrightarrow{P}$ and magneto−optical $\overrightarrow{M}$ which in turn are separated into linear and nonlinear :

$$\begin{aligned}\overrightarrow{P}(\overrightarrow{r},\omega) &= \overrightarrow{P}^{L}(\overrightarrow{r},\omega)+\overrightarrow{P}^{NL}(\overrightarrow{r},\omega)\\ \overrightarrow{M}(\overrightarrow{r},\omega) &= \overrightarrow{M}^{L}(\overrightarrow{r},\omega)+\overrightarrow{M}^{NL}(\overrightarrow{r},\omega)\end{aligned}$$

In the magneto−optical experiments, the first order $\chi^{(1)}$ and the third order $\chi^{(3)}$, linear and nonlinear susceptibility tensors are defined as follows (Bigot [2001]):

$$\begin{aligned}P_i^{(1)}(\omega) &= \sum_j \chi_{ij}^{(1)}(\omega)E_j(\omega) \quad (4.6)\\ P_i^{(3)}(\omega) &= \sum_{jkl} \wp\chi_{ijkl}^{(3)}(\omega;\omega_1,\omega_2,\omega_3)E_j(\omega_1)E_k(\omega_2)E_l(\omega_3)\\ M_i^{(1)}(\omega) &= \sum_j \chi_{ij\nu}^{(1)MO}(\omega)E_j(\omega)H_\nu\\ M_i^{(3)}(\omega) &= \sum_{jkl} \wp\chi_{ijkl\nu}^{(3)MO}(\omega;\omega_1,\omega_2,\omega_3)E_j(\omega_1)E_k(\omega_2)E_l(\omega_3)H_\nu\end{aligned}$$

$$\omega=\omega_1+\omega_2+\omega_3$$

where the indices i, j, k refer to the components of the electric fields and ν to those of the magnetic field (or magnetization direction for a ferromagnetic film)

and $\wp$ indicates the permutations of the fields. The superscript MO is meant to distinguish between the optical and magneto-optical responses.
The MO effects are proportional to the ratio of the non−diagonal and diagonal components of the dielectric tensor ϵ. The dielectric tensor of a given material can be obtained from the solution of the equation of free electrons given by Drude model with a Lorentz force $-e(\overrightarrow{E} + \overrightarrow{v} \wedge \overrightarrow{B})$ and a friction force $-\frac{m}{\tau'}\overrightarrow{v}$ where τ' is the electron mean free path.
For isotropic materials, the dielectric tensor reads (You and Shin [1998]) :

$$\epsilon = \epsilon_{xx} \begin{pmatrix} 1 & -iQm_z & iQm_y \\ iQm_z & 1 & -iQm_x \\ -iQm_y & iQm_x & 1 \end{pmatrix} \tag{4.7}$$

where Q is called the magneto−optical constant, and $\overrightarrow{m}$ is the unit magnetization vector. In some notations, Qm_i (i=x,y,z), is often replaced by $\widetilde{Q}$ and called the voigt vector with three components $\widetilde{Q}_x$, $\widetilde{Q}_y$, $\widetilde{Q}_z$, where $\widetilde{Q}$ is defined as follows :

$$\widetilde{Q} = -i\frac{\widetilde{\epsilon}_{xy}}{\widetilde{\epsilon}_{xx}} = q' + iq'' \quad where \quad \widetilde{\epsilon}_{xx} = \epsilon'_{xx} + i\epsilon''_{xx}$$

The two normal modes are the LCP wave with refraction index :

$$n_L = n(1 - \frac{1}{2}\widetilde{Q} \cdot \overrightarrow{K})$$

and the RCP with refraction index :

$$n_R = n(1 + \frac{1}{2}\widetilde{Q} \cdot \overrightarrow{K})$$

where $n = \sqrt{\epsilon}$. The linear MO effects originates from the non−zero difference between n_L and n_R. In the case of normal incidence of the incident light (parallel to the normal of the sample), the complex Kerr polarization angle is found to be equal to :

$$\Phi_K = \theta_K + i\eta_K = i\frac{N_L - N_R}{1 - N_L N_R} = -i\frac{\epsilon_{xy}^{(1)MO}}{(\epsilon_{xx}^{(1)MO} - 1)\sqrt{\epsilon_{xx}^{(1)MO}}} \tag{4.8}$$

- θ_K=$Re(\Phi_K)$ is the Kerr rotation.
- η_K=$Im(\Phi_K)$ is the Kerr ellipticity.

In the case of the non linear MO effects, the analytical solution of equations (4.5) and (4.6) is not trivial and the problem is complicated.
Since our experiments are based on the Magneto−Optical effects in reflection, in the following we will concentrate on the physics of the Magneto−Optical Kerr effects (MOKE).

4.2.4 Magneto−Optical Kerr Effects

The Magneto−Optical Kerr Effect (MOKE) is the modification of the reflection of polarized light by a material sample under a magnetic field. This modification can be observed with several configurations, including 1) rotation of the direction of polarization of the light, 2) introduction of ellipticity in the reflected beam and 3) a change in the intensity of the reflected beam. The rotation and ellipticity of the reflected light polarization are proportional to the magnetization.
In fact, MOKE can be divided into three configurations according to the direction of the magnetization with respect to the plane of incidence and to the reflecting surface: the longitudinal orientation figure 4.6−A, the polar orientation figure 4.6−B , and the transverse orientation figure 4.6−C.

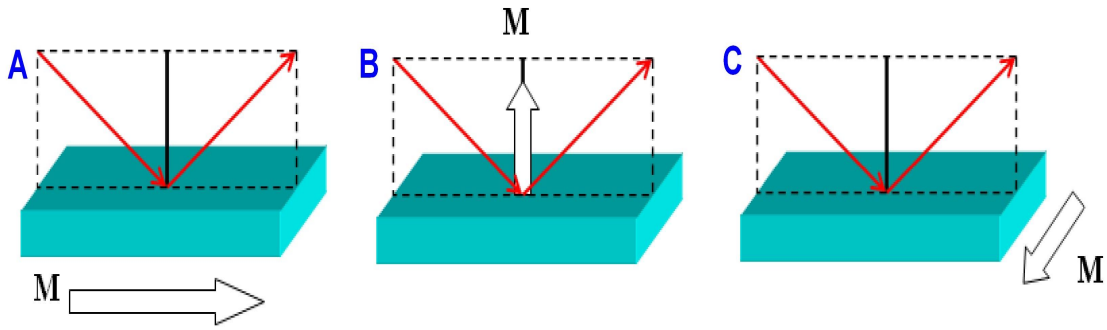

Figure 4.6: The Magneto−optical Kerr effect configurations: A−Longitudinal B−Polar, and C−Transverse.

4.2.4.1 The Magneto−optical Kerr effect configurations

In the longitudinal case, the magnetization vector is in the plane of the surface and parallel to the plane of incidence whereas in the polar case the magnetization vector is perpendicular to the plane of the surface. The effect is simple and occurs for P−polarized incident light ($\overrightarrow{E}$ parallel to the plane of incidence) or the S−polarized ($\overrightarrow{E}$ perpendicular to the plane of incidence). The major axis of the ellipse is often rotated slightly with respect to the principal plane and this is referred to as the Kerr rotation. There is an associated ellipticity called the Kerr ellipticity. The sign and magnitude of these effects are proportional to the magnetization $\overrightarrow{M}$.
The transverse case is quite different from the previous two. First, there is only an effect for light polarized in the P−plane. Secondly, in such a case, the reflected light remains linearly polarized and there is only a change in reflected (or transmitted) amplitude as the magnetization is reversed.

4.2.4.2 Jones Formalism

The complex kerr angle Φ_K can be calculated from the fresnel reflection matrix $\Re$ which is obtained following the Jones formalism.

$$\begin{pmatrix} E_p^r \\ E_s^r \end{pmatrix} = \Re \begin{pmatrix} E_p^i \\ E_s^i \end{pmatrix} = \begin{pmatrix} r_{pp} & r_{ps} \\ r_{sp} & r_{ss} \end{pmatrix} \begin{pmatrix} E_p^i \\ E_s^i \end{pmatrix} \tag{4.9}$$

r_{ij} represents the ratio of the incident j to the reflected i polarized electric field. As an example of calculations, we show the Fresnel coefficients for a thin magnetic film.

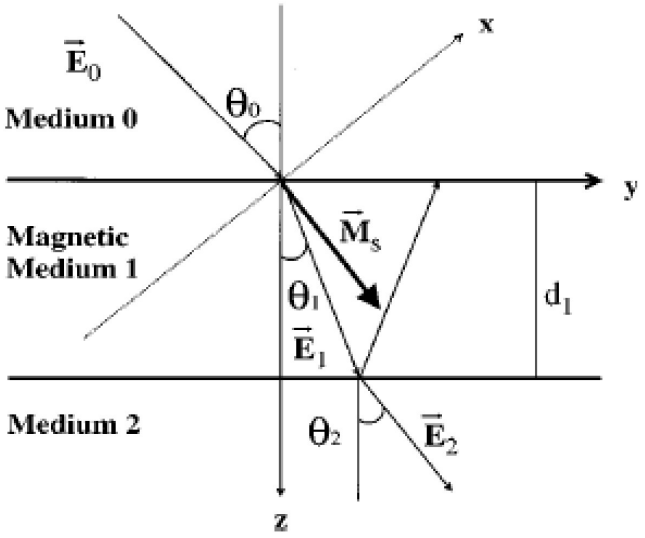

Figure 4.7: A system constituted of the nonmagnetic medium 0, the magnetic medium 1, and the nonmagnetic medium 2. The thickness of medium 1 is d_1 . The magnetization direction of the medium 1 is arbitrary (You and Shin [1998]).

The expressions of r_{ij} are (You and Shin [1998]):

$$
\begin{aligned}
r_{pp} &= \frac{n_s\cos\theta_0 - n_0\cos\theta_2}{n_s\cos\theta_0 + n_0\cos\theta_2} + i\frac{4\pi n_0 d_1\cos\theta_0\left(n_s^2\cos^2\theta_1 - n_1^2\cos^2\theta_2\right)}{\lambda\left(n_0\cos\theta_2 + n_s\cos\theta_0\right)^2} \\
r_{sp} &= \frac{4\pi n_0 n_1 Q d_1\cos\theta_0\left(m_z n_1\cos\theta_2 + m_y n_s\sin\theta_1\right)}{\lambda\left(n_0\cos\theta_0 + n_s\cos\theta_2\right)\left(n_0\cos\theta_2 + n_s\cos\theta_0\right)} \\
r_{ss} &= \frac{n_0\cos\theta_0 - n_s\cos\theta_2}{n_0\cos\theta_0 + n_s\cos\theta_2} + i\frac{4\pi n_0 d_1\cos\theta_0\left(n_1^2\cos^2\theta_1 - n_s^2\cos^2\theta_2\right)}{\lambda\left(n_0\cos\theta_0 + n_s\cos\theta_2\right)^2} \\
r_{ps} &= \frac{4\pi n_0 n_1 Q d_1\cos\theta_0\left(m_z n_1\cos\theta_2 - m_y n_s\sin\theta_1\right)}{\lambda\left(n_0\cos\theta_0 + n_s\cos\theta_2\right)\left(n_0\cos\theta_2 + n_s\cos\theta_0\right)}
\end{aligned}
$$

where n_0, n_1 and n_s are the refractive indices of media 0, 1 and 2 respectively. The complex Kerr angle for S− and P−polarizations is defined as follows :

- $\Phi_K^s = \theta_K^s + i\eta_K^s = \frac{r_{ps}}{r_{ss}}$
- $\Phi_K^p = \theta_K^p + i\eta_K^p = \frac{r_{sp}}{r_{pp}}$

For a polar configuration i.e. $(m_z = 1, m_x = m_y = 0)$, the Kerr angle reads :

$$\begin{aligned} \Phi^s_{K,pol} &= \left(\frac{r_{ps}}{r_{ss}}\right)_{pol} = \frac{-\cos\theta_0}{\cos(\theta_0 - \theta_2)} \cdot \cos\theta_2 \cdot \aleph \\ \Phi^p_{K,pol} &= \left(\frac{r_{sp}}{r_{pp}}\right)_{pol} = \frac{\cos\theta_0}{\cos(\theta_0 + \theta_2)} \cdot \cos\theta_2 \cdot \aleph \end{aligned}$$

$\aleph$ depends on the thickness of the magnetic medium

$$\aleph = \frac{4\pi n_0 n_1^2 Q d_1}{\lambda(n_2^2 - n_0^2)}$$

4.3 Pump−Probe Spectroscopy

The Pump Probe spectroscopy performed with femtosecond laser pulses has turned to be a performant technique to study ultrashort dynamical magnetic processes. The method uses two ultrashort laser pulses : an intense laser pulse called the pump and a relatively less intense pulse called the probe. The basic idea is that the perturbations in the state of a given system induced by the pump beam are investigated using the probe beam at different time delays.
For our experimental measurements, we have excited the samples with a 400 nm/150 fs pump pulse and probed with a 800 nm/150 fs. The description of the laser setup will come later on in this chapter.

In a two level systems formed of a ground state and an excited state, the pump beam induces a transfer of populations from the ground state to the excited state leading to a change in the absorption of the excited sample which induces a change in the transmissivity or reflectivity. This effect can be detected by measuring the differential variation of the intensity of the transmitted or reflected beam :

$$\frac{\Delta I}{I} = \frac{I_{pr}^{pu} - I_{pr}}{I_{pr}} \qquad I \sim T, R \tag{4.10}$$

- I_{pr}^{pu} : intensity of the probe in the presence of the pump.
- I_{pr} : intensity of the probe in the absence of the pump.

For weak absorption, the variation of the transmissivity or reflectivity is proportional to the absorption coefficient :

$$\frac{\Delta I}{I} \propto -\Delta\alpha(\omega) \quad with \quad I_t(w) = I_0 e^{-\alpha(\omega)d} \tag{4.11}$$

where d is the thickness of the sample and I_0 is the incident intensity. In the case of weak optical excitation, Rosei and Lynch [1972] showed that the real and imaginary parts of the dielectric tensor can be written as linear combinations of $\frac{\Delta R}{R}$ & $\frac{\Delta T}{T}$:

$$\begin{aligned} \Delta\epsilon_1 &= A\frac{\Delta T}{T} + B\frac{\Delta R}{R} \\ \Delta\epsilon_2 &= C\frac{\Delta T}{T} + D\frac{\Delta R}{R} \end{aligned}$$

A, B, C and D are parameters that depend on the wavelength of the excitation, film thickness and the index of refraction of the medium.
In pump−probe experiments, the effects of the pulses has to be expressed in terms of the changes of the third order nonlinear susceptibility tensor $\chi^{(3)}$:

$$P_l^{(3)}(\omega_s) \propto \sum_{ijkl} \wp\chi_{ijk}^{(3)}(\omega_s;\omega_i,\omega_j,\omega_k)E_i(\omega_i)E_j^*(\omega_j)E_k(\omega_k)$$

where i, j, k stands for pr (probe) or (pu) pump beams with the condition to have two prump and one probe laser pulses. It is clear from $P_l^{(3)}$ that different permutations of i, j, k can be obtained. However, as in our detection of the reflected or transmitted beam is done is the direction of the probe, then only three effective permutations are to be considered:

1. In the negative time delays, we have $E_{pr}E_{pu}^*E_{pu}$.
2. During the superposition of the two pulses, we have $E_{pu}E_{pr}^*E_{pu}$ and it is called the coherent term.

3. In the positive time delays, we have $E_{pu}E_{pu}^{*}E_{pr}$.

4.4 The Laser system

In the experiments, we have used an amplified laser system from Spectra physics (Tsunami and Spitfire). The oscillator (Tsunami) (figure **??**) delivers pulses at 800 nm with 80 fs duration, a rate of 82 MHz, and an average output power of 600 mW. The energy per pulse is about 7.3 nJ. A continuous laser (Millenia) is used to pump the Tsunami cavity, and another pulsed laser (Evolution X) is used to pump the regenerative amplifier cavity (Spitfire).
The pulses are amplified using a regenerative amplifier with also a Ti:sapphire slab as a gain medium. The output of the amplifier delivers an average power of ∼650 μW which corresponds to an energy of 200 μJ/pulse which have a pulse duration of 150 fs at 5 kHz.

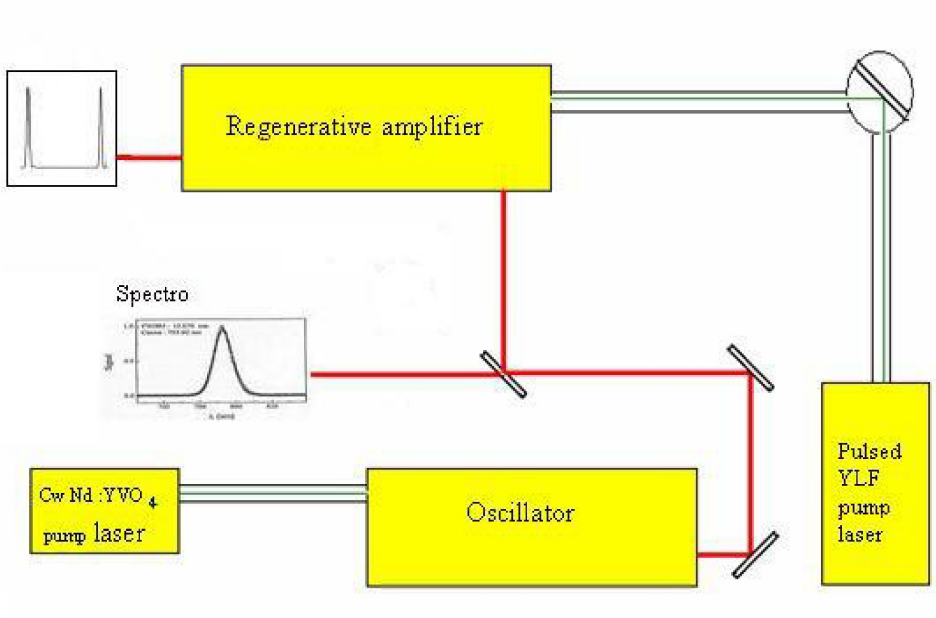

Figure 4.8: A sketch of the laser system.

We use fast photodiodes and an oscilloscope to monitor the pulse train, and a fiber spectrometer for the frequency spectrum.

4.4.1 Ultrashort Laser Pulses

In general, the shorter laser pulses require larger bandwidth. The corresponding relation between a pulse duration Δt and its spectral bandwidth $\Delta\omega$ (optical frequencies necessary to construct it) is given by the time bandwidth product $\Delta t \Delta\omega$. For any laser pulse, the product should be minimum:

$$\Delta t \Delta\omega \geq \frac{1}{2} \tag{4.12}$$

Equation 4.12 is known as the time frequency uncertainty principle. From this equation, we can deduce the relation between the frequency at full half maximum width $\Delta\nu$ and the duration at half maximum :

$$\Delta\nu \Delta\omega \geq K$$

where K is a constant that depends on the shape of the pulse e.g. K=0.441 for a pulse with a gaussian profile.
To generate ultrashort laser pulses, three main factors are to be considered : 1) the gain medium, 2) the compensation of the group velocity dispersion GVD and 3) mode−locking.

1. As mentioned before we have used a regenerative amplifier with Ti^{3+}:sapphire doped medium. The Ti^{3+}:sapphire doped medium provides: 1) large spectral bandwidth (600 nm to 1 μm); 2) good thermal conductivity; and 3) high mechanical and photochemical stability.

2. It is known that as the dispersion properties of the active medium and the optical elements in a laser cavity affects the pulse duration significantly and as the refractive index of any material $n(\omega)$ depends nonlinearly on the frequency therefore, each frequency within the pulse experiences a slightly different group velocity, v_g as it propagates. This effect is known as the

group velocity dispersion GVD.
In fact, the shorter the pulse, the broader the spectral range involved, increasing the influence of GVD on the shape and the duration of the pulse. Therefore, in order to achieve short, stable and reproducible output pulses from a laser, it is necessary to compensate the effects of GVD. Actually, there are two methods for the compensation : the 4 prisms and the diffraction grattings. In femtosecond laser system, the positive GVD is compensated using the 4 prisms.

3. To obtain ultrashort intense laser pulses the phase relationship between the components of the out coming pulse should be fixed. This can be done in a technique called the mode−locking technique.
In general, there exit two main methods of mode−locking : active and passive.

4.5 Brief description of how do we perform our measurements

In order to explore the magnetization dynamics of the $Co_{core}Pt_{shell}$ pellets, we have used a polar magneto−optical kerr configuration (described in section 4.2.4.1) to perform the pump probe measurements.
The measurements are done with a 150 fs/400 nm pump pulse used to excite the sample and a 150 fs/800 nm laser pulse used to probe the modifications in the state of the samples in a function of the time delay between them. The temporal delay between the two pulses is controlled by their relative pathways which is typically done with a precise motorized linear stage with a minimum step of 0.1 μm corresponding to a temporal delay of 6.66 fs. The experimental setup is sketched on the following figure:

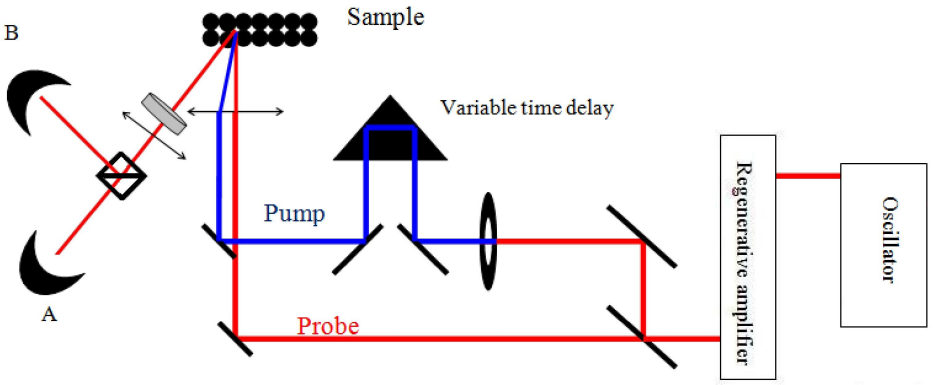

Figure 4.9: A scheme of the experimental setup (A+B gives the reflectivity and A−B gives the magnetization of the sample).

To obtain the laser pulses, we have used a regenerative amplifier which delivers 800 nm/150 fs laser pulses with a 5 kHz repetition rate which corresponds to 200 μs delay between two consecutive pulses. This delay is sufficient so that the sample establishes its thermal equilibrium with the environment. In metals, the heat diffusion process is in the order of nanoseconds.
Then, the output beam is divided into two parts using a beam splitter. The first beam is used as a probe pulse, while the second is used to generate the pump pulse using a 3 mm BBO (beta Barium Borate $\beta - BaB_2O_4$) crystal.
After that the pump and the probe are focused on the samples with an incidence of zero with respect to the normal of the sample. The analysis of the state of polarization of the reflected beam is done using a polarization bridge. The detection of the reflected beam is made on a lock−in amplifier using photodiodes. We perform the measurements on two directions of an external magnetic field $\overrightarrow{H}_0$ applied perpendicular to the sample.

4.5.1 Relation between the magnetization, reflectivity and detected MO signal

The intensity detected by the photodiodes is proportional to the magnetization of the sample.

4.5.1.1 Statics

For a polarimetric configuration composed of the sample and a polarizer, the static intensity $I_{\pm}$ for the opposite directions of magnetization is equal to:

$$I_{\pm} = I_0\Big[\cos\gamma^2 + \sin\gamma^2(\theta^2+\eta^2) \pm 2\theta\sin\gamma\cos\gamma\Big] \tag{4.13}$$

where θ and η are the kerr rotation and ellipticity respectively. γ: angle of the polarizer, I_0: intensity of the initial incident light. We note that equation 4.13 is valid for small values of the θ and η.
If we set γ=π/2-α, and in the limits of small angles, and if we separate the magnetic and non magnetic contribution in the ellipticity and rotation, then equation 4.13 could be written as follows (Bigot et al. [2004]):

$$I_{\pm} = I_0\Big[\alpha^2 - 2\alpha(\theta_0 \pm \theta_M) + (\theta_0^2+\eta_0^2+\theta_M^2+\eta_M^2) \pm 2(\theta_0\theta_M+\eta_0\eta_M)\Big] \tag{4.14}$$

where θ_0, η_0 are the non magnetic rotation and ellipticity induced by the sample. θ_M and η_M are the magneto−optic rotation and ellipticity. All of these quantities are wavelength dependent.

4.5.1.2 Dynamics

The differential signals detected by the lock−in amplifiers are given by :

$$\frac{\Delta M}{M} = \frac{\Delta I(t)_{+H_0} - \Delta I(t)_{-H_0}}{4I_0(t)} \tag{4.15}$$

The relationship between $\Delta M/M$ and the detected signal is given by the following equation (Bigot et al. [2004]):

$$\Delta M/M = -\theta_M(t)\alpha + \theta_M(t)\theta_0 + \eta_M(t)\eta_0 \tag{4.16}$$

4.6 The Samples

In this thesis, we have studied 3D arrangements of CoPt core−shell nanoparticles elaborated by redox transmetalation reactions. In general, such types of reactions describe the exchange of ligands between the metals. The transmetalation reactions produce high quality small size (less than 10 nm) core−shell bimetallic nanoparticles e.g. CoPt, CoAu, CoPd... (Lee et al. [2005]).
The $Co_{core}Pt_{shell}$ nanoparticles were fabricated by our collaborating group at Yonsei University in Seoul (Prof. J. Cheon) on two steps : thermolysis[1] and refluxing[2]. In order to obtain the colloids of cobalt nanoparticles, the inorganic compound Dicobalt octacarbonyl $Co_2(CO)_8$ is thermolyzed in toluene solution. Then, the colloids are refluxed for 8 hours with beta−diketonate complexes of platinum $Pt(hfac)_2$ (hfac=1, 1, 1, 5, 5, 5−hexafluoroacetylacetonate) in a nonane solution containing 0.06 mL of n−dodecyl $C_{12}H_{25}NC$ as a stabilizer. The size dispersion of the particles is approximately 10 %. Finally, the particles are assembled into a compact bulk pellet (1.5 x 1 x 4.5 mm^3) by cold pressing under 160 Pa. The final step was performed in the group of Prof. T.H. Kim at Ewha Womans University in Seoul. The obtained Co_{core} Pt_{shell} nanoparticles have an average diameter of $\sim$ 6.5 nm where $\sim$ 5 nm cobalt resides at the core and is surrounded by a $\sim$1.5 nm platinum shell (Park and Cheon [2001]). The shell to shell distance between two $Co_{core}Pt_{shell}$ nanoparticles is about 0.2 nm.

[1] **Thermolysis**: is the separation of a chemical compound into elements or simpler compounds caused by heat.

[2] **Reflux**: is a technique involving the condensation of vapors and the return of this condensate to the system from which it originated. It is used to supply energy to reactions over a long period of time.

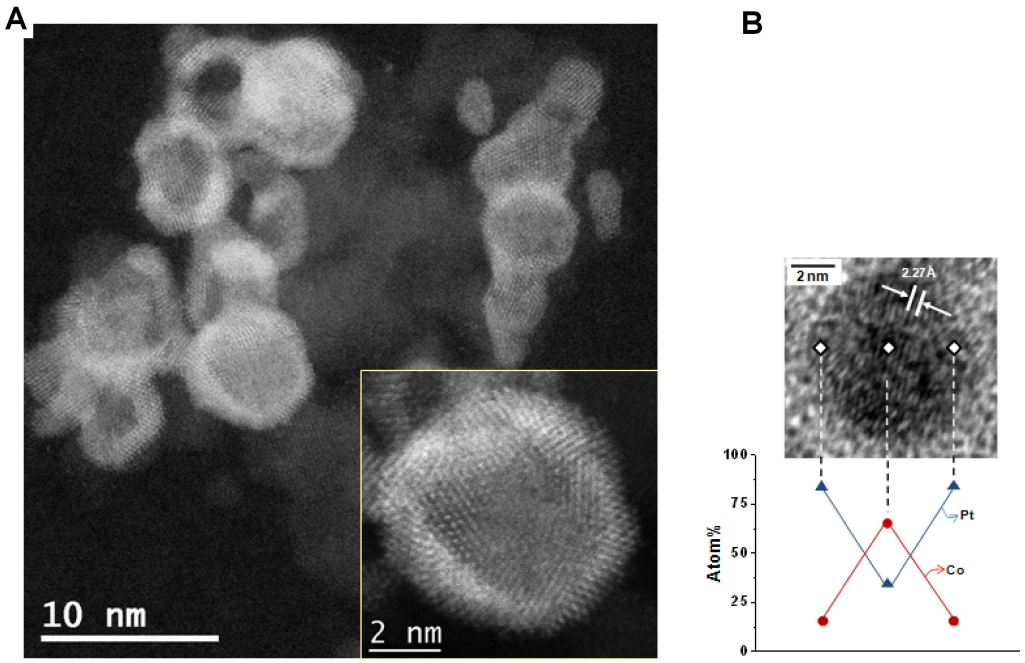

Figure 4.10: A− Electron microscopy image of CoPt core−shell nanoparticles (insert: detailed view of single particle), B− High resolution TEM image and composition analysis of CoPt core−shell nanoparticle at different positions using Energy Dispersive X-ray Spectroscopic(EDS) technique. From the EDS analysis, compositional changes corresponding to the Pt shell (blue rectangles) and Co core (red circles) clearly confirm the CoPt core−shell structure.).

The static magnetic characterization of the samples, such as the Zero Field Cooling/Field Cooling (ZFC/FC) and the hysteresis loops M(H) were performed using a SQUID magnetometer in SQUID lab at the IPCMS by Alain Derory.

4.6.1 The ZFC/FC measurements

In ZFC, the magnetization is measured while cooling the sample from 350 K to 5 K in a zero applied field, then the sample is heated from 5 K to 350 K in the presence of a low magnetic field (typically 50 Oe) which is lower than the saturation field of the samples. The FC measurements are done in a similar way except that the field is applied from the beginning.

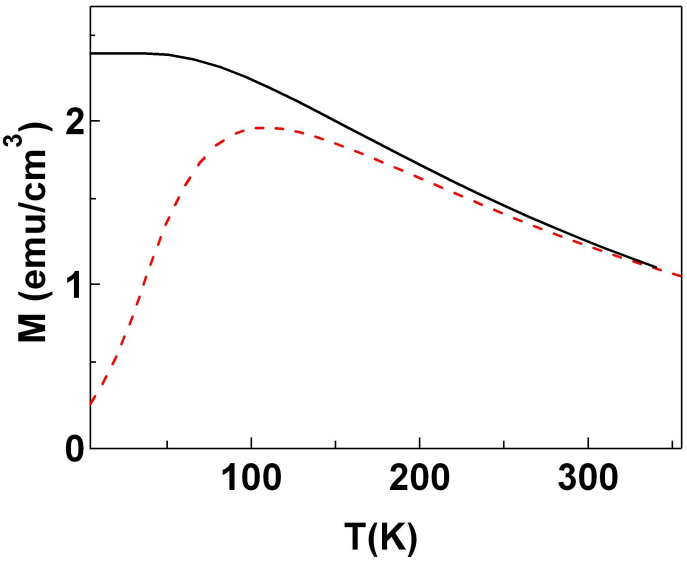

Figure 4.11: Zero-Field-Cooling (ZFC) (dashed lines) / Field-Cooling (FC) (solid lines) Magnetization curve .

The above ZFC/FC curve shows that the nanoparticles are superparamagnetic with a blocking temperature T_B=66 $\pm$ 3 K. The blocking temperature is calculated from the blocking temperature distribution plotted on figure 4.12. The distribution is obtained from the derivative $-\frac{d}{dT}(M_{FC} - M_{ZFC})$ (Denardin et al. [2002]).

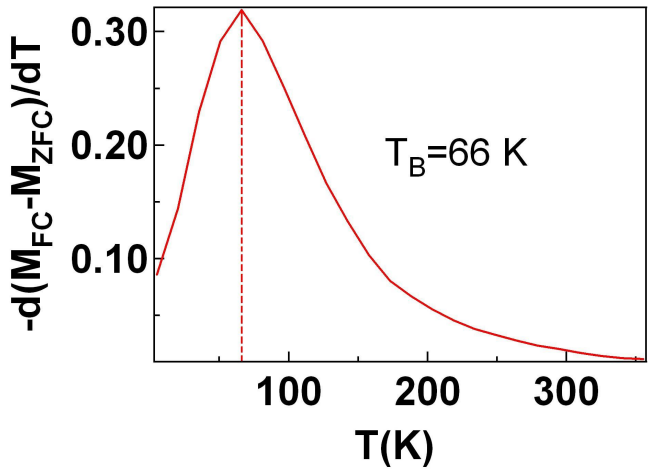

Figure 4.12: The derivative with respect to temperature of the difference between the magnetization obtained by the field cooling M_{FC} and the magnetization obtained by the zero field cooling M_{ZFC}.

4.6.2 The Magnetization curve

To study the dependance of the magnetization $\overrightarrow{M}$ on the external field, we have performed several hysteresis loops measurements for two field directions (// or $\perp$ with respect to $\overrightarrow{M}$) and at different temperatures (5 K and 300 K).

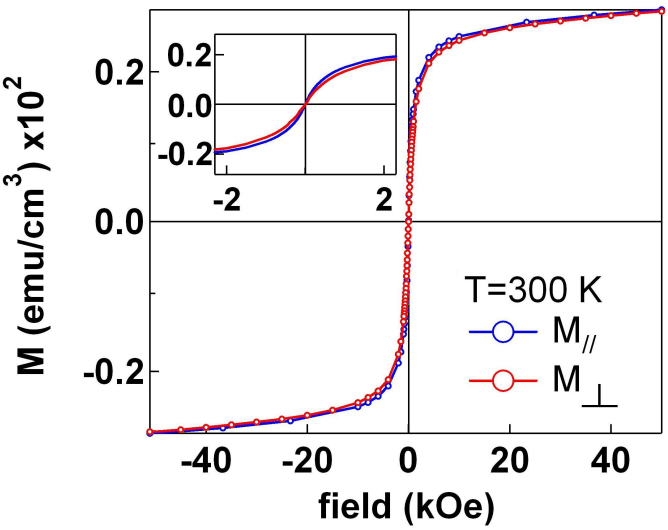

Figure 4.13: Hysteresis loop at 300 K for parallel (blue) and perpendicular (red) directions. Inset: Zooming around zero.

Figure 4.13, shows a typical superparamagnetic hysteresis loop (zero coercive field H_c=0 and zero magnetization at remanence M_R=0), for the two directions of the field confirming the superparamagnetic nature of the particles at room temperature (300 K).

At 5K, for the parallel direction a ferromagnetic hysteresis loop is measured (figure 4.14). For the perpendicular direction, we measure a deformed hysteresis loop which may reflect a competition between individual nanoparticles and the dipolar interactions. From figure 4.15, it is clear that the magnetization at remanence decreases with the weak external applied field (region around the H=0), which is an indication of an anti−parallel alignment of the magnetic moments with respect to the external applied field. This is induced by the dipolar interaction since it favors the anti−ferromagnetic ordering (Arias et al. [2005]). At low temperatures, Kechrakos and Trohidou [2008] have shown that as the strength of the dipolar interaction increases, the magnetization at remanence decreases and for certain strength of dipolar field it attains zero. However, in our case the magnetization at remanence does not arrive at zero, which means that the dipolar interaction are weak so that it does not establish itself properly.

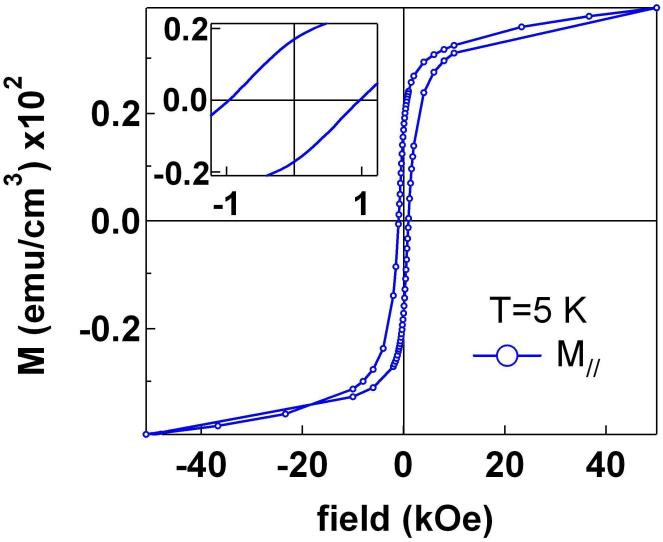

Figure 4.14: Hysteresis loop at 5 K for parallel direction ($M_{//}$). Inset: Zooming around zero.

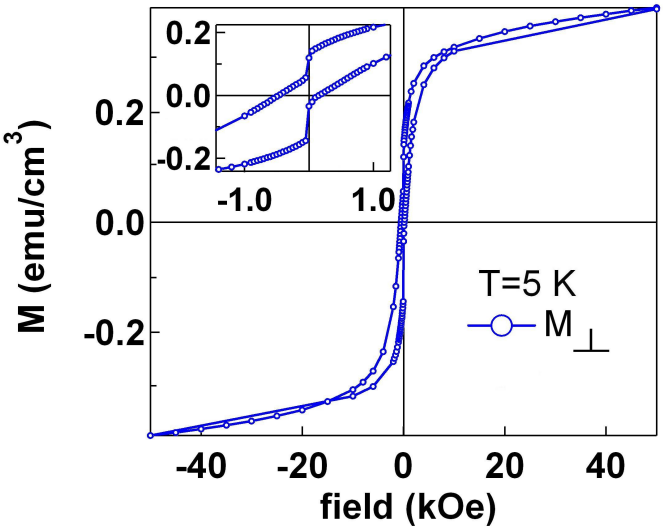

Figure 4.15: Hysteresis loop at 5 K for perpendicular direction ($M_{\perp}$). Inset: Zooming around zero.

The magnetic characteristics of the samples (coercive field, magnetization at

remanence and at saturation) are shown on the following table:

	T [K]	M_R [emu cm^{-3}]		M_S [emu cm^{-3}]		H_C [Oe]	
Orientation of M to sample plane		//	⊥	//	⊥	//	⊥
CoPt core shell (non-annealed)	5	16.9	12,02	39.8	41	1000	93.7
	300	0	0	27	27	0	0

Figure 4.16: Magnetization parameters of the CoPt core-shell nanoparticles. T: Temperature, M_R and M_S: Magnetization at remanence and at saturation, H_c: coercive field, // and ⊥ designate the directions of magnetization M measured parallel and perpendicular to the plane of the pellet sample.

4.6.3 The Annealing of Samples

The samples were annealed at 650 K for one hour in primary vacuum. The thermal annealing derived enormous changes in the magnetic properties of the pellets. For instance, the annealing induced a dilation in the diameter of the particles. More importantly, it led to the formation of CoPt crystalline phase as can be seen from the electron microscope images (figure 4.17).

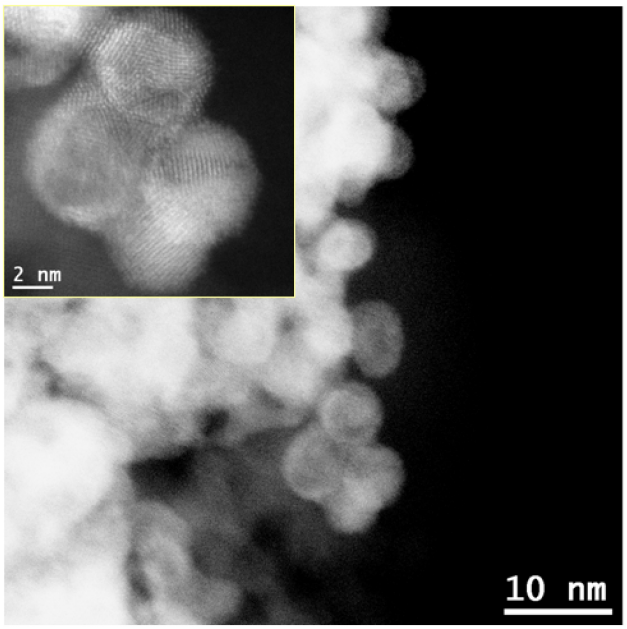

Figure 4.17: Electron microscopy image of CoPt core nanoparticles (insert: detailed view of single particle).

A temperature dependent imaging of an individual nanoparticle assured the enrichment of the cobalt cores with platinum. The evolution of the structure of the nanoparticles from $Co_{core}\ Pt_{shell}$ to a CoPt crystalline phase is shown on the following figure obtained by high-angle annular dark-field scanning transmission electron microscopy (HAADF-STEM):

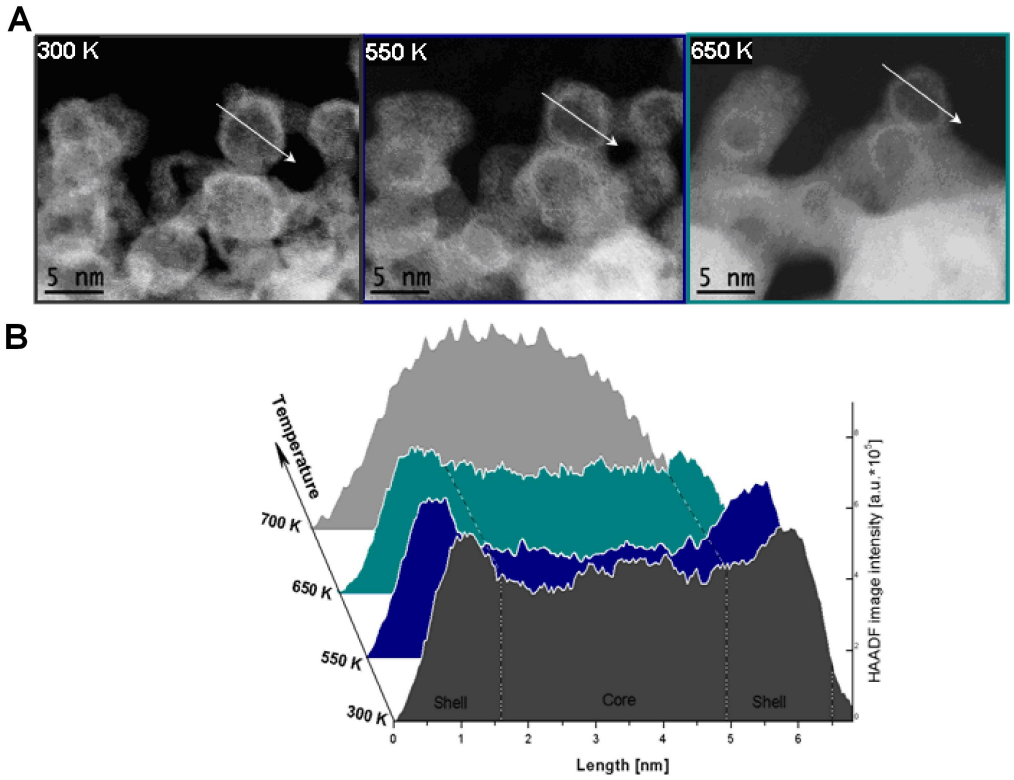

Figure 4.18: Temperature dependent microscopy images of CoPt nanoparticles. A) HAADF images of the pellet showing the evolution of a typical region during thermal treatment up to 650 K. B) Intensity profiles of an individual particle extracted from the HAADF images along the arrow in A. The morphology of a core-shell like nanoparticle (300 K) evolves progressively with the increasing temperature, such that at 700 K the core-shell structure evolves towards a homogenous one.

Here, it is worth to mention that the microscopy characterization of the samples was performed in the Department of Surfaces and Interfaces (DSI) at the IPCMS by S. Moldovan and Ovidiu Ersen. The ZFC/FC curve shows that the blocking temperature is shifted above the the room temperature (T_B >350 K) indicating that the pellets are ferromagnetic at room temperature.

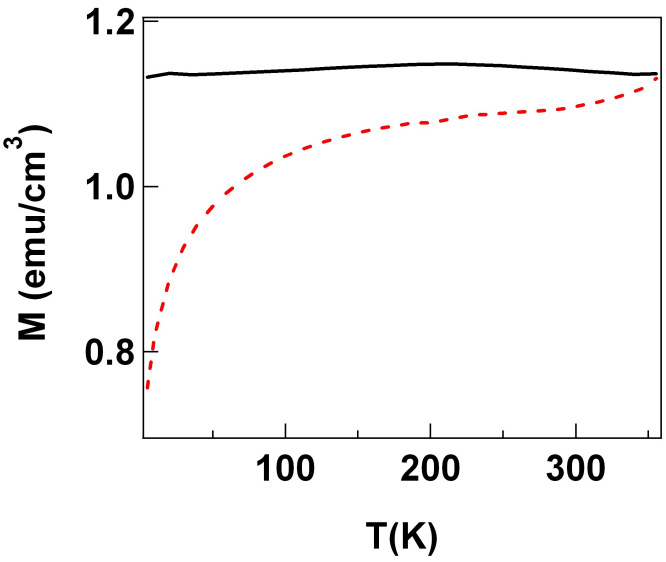

Figure 4.19: Zero-Field-Cooling (ZFC) (dashed lines) / Field-Cooling (FC) (solid lines) Magnetization curve

This phase transition is also seen in the ferromagnetic hysteresis loop measured at 300 K for the $M_{\perp}$ and $M_{//}$ directions.

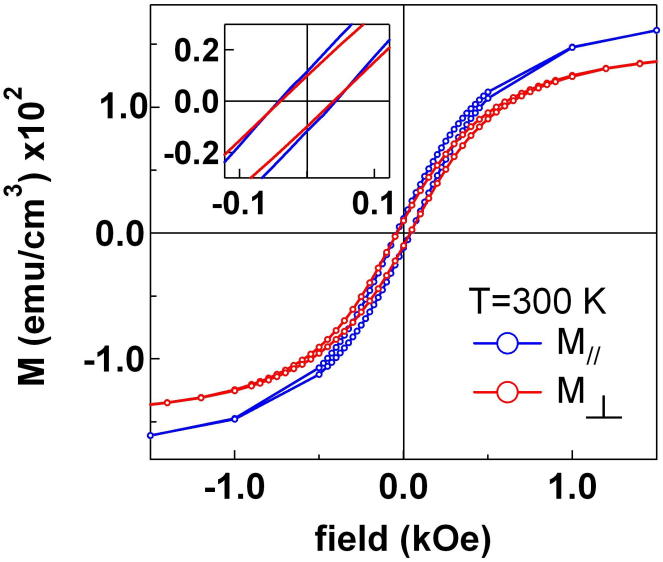

Figure 4.20: Hysteresis loop at 300 K for parallel (blue) and perpendicular (red) directions. Inset: Zooming around zero.

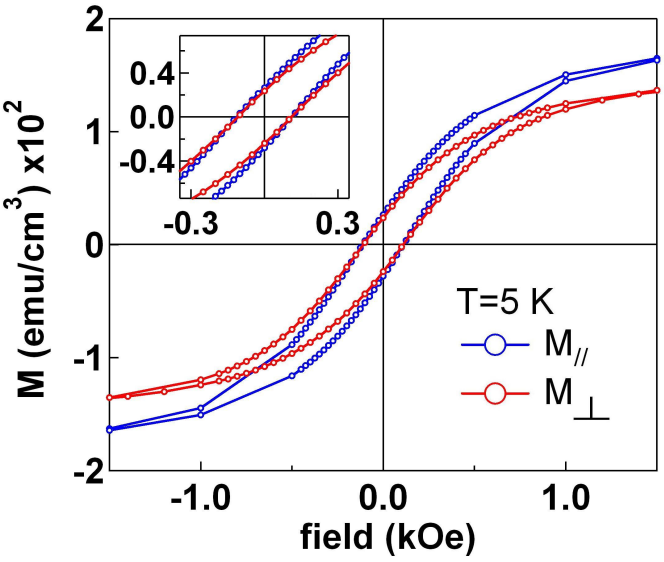

Figure 4.21: Hysteresis loop at 5 K for parallel (blue) and perpendicular (red) directions. Inset: Zooming around zero.

The magnetic characteristics of the non−annealed samples (coercive field, magnetization at remanence and at saturation) are shown on the following table:

	T [K]	M_R [emu cm^{-3}]		M_S [emu cm^{-3}]		H_C [Oe]	
Orientation of M to sample plane		//	⊥	//	⊥	//	⊥
CoPt core shell (annealed 650 K)	5	26.5	23.7	189	156	100	100
	300	11.6	9.9	181	151	50	50

Figure 4.22: Magnetization parameters of the CoPt core-shell nanoparticles. T: Temperature, M_R and M_S: Magnetization at remanence and at saturation, H_c: coercive field, // and ⊥ designate the directions of magnetization M measured parallel and perpendicular to the plane of the pellet sample.

The induced ferromagnetism in the annealed pellets is attributed to the increase of the magneto−crystalline anisotropy from $Co_{core}Pt_{shell}$ nanoparticles to the CoPt crystalline nanoparticles.
To calculate the increase of the anisotropy constant K_1, we use the blocking temperature T_B and the volume V of the nanoparticle. We have:

$$K_{1_{core/shell}} = \frac{30.1 K_B T_B}{V} = 4.2\ m^5\ J/m^3 \quad for\ T_B = 66K \quad and\ V = 6.65^{-26}\ m^3$$

$$K_{1_{core/shell}} = \frac{30.1 K_B T_B}{V} = 5.4 \cdot\ 10^5\ J/m^3 \quad for\ T_B = 350K \quad and\ V = 2.68^{-26} \cdot\ 10^3$$

Assuming the same temperature as in the bulk Co (Paige and tanner [1984]), then:

$$K_{1_{core/shell}} \approx 0.38 K_{1_{CoPt}} \tag{4.17}$$

N.B. To obtain the factor 30.1 we use the relaxation time given by equation 2.8. The measurement time τ is 120 s and τ_0=10 ps calculated from the pre-exponential factor of equation 2.47 using the physical parameters of the samples (K=4.2 x10^5 Jm^{-3} and M_s=150 x10^3 Am^{-1}).

In the next chapter, we will show the magnetization differential signals obtained on different time scales on the pellets.

Chapter 5

Results and Discussions

We have performed Polar Time Resolved Magneto Optical Kerr Effect (TR−MOKE) measurements with 150 fs pulses at 400 nm for the pump and 800 nm for the probe to study the magnetization and the charge dynamics in Co_{core} Pt_{shell} nanoparticles.

In the polar configuration, the pump and the probe are focused onto the sample with normal incidence where the external field is applied perpendicular to the surface of the sample. The detection of the reflected signal is made by synchronous detection on a lock−in amplifier using a polarization bridge and photodiodes. The advantage of TR−MOKE is that it allows to study the magnetization and the charge dynamics at the same time. To extract the magnetization and the reflectivity, we use the equations:

$$\begin{aligned} \frac{\Delta M}{M} &= \frac{\Delta I(t)_{+H_0} - \Delta I(t)_{-H_0}}{M_{stat}} \\ \frac{\Delta R}{R} &= \frac{\Delta I(t)_{+H_0}}{R_{stat}} = \frac{\Delta I(t)_{-H_0}}{R_{stat}} \end{aligned}$$

The samples (non−annealed and annealed) are studied on three different time scales: where hereafter we name 1) very short time scale (-200 to 600 fs); 2) short time scale (-1 to 3.5 ps); and 3) long time scale (-20 ps to 300 ps). The results are presented on two sections, the first corresponds to the non−annealed samples whereas the second is devoted for the annealed samples.

5.1 Non−annealed Samples

5.1.1 Charge Dynamics

The obtained reflectivity curves, corresponds to the charge dynamics described in chapter 3 section 3.2.1. The absorption of an intense laser pulse drives a gas of electrons above the Fermi level, which relaxes to a hot Fermi−Dirac distribution undergoing electron−electron scattering processes with a characteristic time τ_{c-th}=160 ± 5 fs[1] for a pump energy Ep=0.8 mJ/cm^2. Then, the hot electron gas cools down to the lattice via electron−phonon scattering processes with a characteristic time τ_{c-rel}=1.34 ± 0.03 ps[2]. This exchange of energy with the lattice heats up the nanoparticles, so that the oscillations observed with a period T_{vib}=1.95 ± 0.1 ps corresponds to a spherical breathing mode of the individual nanoparticles which is a well known vibrational process in metallic nanoparticles (Del Fatti et al. [1999]; Hodak et al. [2000]; Link and El Sayed [1999]; Nisoli et al. [1997]). The $\Delta R(t)/R(t)$ on figure 5.1−B is fitted with a damped cosine function of the form

$$\Big(\frac{\Delta R}{R}\Big)(t) = \Big[- Acos^2(\omega_{vib}t) + B\Big] exp\Big(- \frac{t}{\tau_{rel}}\Big)$$

[1] τ_{c-th}: is the charge thermalization time.
[2] τ_{c-rel}: is the charge relaxation time.

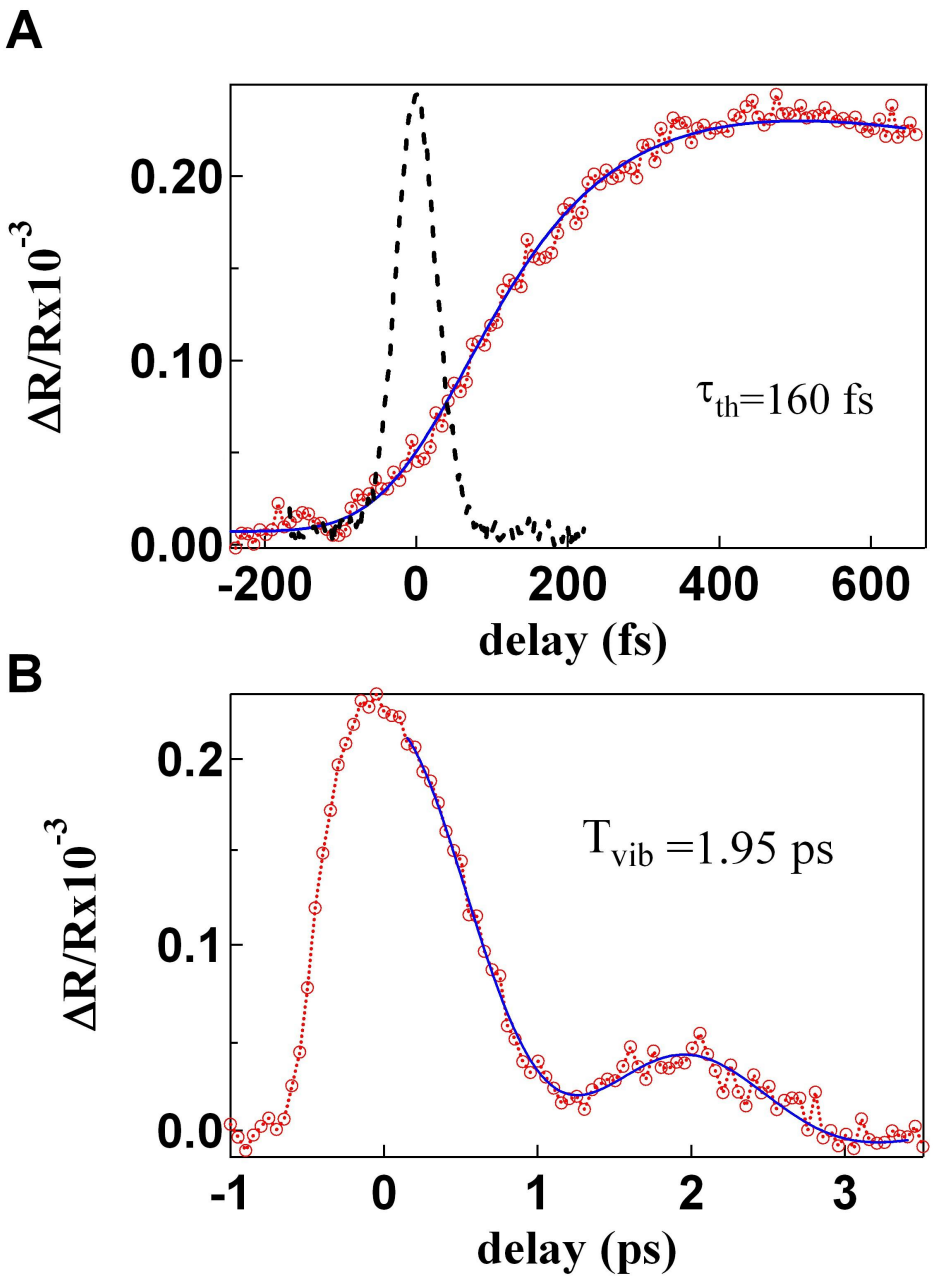

Figure 5.1: Time resolved differential reflectivity (ΔR/R)(t) of non−annealed CoPt core−shell nanoparticles. A) Thermalization dynamics of electrons (blue: fit with causal exponential growth using laser pulse autocorrelation in dashed black line). B) Vibration dynamics of nanoparticles.

Figure 5.2 shows a oscillatory behavior of the nanoparticles occurring on longer a time scale. It is attributed to collective oscillations of the nanoparticles which are organized locally. It is also fitted with a damped cosine function of the form:

$$\left(\frac{\Delta R}{R}\right)(t) = \Big[- Acos^2(\omega_{coll}t) + B\Big] exp\Big(- \frac{t}{\tau_{coll}}\Big) + Cexp\Big(- \frac{t}{\tau_{diff}}\Big)$$

It is characterized with a period T_{coll}=146 $\pm$ 2 ps corresponding to a frequency ν_{coll}=$\omega/2\pi$=6.85 GHz. The oscillations are rapidly damped with a characteristic time τ_{coll}=157 $\pm$ 2 ps. These low frequency oscillations corresponds to a local supracrystalline ordering induced by a mild laser annealing. The supracrystalline ordering corresponds to a coherent vibration of organized nanoparticles recently observed on 3D Co supracrystals (Lisiecki et al. [2008]). We also note that the heat diffusion to the environment on $\tau_{diff} = 170 \pm 2$ ps.

Let us remark that the overall positive signal may be referred to the particularity of the interband optical processes in cobalt platinum with some typical signatures of the electron dynamics in metallic nanoparticles (Bigot et al. [2000]).

In summary, we have shown that the femtosecond laser pulses induce a mild laser annealing of the pellet sample which leads to a local supracrystalline ordering. The assembly of nanoparticles can then oscillate with a 146 ps period which is different than the oscillations with 1.95 ps period associated with the breathing mode of the individual nanoparticles.

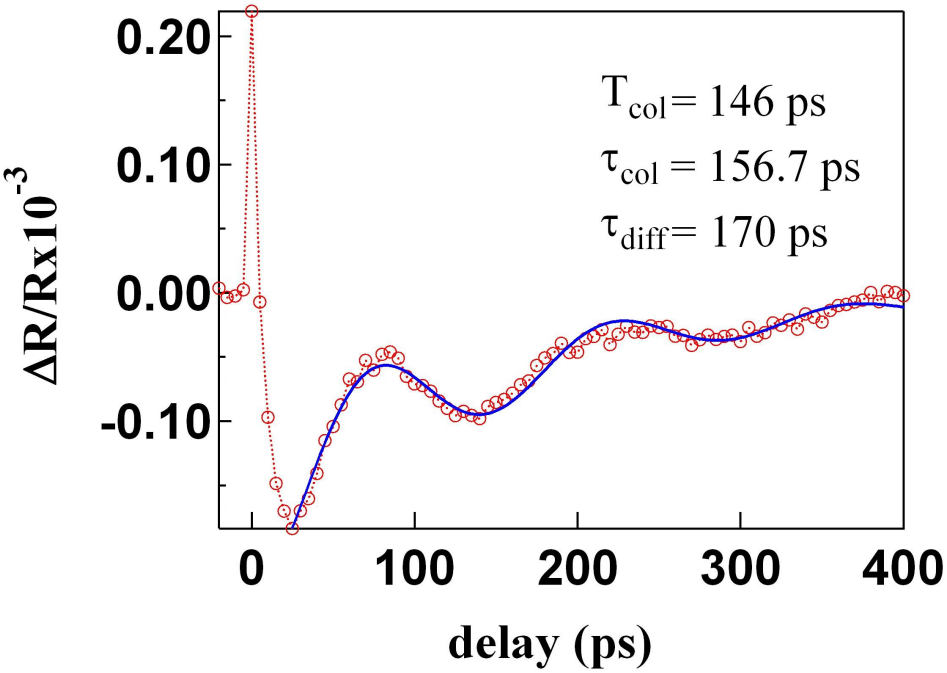

Figure 5.2: Time resolved differential reflectivity (ΔR/R)(t) of non−annealed CoPt core−shell nanoparticles: Collective oscillations of nanoparticles due to laser induced supra-crystal ordering (blue: fit of damped oscillations).

5.1.2 Spin Dynamics

The overall magnetization dynamics occurs during the thermalization of the electrons (Guidoni et al. [2002]). It is followed by a partial re−magnetization. The spin population thermalizes faster than the charge population with a characteristic time τ_{s-th}=101 ± 5 fs[1] for Ep=0.85 mJ/cm^2. This faster thermalization may be attributed to the important spin scattering processes at the core/shell interface.

Due to the efficient breathing mode relaxation process of the charges, the spin relaxation process is also found to be faster with τ_{s-rel}=363 ± 5 fs[2] for a pump energy Ep=0.85 mJ/cm^2.

[1] τ_{s-th}: is the spin thermalization time.
[2] τ_{s-rel}: is the spin relaxation time.

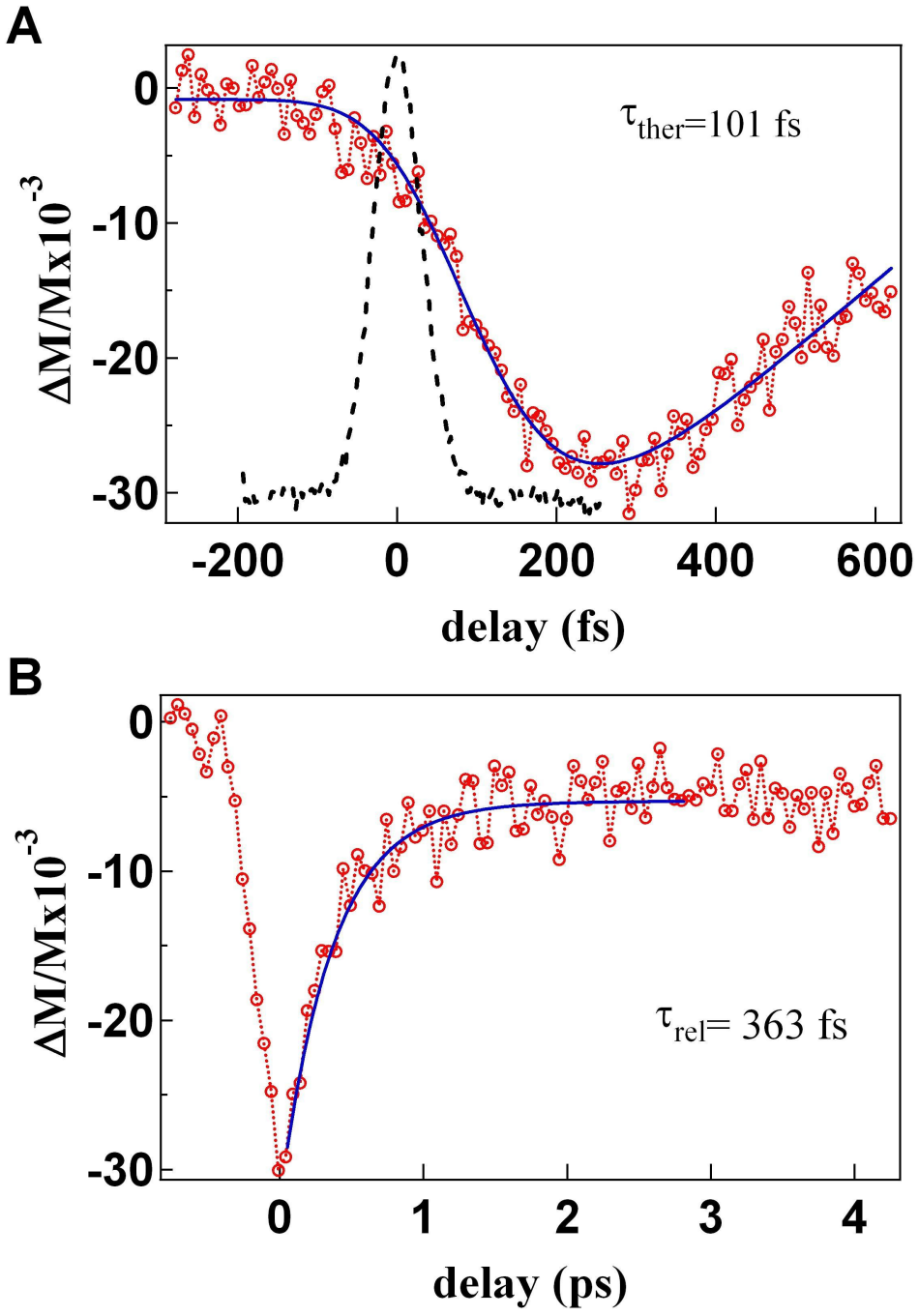

Figure 5.3: Time resolved differential magnetization (ΔM/M)(t) of non−annealed CoPt core−shell nanoparticles. A) Thermalization dynamics of the magnetic moments (spins) (blue: fit with causal exponential growth using laser pulse autocorrelation in dashed black line). B) relaxation dynamics of the magnetic moments (spins) (fit with exponential growth).

On the long time scale, no remarkable features can be observed. This indicates that the moments of the particles precesses randomly which is in agreement with their superparamagnetic nature.

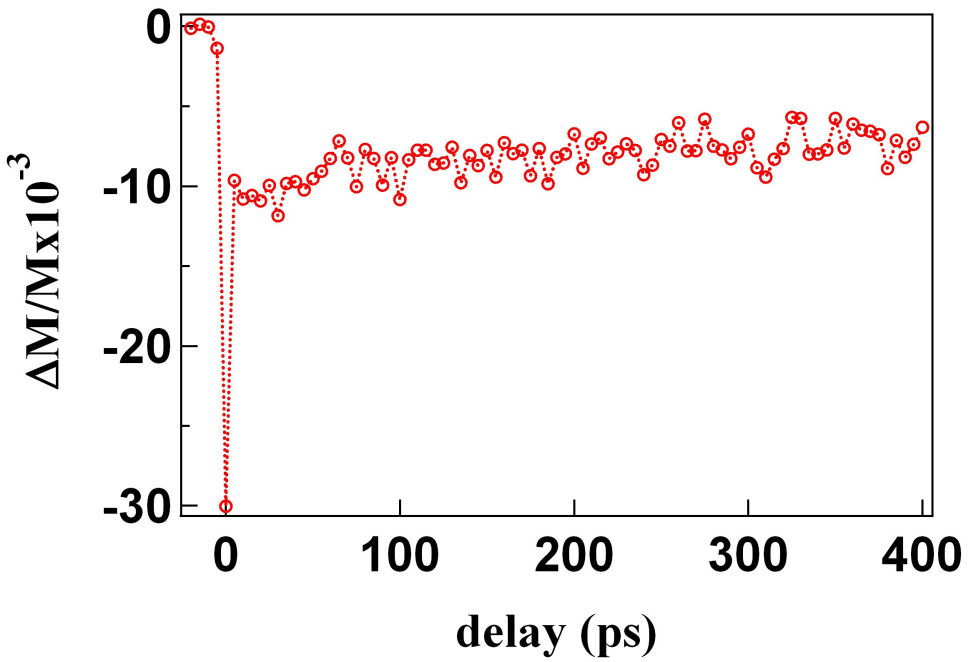

Figure 5.4: Time resolved differential magnetization ΔM/M(t) of non−annealed CoPt core−shell nanoparticles: classical heat diffusion process.

In conclusion, in comparison with the charges, we have reported a faster spin thermalization process attributed to the important scattering processes occurring at the core/shell interface. Also, a faster spin relaxation process is reported. The lattice heat diffusion process is observed to be monotonic.

5.2 Annealed Samples

As we have discussed in the previous chapter, the thermal annealing to 650 K induced a magnetic phase transition from superparamagnetic to ferromagnetic at room temperature ($T_B > 350K$). Moreover, it has induced a CoPt crystalline phase. The existence of this phase was confirmed by a temperature dependent mi-

croscopy imaging carried on a single nanoparticle shown in chapter 4 section 4.5.3. The ferromagnetism manifest itself as an increase in the magnetic anisotropy energy which in turn increases the energy barrier KV and consequently prevents the thermal fluctuation of the magnetization.

5.2.1 Charge Dynamics

The annealed pellets follow the same charge dynamics as the non−annealed pellets that is a thermalization, relaxation and heat diffusion processes. The thermalization process is found to be faster where τ_{c-th}=115 ± 5 fs for Ep=0.45 mJ/cm^2 and τ_{c-th}=172 ± 5 fs for Ep=1.6 mJ/cm^2.
As it is mentioned before, the thermal annealing induced important changes in the morphology of the nanoparticles. It has induced an inhomogeneity at the core−shell interface due to the platinum diffusion inside the cores of the nanoparticles and/or to the intersticial platinum diffusion between the nanoparticles which leads to the reduction of the mean free path of the electrons. This reduction increases the scattering cross−section of the electrons which lead to the faster thermalization (Link and El Sayed [1999]; Voisin et al. [2000]).
The electron phonon relaxation time is τ_{c-rel}=1.52 ± 0.04 ps for a pump energy Ep=0.85 mJ/cm^2. The annealed nanoparticles kept the breathing mode vibrations during their relaxation, however, with an increased period T_{vib}=2.5 ± 0.1 ps. In fact, this can also be attributed to the diffusion of the platinum inside the Co core.

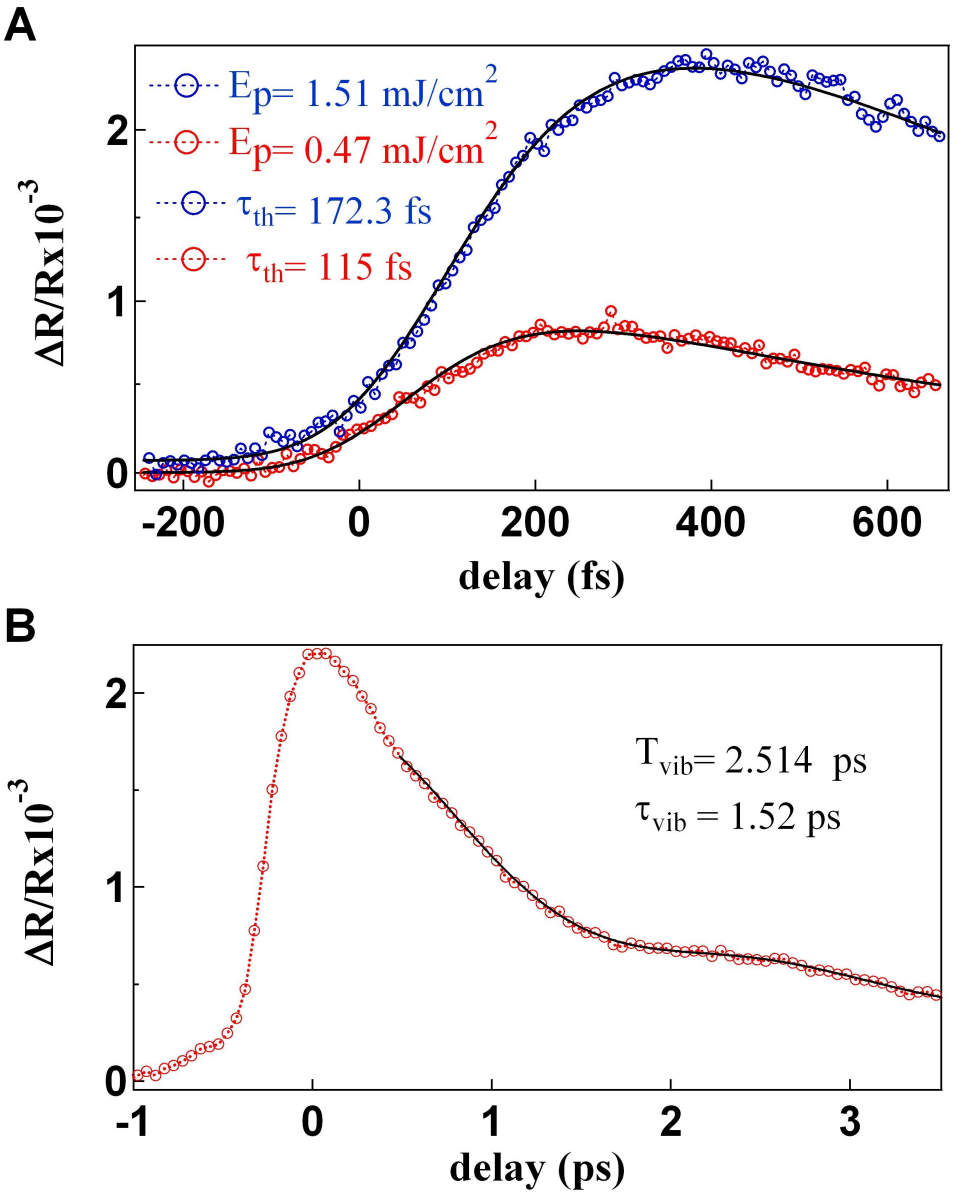

Figure 5.5: Time resolved differential reflectivity (ΔR/R)(t) of annealed CoPt core−shell nanoparticles. A) Thermalization dynamics of electrons (blue: fit with causal exponential growth using laser pulse autocorrelation in dashed black line). B) Vibration dynamics of nanoparticles.

The disappearance of the collective oscillations is another consequence of the thermal annealing. We notice that the relaxation to the environment is slower in

comparison with the non−annealed pellets. The process now takes place on two steps corresponding to two time scales:

1. Thermal diffusion between the nanoparticles with a time constant $\tau_{diff,1}$=138 ± 2 ps.

2. Overall thermal diffusion outside the spatial region probed by the laser beam with a $\tau_{diff,2}$=980 ± 25 ps.

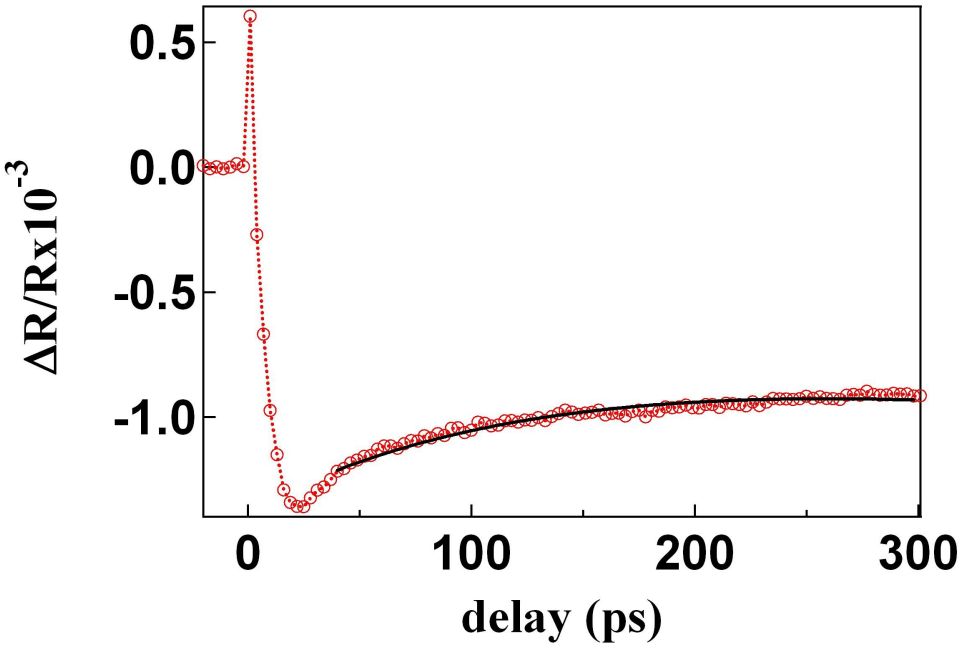

Figure 5.6: Time resolved differential reflectivity (ΔR/R)(t) of annealed CoPt core−shell nanoparticles: Thermal diffusion.

This longer thermal diffusion process is attributed to the low thermal conductivity of the pellets. The situation is different for nanoparticles dispersed in matrices which serves as efficient heat reservoirs with a considerable thermal conductivity that plays a significant role during the cooling process e.g Ag nanoparticles embedded in AL_2O_3 or SiO_2 (Halté et al. [1999]).
In conclusion, by thermally annealing the samples, the pellets cannot be anymore ordered into supracrystals. In contrast, individual nanoparticles kept their

breathing mode relaxation process. We remark an important electron scattering processes leading to a faster thermalization of the electrons.

5.2.2 Spin Dynamics

The annealed samples show typical overall magnetization dynamics that is a demagnetization process followed by a partial re−magnetization. In comparison with the non−annealed samples, the thermalization and relaxation processes are observed to be slower. We obtained the following spin thermalization times : τ_{s-th}=109 ± 5 fs for a pump energy Ep=0.471 mJ/cm^2 or τ_{s-th}=154 ± 5 fs for Ep=1.51 mJ/cm^2, and spin relaxation times: τ_{s-rel}=495 ± 5 fs for Ep=1 mJ/cm^2.

The slower thermalization and relaxation processes are attributed to the ferromagnetic nature of the annealed particles induced by the diffusion of the platinum inside the cobalt core which led to the formation of a CoPt crystalline phase. Similar thermalization and relaxation times have been reported on CoPt films by Guidoni et al. [2002].

Actually, the induced CoPt phase has two effects on the magnetic properties of the pellets. First, an increase in the value of magnetization at saturation as can be seen from the 300 K ferromagnetic hysteresis loop plotted on figure 4.20. Second, the ferromagnetic nanoparticles are no more separated by the platinum shell enhancing the magnetic dipole−dipole interactions. This results in a different magnetization for directions // and ⊥ to the sample plane.

As we have discussed in the previous chapter in section 4.5.3, we have estimated the increase in the anisotropy constant to be:

$$K_{1_{core-shell}} \approx 0.38 K_{1_{CoPt}}$$

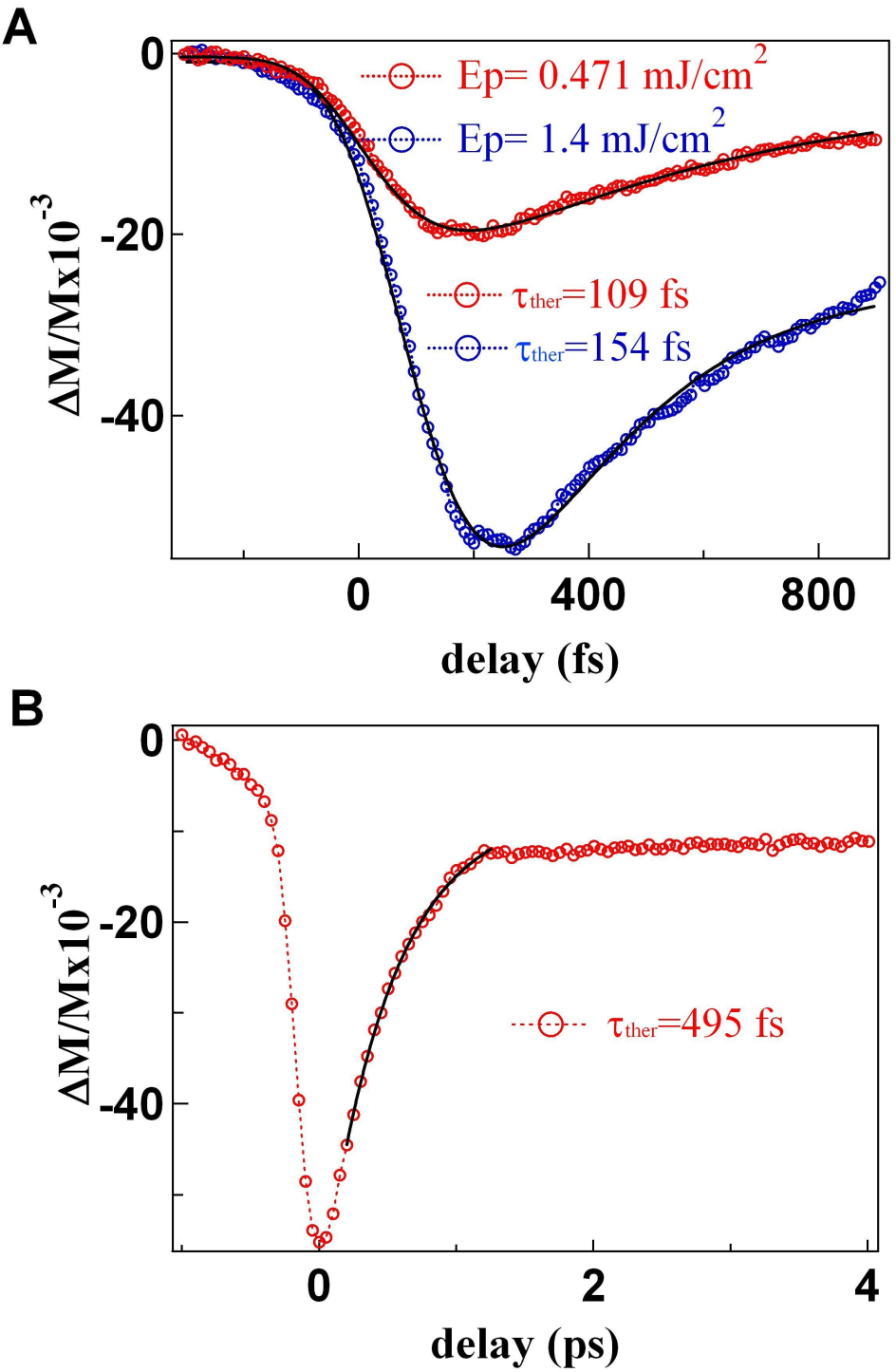

Figure 5.7: Time resolved differential magnetization (ΔM/M)(t) of annealed CoPt core−shell nanoparticles. A) Thermalization dynamics of the magnetic moments (spins) (blue: fit with causal exponential decay using laser pulse autocorrelation in dashed black line). B) relaxation dynamics of the magnetic moments (spins) (fit: exponential growth.

On the contrary to the non−annealed samples, the heat diffusion process induces a precession of the magnetization vector. On figure 5.8, we show an example of this precession with a characteristic period T_{prec}=80 ± 2 ps for Ep=0.382 mJ/cm^2 where the external field $\mathbf{H}_0$=0.2 T is applied at angles 50° and 130°. The ultrafast change in temperature induces a change in both the modulus and orientation of the magnetization vector. Vomir et al. [2005] have shown that the re−orientation of the magnetization vector in cobalt thin films is due to a dynamical change in the effective field.

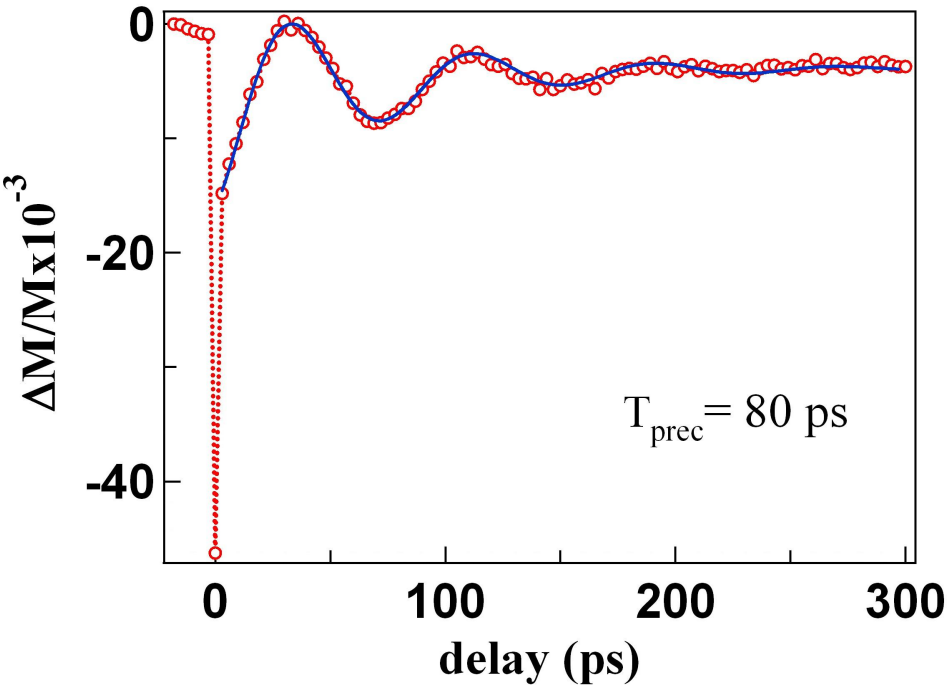

Figure 5.8: Time resolved differential magnetization (ΔM/M)(t) of annealed CoPt core−shell nanoparticles: precession of the magnetization vector.

We fit the precession with a damped cosine function of the form:

$$\left(\frac{\Delta M}{M}\right)(t) = \left[-Acos^2(\omega_{coll}t) + B\right] exp\left(-\frac{t}{\tau_{prec}}\right) + Cexp\left(-\frac{t}{\tau_{diff}}\right)$$

Since both the amplitude and the direction of the effective field depend on the

amplitude and orientation of the applied field, then it is expected that the variations of these parameters will affect the magnetization precession period. In what follows we present a study of the effects of amplitude as well as orientation variation on the precession in the pellets.

5.2.2.1 Variation with the Amplitude and Orientation

Figure 5.9, shows different precessions of the magnetization vector for different amplitudes of the applied field.

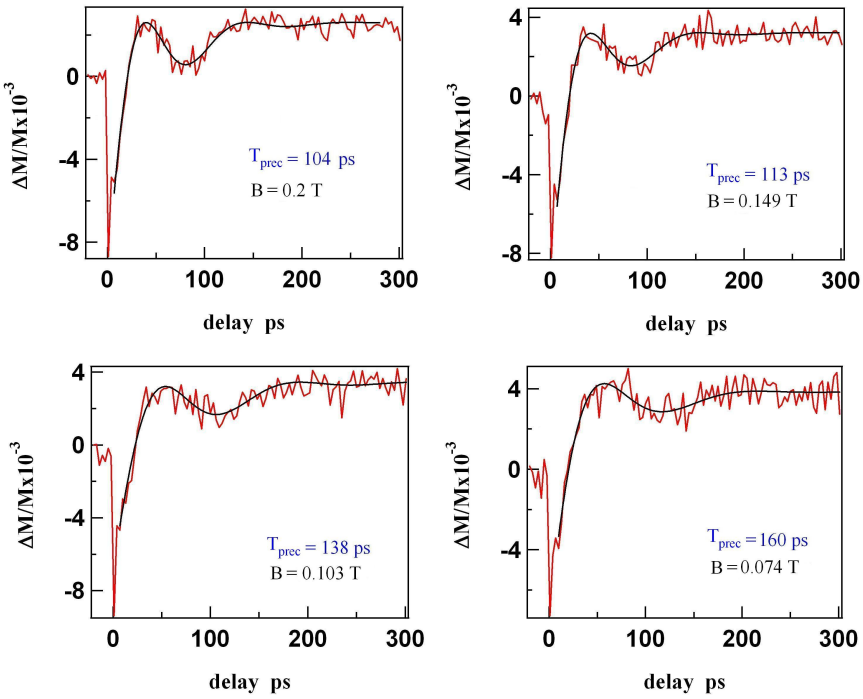

Figure 5.9: Precession of the magnetization vector for different intensities of the field (direction of H: 50,130).

The amplitude of the field varies between 0.2 and 0.074 T, we found that the period of precession decreases (T_{prec}=160 ps for H_0=0.074) as the amplitude of the applied field increases (T_{prec}=104 ps for H_0=0.2). The obtained results are consistent with the results reported on NiFe/NiO bilayer (Ju et al. [1999]),

ferromagnetic film and permalloy (Kampen et al. [2002]), GdFeCo structures (Tsukamoto et al. [2004]) or Co/Al_2O_3 thin films (Vomir et al. [2005]).

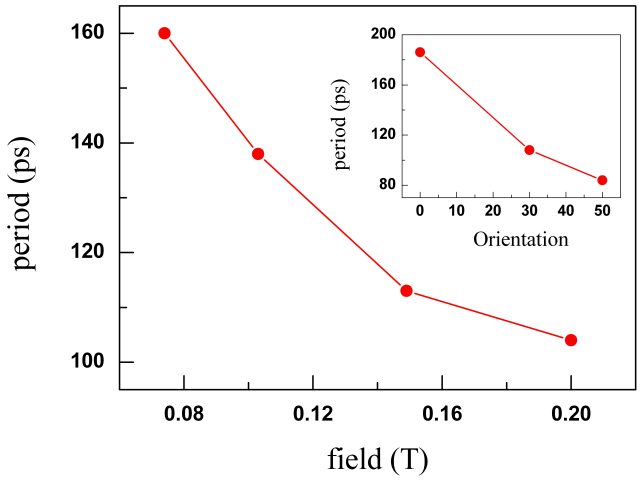

Figure 5.10: Variation of the period vs the intensity of the applied field. Inset: variation with orientation.

The laser excitation perturbs the direction of the effective field $\overrightarrow{H}_{eff}(t) = \overrightarrow{H}_{ani}(t) + \overrightarrow{H}_0$, where $\overrightarrow{H}_{ani}(t)$ represents the magnetic fields due to the shape and the magneto−crystalline anisotropy and $\overrightarrow{H}_0$ represents the external applied field. This will lead to modifications of both the magnitude and the direction of the magnetization vector. The change in the period of precession is related to the modifications of the time dependent magneto−crystalline anisotropy (Bigot et al. [2005]).
As discussed in chapter 3 (section 3.3.0.3), we model the ultrafast magnetization vector precession following the model proposed by Bigot et al. [2005].

$$\frac{d\overrightarrow{M}}{dt} = \gamma\left(\overrightarrow{M} \wedge \overrightarrow{H}_{eff}\right) - \left[\frac{d\overrightarrow{M}}{dt}\right]_{relax} - P(t)\overrightarrow{M}(t) \tag{5.1}$$

where the second term of the right part of equation 5.1 corresponds to the damping.

5.3 Comparison

We stress that thermal annealing of the samples induced important changes in the magnetic properties of the samples. The dynamical measurements are consistent with the static measurements, and they confirm the ferromagnetic nature of the annealed samples. The magnetization precession is an important characteristic of the nanoparticles that has appeared after annealing.
Concerning the charge dynamics, we notice that the diffusion of the platinum into the cobalt core accelerated the thermalization process. The thermal annealing ceased the possibility to order the pellets into supracrystals using the femtosecond laser pulses. We present two tables including the different characteristic relaxation times of the non −annealed and annealed samples.

	$\tau_{c\text{-}th}$ [fs]	$\tau_{c\text{-}rel}$ [ps]	T_{vib} [ps]	T_{coll} [ps]	τ_{coll} [ps]	τ_{diff} [ps]
CoPt core-shell (non-annealed)	160 ±5 (E_p = 0.8 mJcm^{-2})	1.34 ± 0.03 (E_p = 0.8 mJcm^{-2})	1.95 ± 0.1	146±2	156 ±2	170 ±2
CoPt core-shell(annealed 650 K)	115 ±5 (E_p = 0.4 mJcm^{-2}) 172 ±5 (E_p = 1.5 mJcm^{-2})	1.84± 0.04 (E_p = 0.8 mJcm^{-2})	2.15 ±0.1	None	None	138 ±2 & 980 ±50

Figure 5.11: Characteristic electron and vibrational relaxation times in CoPt core-shell nanoparticles. τ_{c-th}: thermalization of electrons, τ_{c-rel}: relaxation of electrons, T_{vib}: breathing vibration period of individual nanoparticles, T_{coll}: collective oscillations associated to the supra-crystal ordering of nanoparticles, τ_{coll}: damping of collective oscillations, τ_{diff}: energy dissipation to the environment. Ep is the absorbed density energy of excitation.

	$\tau_{s\text{-}th}$ [fs]	$\tau_{s\text{-}rel}$ [fs]
CoPt core-shell (non-annealed)	101 ±5 (E_p = 0.8 mJcm^{-2})	363 ± 5 (E_p = 0.8 mJcm^{-2})
CoPt core-shell(annealed 650 K)	109 ±5 (E_p = 0.4 mJcm^{-2}) 154 ±5 (E_p = 1.5 mJcm^{-2})	495 ± 5 (E_p = 1 mJcm^{-2})

Figure 5.12: Characteristic spin relaxation times in CoPt core-shell nanoparticles. τ_{s-th}: thermalization of spins, τ_{s-rel}: relaxation of spins. Ep is the absorbed density energy of excitation.

Chapter 6

Modeling the Magnetization Dynamics in Nanoparticles

In the domain of magnetic nanomaterials, the numerical simulation is an effective tool capable of providing better understanding of different physical phenomena since it is only in few cases reliable experimental investigations are possible. For instance, magnetization reversal (e.g. Scholz et al. [2004]), magnetic phase transition (e.g. Lopez-Diaz et al. [2002]), magnetization dynamics (e.g. Atxitia et al. [2007]; Chubykalo et al. [2003]; Tsiantos et al. [2007]), effect of dipolar interactions on the nanoparticles (e.g. Denisov et al. [2004]; Plumer et al. [2010])...etc. As modern nanotechnology aims to use smaller monodomain magnetic nanoparticles in the data storage, the understanding of magnetization reversal in these particles becomes critical. Since the leading theoretical models of Stoner-Wohlfarth (Stoner and Wohlfarth [1948]) and Néel-Brown (Brown [1963]; Néel [1949]), on the magnetization reversal by thermal activation in isolated single domain nanoparticles, intensive experimental and theoretical work has been carried out. For example, by performing switching field and waiting time measurement on small well fabricated isolated monodomain nanoparticles with uniaxial anisotropy energy, Wernsdorfer et al(Wernsdorfer et al. [1997]) showed that the measured relaxation times fit very well with Arrhenius law given by Néel-Brown Model. On the other hand, performing numerical simulations, Coffey et al.(Coffey et al. [1998]) did not only verify Brown's calculations for axially symmetric uniaxial particles but

also were able to find an exact solution of Brown's differential equation for any arbitrary applied field direction.
However, as long as magnetic interparticle interactions, such as dipole-dipole, exchange interaction, are considered the viability of Néel-Brown model becomes questionable. Indeed, in dense samples where the magnetic moments are strongly coupled, the effect of interparticle interactions especially dipole-dipole interaction cannot be neglected. Recently, in many articles it is shown that these interparticles interactions may lead to a collective behavior such as Super-Spin Glass behavior (SSG) (Djurberg et al. [1997]; Mamiya et al. [1999]) or Super-Ferromagnetism (SFM) (Mørup et al. [1983]; Rancourt and Daniels [1984]).
Therefore, due to the importance of understanding the effects of different interactions on the magnetization reversal process such as interparticle dipolar interactions, and due to our experimental observation on the magnetization dynamics of super-paramagnetic nanoparticles, this part of the work is devoted to solve Brown's FP equation numerically first for isolated nanoparticles and then for interacting assemblies of these nanoparticles.

6.1 Different Numerical Approaches

6.1.1 Langevin Dynamics Approach

The Langevin Dynamics LD approach was introduced by A. Lyberatos et al. in 1993 (Lyberatos et al. [2010]). It is considered to be the pearl of the numerical simulations due to the close correspondence between the results and real experiments. The approach consists on the direct numerical integration of the Landau Lifshtiz Gilbert (LLG) equation derived by Brown (Brown [1963]). The LLG models the time evolution as well as the precessional motion of magnetization vector in the magnetic nanoparticle.

$$\frac{\partial \overrightarrow{M}}{\partial t} = -\frac{\mu_0 \gamma_0}{M_s(1+\alpha^2)} \overrightarrow{M} \times [(\overrightarrow{H} + \overrightarrow{h(t)}) + \alpha \overrightarrow{M} \times (\overrightarrow{H} + \overrightarrow{h(t)})] \tag{6.1}$$

where

- γ : gyromagnetic coefficient.

- α : damping constant.
- M_s : saturation magnetization.
- $\overrightarrow{h(t)}$: thermal or random field.
- $$\overrightarrow{H} = -\frac{1}{M_s V}\frac{\partial E}{\partial \overrightarrow{M}}$$

Different discretization schemes of the above equation may provide results that match with one of the two interpretations of the random field discussed in the first chapter 2.5.2.1: the Itô′s interpretation e.g.Euler method (Greiner et al. [1988]), and the Stratonovich′s interpretation e.g. Heun method (García-Palacios and Lázaro [1998]; Wolf [1997]). Therefore, to be consistent with Brown calculations, a Heun−like method should be used. The Heun's method is a predictor−corrector method where the predictor is the forward Euler's method and the corrector is a trapezoidal method.
Despite of the firm physical basis, the LD approach cannot be used to model the dynamics on long time scales and it is limited to short time scales because the numerical accuracy to model the spin precession forces very small discretization step and so a LD simulation on a long time scale will be time and memory consuming.

6.1.2 Monte Carlo Approach

The Monte Carlo MC numerical method was introduced a long time ago by Metropolis N. and Ulam S. in 1949 (Metropolis and Ulam [1949]). The application of MC to Micromagnetism is very useful especially as it allows to probe the magnetization dynamics on long time scales i.e. on time scales where the LD approach cannot be applied. The approach consists on the calculation of the trajectories in phase space $(\overrightarrow{r},\overrightarrow{v})$ following a master equation which stands for the development of the probability distribution $P_s(t)$ in phase space (Nowak [2001]):

$$\frac{dP_s}{dt} = \sum_{s'}(P_{s'}\omega_{s'\to s} - P_s\omega_{s\to s'}) \tag{6.2}$$

Here s and $s^{'}$denote different states of the system and ω is the transition rate from one state to another.
Within MC method, we may distinguish between two basic algorithms: the spin flip algorithm (Glauber [1963]) and the cluster algorithm (Swendsen and Wang [1987]; Wolff [1989]).
The basic drawback in MC methods is that the time corresponds to the number of MC steps and there is no clear connection to the real time i.e. physical time scale at which the process takes place. However, the first serious attempt to overcome this problem was introduced by Nowak et al. (Nowak et al. [2000]) where they proposed a MC method with time quantified step. The basic assumptions of the new method are:

1. The magnetic moments are uncorrelated.

2. The quantification is valid on time scales larger than those of the relaxation and precession processes.

6.1.3 Fokker Planck Approach

In our study, we follow a third computational method that is equivalent to the LD approach and it is based on the numerical integration of the Fokker Planck (FP) equation derived by Brown (Brown [1963]). The FP equation governs the non-equilibrium probability distribution W of magnetic moment orientation associated with the stochastic LLG equation. Knowing that E is the total energy, then the FP eqution is:

$$\begin{aligned}\frac{\partial W}{\partial t} &= \frac{1}{\sin\theta}\frac{\partial}{\partial\theta}\Big(\sin\theta\Big[\Big(h'\frac{\partial E}{\partial\theta}-g'\frac{1}{\sin\theta}\frac{\partial E}{\partial\phi}\Big)W+k'\frac{\partial W}{\partial\theta}\Big]\Big)\\ &+ \frac{1}{\sin\theta}\frac{\partial}{\partial\phi}\Big[\Big(g'\frac{\partial E}{\partial\theta}+h'\frac{1}{\sin\theta}\frac{\partial E}{\partial\phi}\Big)W+k'\frac{1}{sin\theta}\frac{\partial W}{\partial\phi}\Big].\end{aligned}$$

In our work, we want to study the magnetization reversal processes in superparamagnetic nanoparticles where the thermal fluctuations causes the reorientation of the magnetization from one equilibrium to another. We have decided to use the Fokker Planck approach for two reasons: first the fluctuations are already taken

into account by the Fokker Planck equation derived by Brown, so we do not need to model these fluctuations. Second, adapting either of the Langevin dynamics and the Time Quantified Monte Carlo method described in the preceding paragraphs to the case of interacting nanoparticles would require prohibitive computational times and memory storage, particularly when the number of nanoparticles is large.

6.2 Numerical Method

6.2.1 Finite Difference Method

The numerical method used is the Finite Difference (FD) method. The FD method is a very simple and effective method. As in any method of numerical solution, the starting point of FD is to decompose the geometric domain into a set of points or nodes forming a numerical grid. Each node of the grid is identified by its corresponding indices e.g. (i) for 1D, (i, j) for 2D and so on (see figure 6.1).

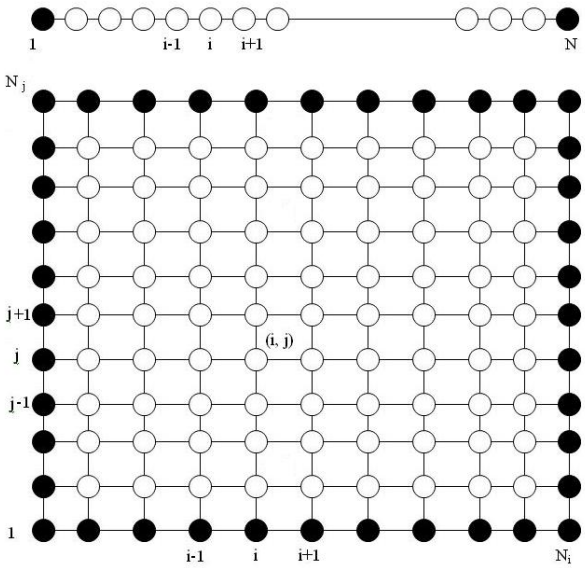

Figure 6.1: 1D and 2D grids.

The main idea in the calculus of FD is to replace the derivatives with linear combinations of discrete values of the function at each grid point so that there will be one algebraic equation to be solved at each grid point (Ferziger and Peric [1996]). At the boundary points, there are two types of boundary conditions:

- **Dirichlet conditions**: if the value of the function is known then no equation is needed.
- **Neumann conditions**: if the value of the function is not known then, the boundary conditions should be discretized to provide the required equation.

6.2.1.1 Approximation of the First Derivative

By definition, the exact derivative of $\phi(x)$ (equation 6.3) at a given point x_i is the slope of the tangent to the curve representing $\phi(x)$ at that point.

$$\left(\frac{\partial \phi}{\partial x}\right)_i = lim_{\Delta x \to 0} \frac{\phi(x + \Delta x) - \phi(x))}{\Delta x} \tag{6.3}$$

In FD method, the first derivative can be approximated in three possible ways:

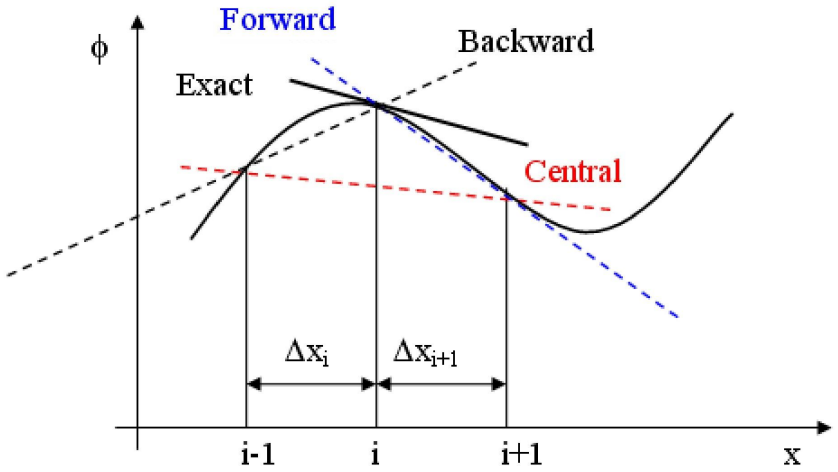

Figure 6.2: On the definition of a derivative and its approximation.

- Backward Difference Scheme (BDS): the slope is approximated by the slope of the line passing by x_i and a point before.(Dashed black line)

$$\Big(\frac{\partial\phi}{\partial x}\Big)_i \approx \frac{\phi_i - \phi_{i-1}}{x_i - x_{i-1}} \quad with \quad \Delta x_i = x_i - x_{i-1}. \tag{6.4}$$

- Forward Difference Scheme (FDS): the slope is approximated by the slope of the line passing by x_i and a point after.(Dashed blue line)

$$\Big(\frac{\partial\phi}{\partial x}\Big)_i \approx \frac{\phi_{i+1} - \phi_i}{x_{i+1} - x_i} \quad with \quad \Delta x_{i+1} = x_{i+1} - x_i. \tag{6.5}$$

- Central Difference Scheme (CDS): the slope is approximated by the slope of the line passing by two points before and after x_i.(Dashed red line)

$$\Big(\frac{\partial\phi}{\partial x}\Big)_i \approx \frac{\phi_{i+1} - \phi_{i-1}}{x_{i+1} - x_{i-1}} \tag{6.6}$$

For FDS and BDS, the truncation error is:

$$\epsilon_r \approx \frac{\Delta x_i}{2}\Big(\frac{\partial^2\phi}{\partial x^2}\Big)_i \tag{6.7}$$

While for the CDS, the truncation error is:

$$\epsilon_r \approx \frac{(1 - r_e)\Delta x_i}{2}\Big(\frac{\partial^2\phi}{\partial x^2}\Big)_i \quad with \quad r_e = \frac{\Delta x_{i+1}}{\Delta x_i} \tag{6.8}$$

6.2.1.2 Approximation of the Second Derivative

By definition, the second derivative of $\phi(x)$ is the slope of the tangent to the curve representing the first derivative. It is can be also approximated following one of the three schemes mentioned above.

$$\Big(\frac{\partial^2\phi}{\partial x^2}\Big)_i = \frac{\phi_{i+1}(x_i - x_{i-1}) + \phi_{i-1}(x_{i+1} - x_i) - \phi_i(x_{i+1} - x_{i-1})}{(x_{i+1} - x_i)^2(x_i - x_{i-1})} \tag{6.9}$$

with the the truncation error being:

$$\epsilon_r \approx \frac{\Delta x_{i+1} - \Delta x_i}{3} \left(\frac{\partial^3 \phi}{\partial x^3}\right)_i \tag{6.10}$$

For example, for CDS where $\Delta x_{i+1} = \Delta x_i$ the approximation becomes:

$$\left(\frac{\partial^2 \phi}{\partial x^2}\right)_i = \frac{\phi_{i+1} + \phi_{i-1} - 2\phi_i}{\Delta x^2} \tag{6.11}$$

6.2.1.3 Approximation of the Mixed Derivative

A mixed Derivative is approximated as follows:

$$\frac{\partial^2 \phi}{\partial x \partial y} = \frac{\phi_{i+1,j+1} - \phi_{i+1,j-1} - \phi_{i-1,j+1} + \phi_{i-1,j-1}}{4\Delta x \Delta y} \tag{6.12}$$

6.3 Isolated Nanoparticles

The relaxation time describes how fast does a magnetization reversal between two energy minima separated by an anisotropy barrier takes place.
As a starting point, we calculate the relaxation times of single domain ferromagnetic nanoparticles with uniaxial anisotropy (ϕ is constant). For that, we solve numerically the Brown's Fokker Planck equation for these particles (Brown [1963]):

$$\frac{\partial W}{\partial t} = \frac{1}{\sin\theta} \frac{\partial}{\partial \theta} \left(\sin\theta \left[h' \frac{\partial E}{\partial \theta} W + k' \frac{\partial W}{\partial \theta} \right] \right) \tag{6.13}$$

with the total energy:

$$E(\theta) = KV \sin^2\theta - \mu_0 V M_s \cos\theta \tag{6.14}$$

6.3.1 Discretization Scheme

In order to discretize the above equation, we perform following two changes of variables:

- x=$cos\theta$ then the FP eqution and the energy become:

$$\frac{\partial W}{\partial t} = \frac{\partial}{\partial x}\Big((1-x^2)\Big[h'\frac{\partial E}{\partial x}W + k'\frac{\partial W}{\partial x}\Big]\Big) \tag{6.15}$$

$$\begin{aligned} E(\theta) &= KV\sin^2(\theta) - \mu_0 VHM\cos(\theta) \\ &= KV(1-x^2) - \mu_0 VHMx \\ &= E(x) \end{aligned}$$

- $t = \widehat{t} * tau$

$$tau = \frac{(1+\alpha^2)VM_s}{\alpha\gamma_0 K_B T} \tag{6.16}$$

Thus, the final dimensionless equation is:

$$\begin{aligned} \frac{\partial W}{\partial \widehat{t}} &= \frac{\partial}{\partial x}\Big[(1-x^2)\Big((Ax+B)W + \frac{\partial W}{\partial x}\Big)\Big] \\ &= \frac{\partial}{\partial x}\Big[(1-x^2)(Ax+B)W\Big] + \frac{\partial}{\partial x}\Big[(1-x^2)\frac{\partial W}{\partial x}\Big] \\ &= \frac{\partial}{\partial x}\Big(U(x)W\Big) + \frac{\partial}{\partial x}\Big(D(x)\frac{\partial W}{\partial x}\Big) \end{aligned}$$

where

- $A = -\frac{2KV}{K_B T}$ and $B = -\frac{\mu_0 VHM}{K_B T}$.
- U(x)=$(1-x^2)(Ax+B)$ and $D(x) = 1-x^2$

The temporal grid contains **n** nodes separated by a temporal step Δt so that $t_i = n * \Delta t$ with $0 \leq \mathbf{i} \leq n$, while the spatial grid contains **s** nodes separated by a spatial step Δx so that $x_j = x_0 + j * \Delta x$ with x_0 the position of initial node and $0 \leq \mathbf{j} \leq s$.

The discretization in time is done following a forward derivative scheme:

$$\frac{\partial W}{\partial \hat{t}} = \frac{W_j^{i+1} - W_j^i}{\Delta t} \tag{6.17}$$

The discretization in space is done following a central derivative scheme:

$$\begin{aligned}
\frac{\partial}{\partial x}\Big(U(x)W\Big) &= \frac{U_{j+1}W^i_{j+1} - U_{j-1}W^i_{j-1}}{2\Delta x} \\
\frac{\partial}{\partial x}\left(D(x)\frac{\partial W}{\partial x}\right) &= \frac{\Big(D(x)W^i\Big)_{j+\frac{1}{2}} - \Big(D(x)W^i\Big)_{j-\frac{1}{2}}}{\Delta x} \\
&= (D_{j+1}+D_j)\Big(\frac{W^i_{j+1}}{2\Delta x^2}\Big) + (D_{j-1}+D_j)\Big(\frac{W^i_{j-1}}{2\Delta x^2}\Big) \\
&- (D_{j+1}+D_{j-1}+2D_j)\Big(\frac{W^i_j}{2\Delta x^2}\Big)
\end{aligned}$$

Finally,we get:

$$\begin{aligned}
W^{i+1}_j &= W^i_j \\
&+ U_{j+1}\Big(\frac{\Delta t}{2\Delta x}\Big)W^i_{j+1} - U_{j-1}\Big(\frac{\Delta t}{2\Delta x}\Big)W^i_{j-1} \\
&+ (D_{j+1}+D_j)\Big(\frac{\Delta t}{2\Delta x^2}\Big)W^i_{j+1} + (D_{j-1}+D_j)\Big(\frac{\Delta t}{2\Delta x^2}\Big)W^i_{j-1} \\
&- (D_{j+1}+D_{j-1}+2D_j)\Big(\frac{\Delta t}{2\Delta x^2}\Big)W^i_j
\end{aligned}$$

6.3.2 Boundary Conditions

The coefficients U and D are variable dependents and vanish at the boundaries. However, their corresponding derivatives do not. This imposed special treatment of the boundary conditions. The method that we have used to calculate the boundary conditions can be found in the Appendix A.

The boundary conditions are:

- at j=0:

$$W^{i+1}_0 = W^i_0 + \frac{1}{2}U_1\frac{\Delta t}{\Delta x}W^i_1 + \frac{1}{2}D_1\frac{\Delta t}{\Delta x^2}(W^i_1 - W^i_0) \tag{6.18}$$

- at j=s:

$$W_s^{i+1} = W_s^i - \frac{1}{2}U_{s-1}\frac{\Delta t}{\Delta x}W_{s-1}^i - \frac{1}{2}D_{s-1}\frac{\Delta t}{\Delta x^2}(W_s^i - W_{s-1}^i) \tag{6.19}$$

6.3.3 Numerical Results

How do we get the relaxation time?

- The initial distribution of the moments is a half-gaussian centered at $x = -1$ ($\theta = \pi$).
- Calculate the integral I=$\int_{-1}^{0} W dx$ or I=$\int_{0}^{1} W dx$ at any time and for different values of the temperature T.
- To extract the numerical relaxation time we fit I with an exponential function of the form

$$f(t) = A_0 exp\Big(-\frac{t}{\hat{t}}\Big) + y_0$$

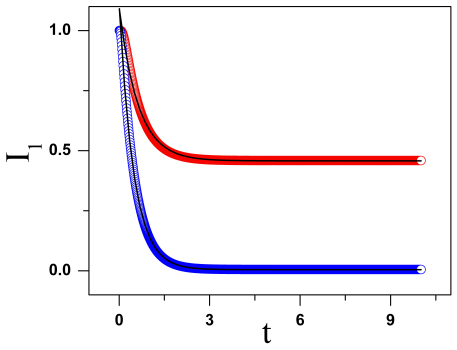

Figure 6.3: A sketch of I_1 fitted with an exponential decay..

- To get the real relaxation time we multiply $\hat{t}$ by tau defined in equation 6.16.

In order to check the consistency of our numerical results, we perform the following tests:

- Verify always that the total number of configurations is conserved that is $\int_{-1}^{1} W dx$=1 at any time.
- Verify that the final configuration of the particles converges to a Boltzmann distribution function which is the equilibrium solution of Brown Fokker Planck equation 6.13.

The numerical code is written in FORTRAN. In what follows, we perform simulations for an isolated Co nanoparticle with the following properties (Nowak et al. [2000]):

- $V = 8 * 10^{-24} m^3$ Total volume of the particle.
- $K = 4.2 * 10^5 J/m^3$ Anisotropy Constant.
- $\mu_s = N\mu_B * 1.7 = 1.12 * 10^{-17} J/T$ Saturation magnetic moment.
- $Ms = \mu_s / V = 1.4 * 10^6 A/m$ Saturation magnetization.
- $\mid H_0 \mid = 0.2/\ \mu_0 A/m$ Intensity of the applied field.

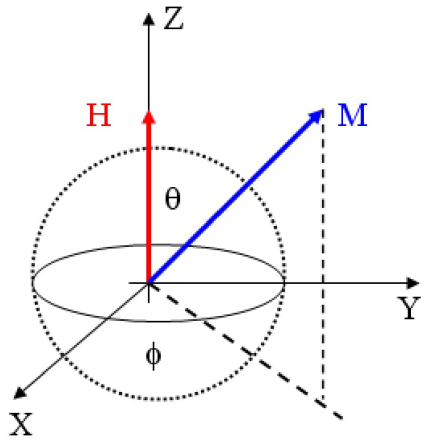

Figure 6.4: A spherical nanoparticle with a magnetic field applied parallel to the easy axis of the particle's magnetization (z−axis).

6.3.3.1 Variation of τ with $1/T$

In this section, we calculate the relaxation time of the particle as a function of temperature. The initial configuration is shown on the figure below:

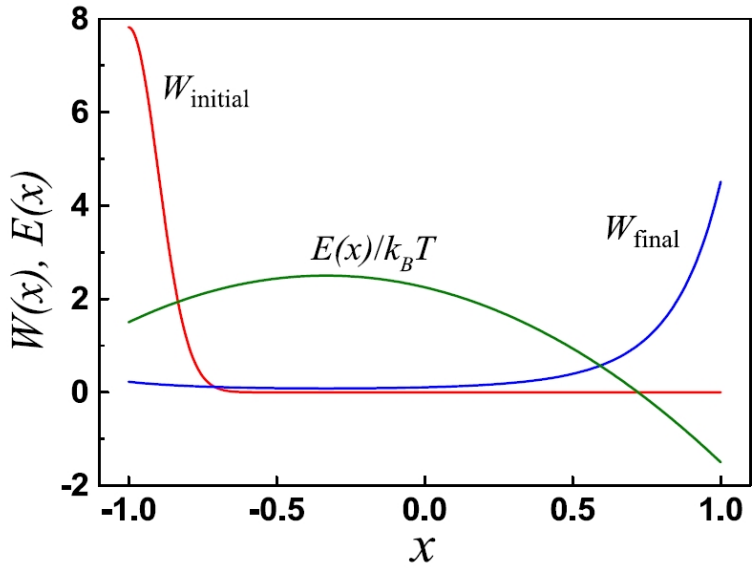

Figure 6.5: The initial distribution (red), the energy profile (green) and final distribution (blue).

In figure 6.6, we compare values of the numerical relaxation times to the exact values obtained directly from Néel-Brown relaxation formula (equation 2.47):

$$\frac{1}{\tau} = \frac{\alpha}{1+\alpha^2}\frac{\gamma_0}{M_s V}\frac{(2KV)^{3/2}}{(2\pi K_B T)^{1/2}}(1-\varepsilon^2)\left[(1+\varepsilon)e^{-\frac{KV}{K_B T}(1+\varepsilon)^2} + (1-\varepsilon)e^{-\frac{KV}{K_B T}(1-\varepsilon)^2}\right] \tag{6.20}$$

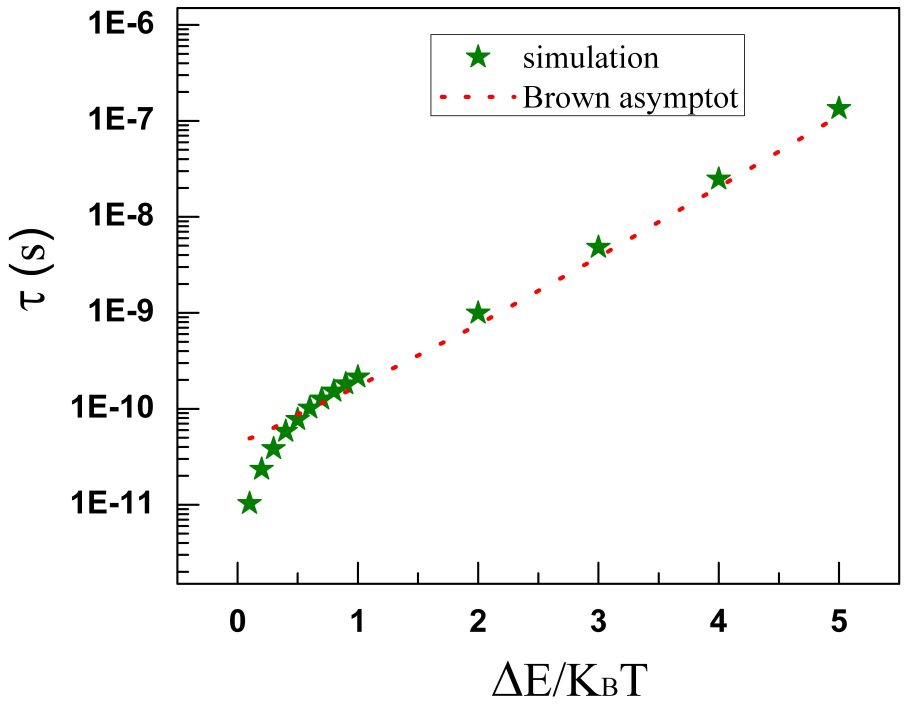

Figure 6.6: The variation of τ as a function of $1/T$ for damping constant α=1.

It is obvious that for low temperatures, the numerical calculations are consistent with those of Brown′s within 10 % accuracy. However, this consistency breaks down for high temperatures and numerically it is expected that τ tends to 0 as T tends to ∞.

To verify the obtained results, we present on figure 6.7 values of the relaxation times obtained by different numerical techniques such as LD and MC (Nowak et al. [2000]).

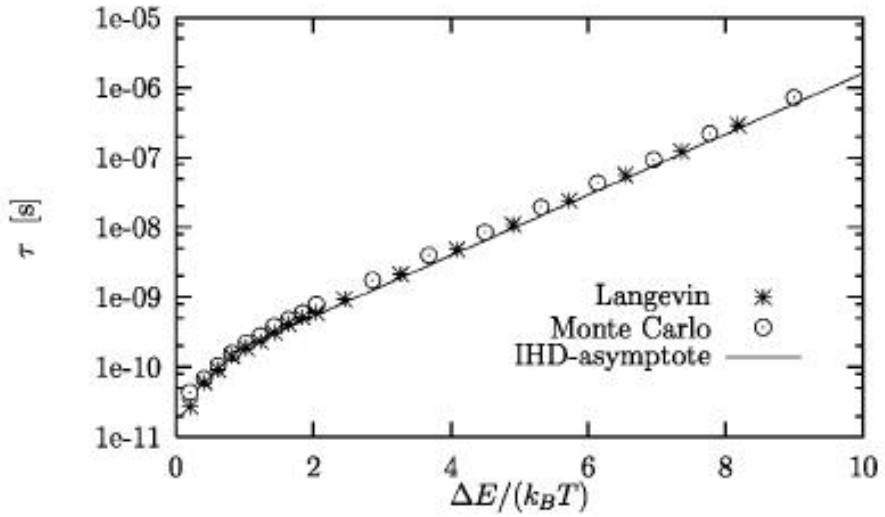

Figure 6.7: The variation of τ as as a function of $1/T$ for damping constant α=1 for three numerical methods: intermediate to high damping, LD simulation, MC simulation.(Nowak et al. [2000])

We clearly see that , the different numerical approaches produce results that show exactly the same behavior i.e. a correspondence at low temperatures and a failure at high temperatures. Moreover, for $\frac{\Delta E}{K_B T}$=2, the numerical methods (LD, MC..) gives $\tau \approx 1$ ns which is exactly found in our simulations.

6.3.3.2 Variation of τ with the Damping Constant α

In this section, we investigate the effect of the damping constant on the relaxation time.

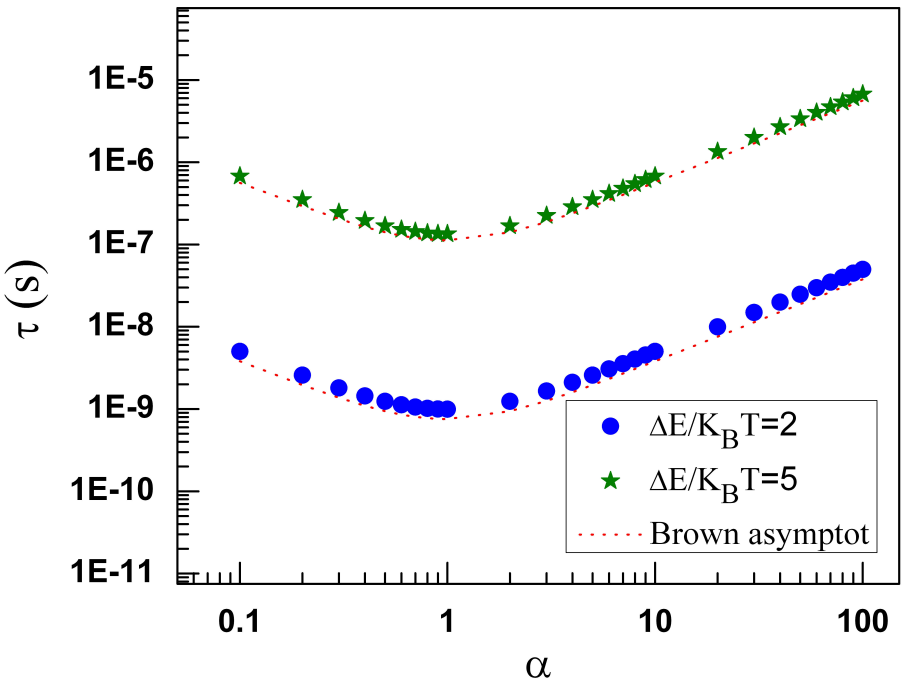

Figure 6.8: The variation of τ as a function of the damping constant α for $\Delta E/K_BT = 2$ (green) and 5 (blue).The red curve corresponds to the analytical brown asymptote.

The results (figure 6.8) show that our method gives a precise description of the reversal process even at low damping limit at the precessional motion dominates the process whereas the MC method proposed by Nowak functions only at the high damping limit.(Chubykalo et al. [2003]; Nowak et al. [2000]).

6.3.3.3 Effect of the angle ψ of the external magnetic applied field

The effect of a constant magnetic field applied with an angle ψ with respect to the easy axis of the magnetization of the particles (see figure 6.9) is studied.

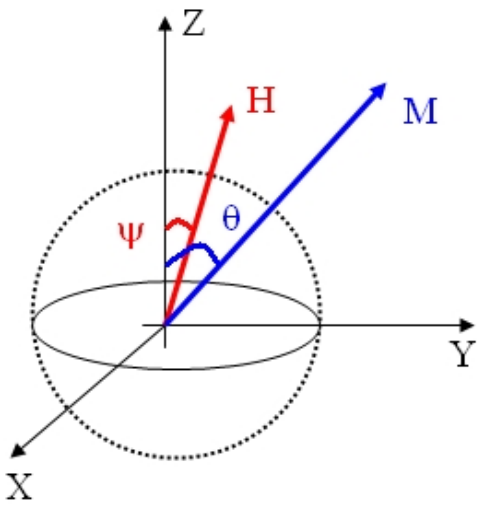

Figure 6.9: A spherical nanoparticle with a magnetic field applied with angle ψ to the easy axis of the particle's magnetization (z−axis).

Energetically, the application of an oblique magnetic field will affect the zeeman contribution of the total energy (equation 6.14) only. The total energy is modified as follows:

$$E(\theta) = KVsin^2\theta - \mu_0 V M_s cos(\theta - \psi) \tag{6.21}$$

In the first chapter paragraph 2.5.2.4, we have introduced an exact calculation of the relaxation time for an oblique magnetic field.
N.B. The applied angle does not affect neither the discretization scheme nor the boundary conditions.
On figure 6.12, we plot the variation of τ as a function of the angle ψ.

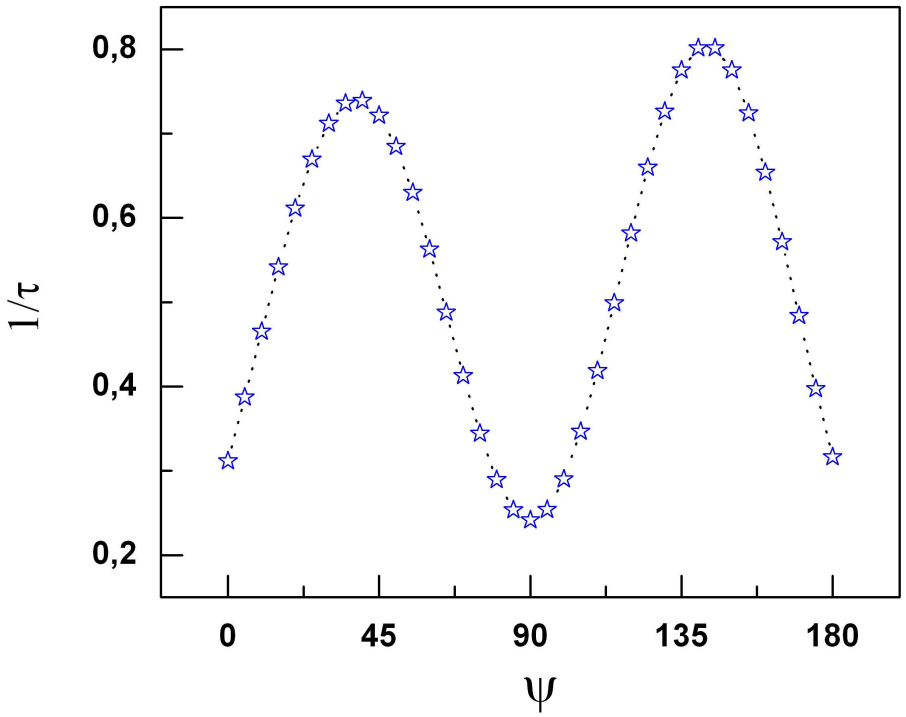

Figure 6.10: The inverse of τ as a function of ψ for damping constant α=1 and $|\mathbf{B}|$=0.2 T (amplitude of the field). τ (ns) is normalized to 0.34.

It is found that the relaxation time is maximum for $\psi = \pi/4$ and minimum for $\psi = \pi/4$. Qualitatively, these results could be interpreted as the manifestation of the height of the energy barrier separating the two energy minima. In fact, the height of the energy barrier for a $\pi/2$ field direction, is maximum with respect to other directions, as can be seen from figure 6.11, making the reversal process the slowest among other field directions. However, for a $\psi = \pi/4$ field direction the height is the lowest making the reversal process the fastest among other field directions. These conclusions are consistent with Brown's calculation.

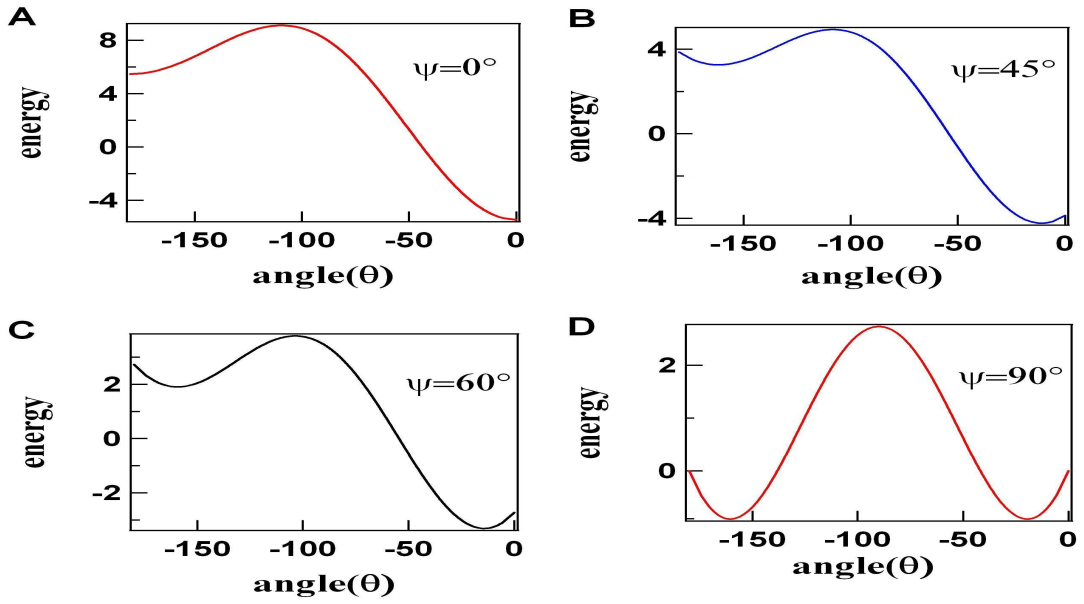

Figure 6.11: Energy Barriers for: A: ψ=0°, B: ψ=45°, C: ψ=60° and D: ψ=90° 90

We do not show exact calculations of the relaxation times, since the analytical expression of the relaxation time depends on the factor ΔE which represents the height of the barrier and to calculate ΔE one needs to know the energy at the maximum angle which cannot be determined analytically.

6.4 Interacting Nanoparticles

The interparticle dipole-dipole interactions or simply the dipolar interaction, are at the center of intensive theoretical and experimental investigations due to their important effects on the magnetic nanoparticles. For example, they induce ferromagnetic ordering of free dipoles sitting on Fcc lattice (Luttinger and Tisza [1946]), super-spin glass behavior(Djurberg et al. [1997]; Mamiya et al. [1999]), or Super-Ferromagnetism (SFM) (Mørup et al. [1983]; Rancourt and Daniels [1984]). The effects of the dipolar interaction on the magnetization reversal processes in fine ferromagnetic monodomain nanoparticles is a debated question whose answers are not only different but even contradictory. Theoretically, there exit

models stating that the dipolar interaction speed up the reversal process (Hansen and Mørup [1998]; Mørup and Elisabeth [1994]) and other models predicting the inverse that is the dipolar interaction slow down the process (Dormann et al. [1988]; El-Hilo et al. [1992]). On the other hand, the performed experiments yields also contradictory results since it is not easy to obtain samples of nanoparticles with an effective control on the different parameters of the dipolar interaction such as interparticle distance, anisotropy...(Dormann et al. [1988]; Mørup and Elisabeth [1994]).

6.4.1 Mean Field Approximation

(Denisov [1999]) To account for the influence of the dipolar interaction a mean field approximation is used. In the mean field approximation, the nanoparticles in a given ensemble are considered to be independent of each others and are treated as isolated nanoparticles. Consequently, the dynamics of each nanoparticle could be described either by the LLG equation or by the equivalent Fokker Planck equation derived by Brown (Brown [1963]).
Consider an ensemble of N spherical monodomain nanoparticles distributed over a lattice with S sites. To calculate the mean dipolar magnetic field $\overrightarrow{H_d(t)}$ on a given nanoparticle, first we have to compute the local dipolar field $\overrightarrow{h(t)}$ that the nanoparticle experiences from the other nanoparticles:

$$\overrightarrow{h(t)} = \sum_i \frac{3\overrightarrow{r}_i(\overrightarrow{m}_i.\overrightarrow{r}_i) - r_i^2\overrightarrow{m}_i}{r_i^5} \tag{6.22}$$

The index i denotes all the nanoparticles other than the addressed nanoparticle. Provided that particles are initially supposed to be oriented parallel to the easy axis (the z−axis), we average $\overrightarrow{h(t)}$ over all the possible configurations that the nanoparticles may take in the lattice,

$$\begin{aligned} \overrightarrow{H(t)} &= <\overrightarrow{h(t)}> \\ &= <\sum_i \frac{3r_{iz}^2 - r_i^2}{r_i^5}\overrightarrow{m_{iz}(t)}> \end{aligned}$$

$$= \lim_{V\to\infty} \frac{1}{R} \sum_{\sigma}^{R} \sum_{\mathbf{r}_\sigma} \frac{3r_{\sigma z}^2 - r_\sigma^2}{r_\sigma^5} \overline{m_{\sigma z}(t)}$$

$$= \lim_{V\to\infty} \frac{R1}{R} \sum_{\mathbf{r}} \frac{3r_z^2 - r^2}{r^5} \Big(\frac{1}{R1} \sum_{l=1}^{R1} \overline{m_z^l(t)} \Big)$$

$\mathbf{r}$=radius vector of the i^{-th} particle=$d_1(n_{1i}\overrightarrow{e_x} + n_{2i}\overrightarrow{e_y}) + d_2 n_{3i}\overrightarrow{e_z}$.
R=number of total permutations=$S!/(N-S)!$.
R1=number of permutations for a given site=$(N/S)R$.
p=(N/S)=probability of occupation of a given site.
$S(\xi)$=distribution function, where $\xi = d_2/d_1$:

$$S(\xi) = \frac{1}{8} \sum_{n_1,n_2,n_3} \frac{2\xi^2 n_3^2 - n_1^2 - n_2^2}{(n_1^2 + n_2^2 + n_3^2)^{\frac{5}{2}}} \tag{6.23}$$

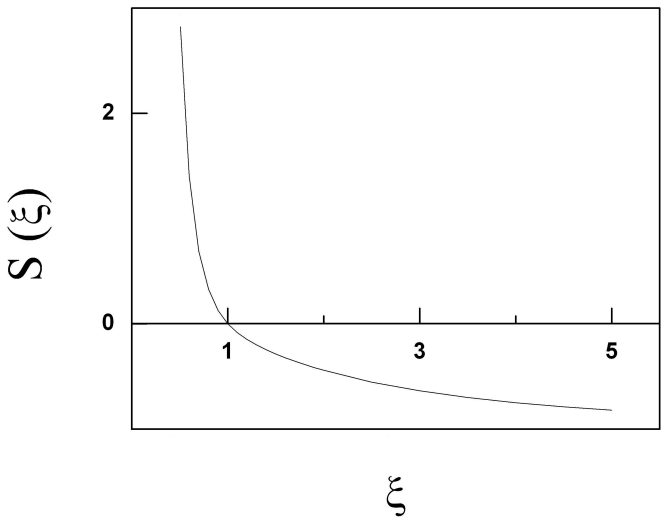

Figure 6.12: The function $S(\xi)$ for 100 particles on the x,y and z axes.

Thus, the mean dipole magnetic field is:

$$\overrightarrow{\overline{H_d(t)}} = 8pS(\xi)d^{-3}\overline{m_z(t)} \tag{6.24}$$

where $\overline{m_z(t)} = m\int_0^\pi \cos(\theta)W(\theta,t)d(\cos(\theta))$ and d being the distance from the center of the first nanoparticle to the center of the next one.

The existence or the absence of the ferromagnetic order in a given ensemble of nanoparticles could be understood as a result of a competition between different interparticle forces such as the anisotropy, exchange and the dipolar forces (Denisov [1999]). The contribution of the dipolar forces is determined through the sign of equation 6.23 which indicates that there are two types of forces: $1-$ forces of dipoles with $3r_z^2 - r^2 \leq 0$ producing a mean dipolar field anti$-$parallel to the total magnetization of the sample and $2-$ forces of dipoles with $3r_z^2 - r^2 > 0$ producing a dipolar field parallel to the total magnetization of the sample. And thus, the competition between these forces determines the nature of ordering.
In this work, we study 2D systems of nanoparticles which corresponds to the case where as $\xi \to \infty$ $S(\xi)$ tends to -1.129.

6.4.2 Discretization Scheme and Boundary Conditions

To account for interparticle dipolar interaction, we modify the total energy of the nanoparticle and consequently the first part of the discretized equation i.e. equation 7.2. The new equations are:

$$E(\theta) = KV\sin^2\theta - \mu_0 V M_s\cos\theta - \mu_0\overrightarrow{m}.\overrightarrow{\overline{H_d(t)}} \tag{6.25}$$

$$\frac{\partial W}{\partial \widehat{t}} = \frac{\partial}{\partial x}\Big(U(x)W\Big) = \frac{\partial}{\partial x}\Big((1-x^2)(Ax+B+C)\Big) \tag{6.26}$$

where C is the strength of the dipolar interaction:

$$C = -\frac{\mu_0 M_s V}{2\pi K_B T}8pSd^{-3}\overline{m_z(t)} \tag{6.27}$$

N.B. Both the discretization scheme and the boundary conditions are not affected by the modifications. To determine the relaxation time, we follow the same

method of the non-interacting nanoparticles.
Finally, to check the consistency of our numerical results, we perform the following tests:

- Similarly, verify always that the total number of configurations conserved that is $\int_{-1}^{1} W dx$=1 at any time instant.
- For the convergence test, we calculate the boltzmann distribution numerically and then compare it to the final distribution of the initial configuration (a half−gaussian distribution).

6.4.3 Numerical Results

In order to make a comparison with the isolated nanoparticles, we performed simulations on an ensemble of the same Co nanoparticles where each has the following properties:

- $V = 8 * 10^{-24} m^3$ Total volume of the particle.
- $K = 4.2 * 10^5 J/m^3$ Anisotropy Constant.
- $\mu_s = N\mu_B * 1.7 = 1.12 * 10^{-17} J/T$ Saturation magnetic moment.
- $Ms = \mu_s/V = 1.4 * 10^6 A/m$ Saturation magnetization.
- $S(\xi) \approx -1.129$.
- $\mid H_0 \mid = 0.2/\ \mu_0 A/m$ Intensity of the applied field.

6.4.3.1 Variation of τ with $1/T$

On figure 6.13, we plot the variation of τ with $1/T$ for isolated and interacting nanoparticles. The interparticle distance (center to center) considered is 25 nm and the probability of occupation p=0.5. The obtained results show that the inclusion of the dipolar interaction accelerates the reversal process at low temperatures e.g. for $\Delta E/K_BT$=2, $\tau_{isol} \approx 1$ ns whereas $\tau_{inter} \approx 0.1$ ns. However, at high temperature up to $\Delta E/K_BT$=0.1, the interacting nanoparticles behaves as

the isolated ones. In fact, as the temperature increases the strength of the dipolar interaction decreases (equation 6.27)), then at high temperatures the dipolar interaction is expected to be weak.

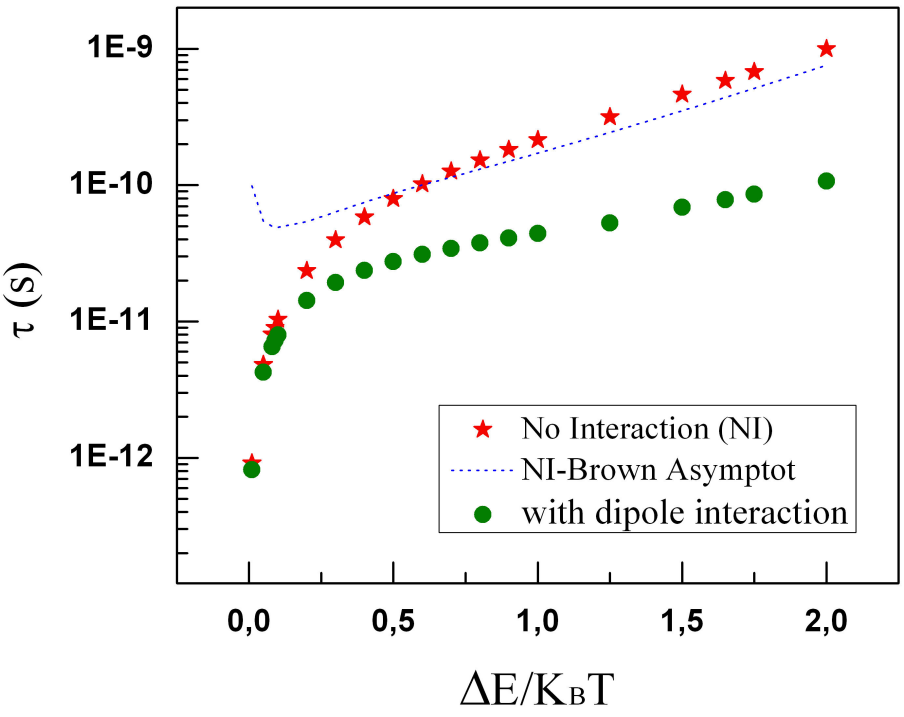

Figure 6.13: The variation of τ as a function of $1/T$ for damping constant α=1: numerical results (red) and brown asymptote for no interaction (dashed line), dipolar interaction for d=25 nm (green).

In the following two sub−sections, we study how does the reversal process could be affected by the different parameters of the dipolar interaction, such as the interparticle distance and the density of the particle.

6.4.3.2 Effect of the interparticle distance

The interparticle distance is a key parameter for the interparticle dipolar interaction. The interaction varies as d^{-3}, therefore as the distance between the

nanoparticles decreases, the dipolar interaction becomes more effective and its contribution in the total energy leads to a decrease in the height of the barrier and consequently it accelerates the process of reversal .
The results plotted on figure 6.14 confirm these theoretical predictions, for instance, it shows that for long enough interparticle distance the dipolar interaction effect is weak and the nanoparticles behave as isolated ones (similar to results for d=50 nm). In general and for any values of the parameters of the nanoparticles studied, it is found that the dipolar interaction can be neglected for d≥ 4*r (r: radius of the nanoparticle).

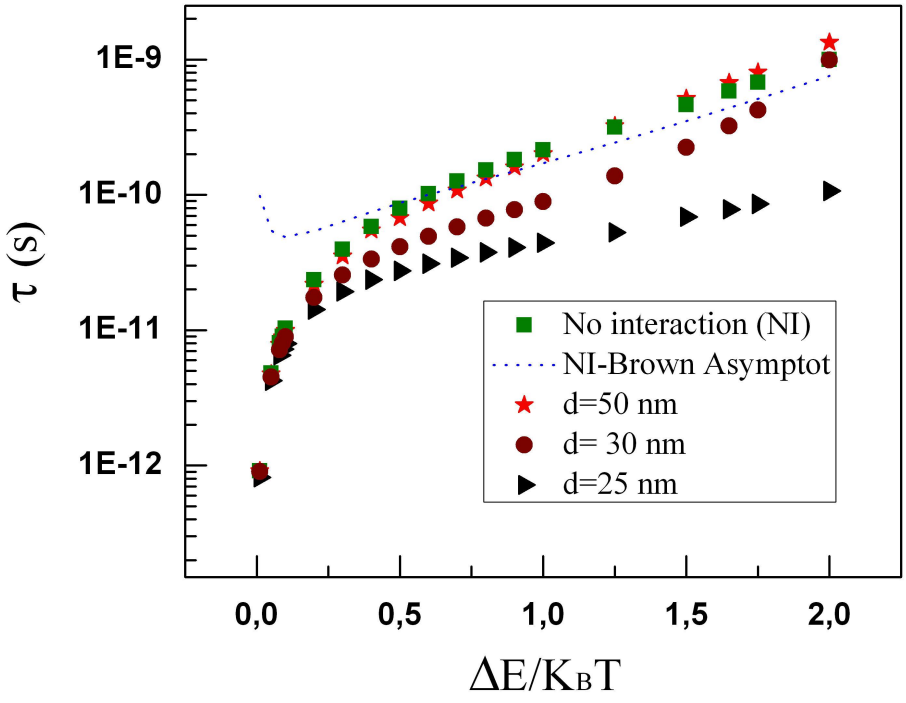

Figure 6.14: The variation of τ as a function of $1/T^{-1}$ for different interparticle distances d: numerical results (green) and brown asymptote for no interaction (dashed line), dipolar interaction for distances: 50 nm (red),30 nm (wine) and 25 nm (black). p=0.5 and α=1.

6.4.3.3 Effect of the probability of occupation

In dense samples of nanoparticles, the dipolar interaction becomes more and more relevant. Qualitatively, this can be explained as follows: the increase in the density of the nanoparticles leads to an increase in the saturation value of the magnetic moment of the nanoparticles which in turn increases the amplitude of the dipolar interaction i.e. the factor C in the equation 6.27.

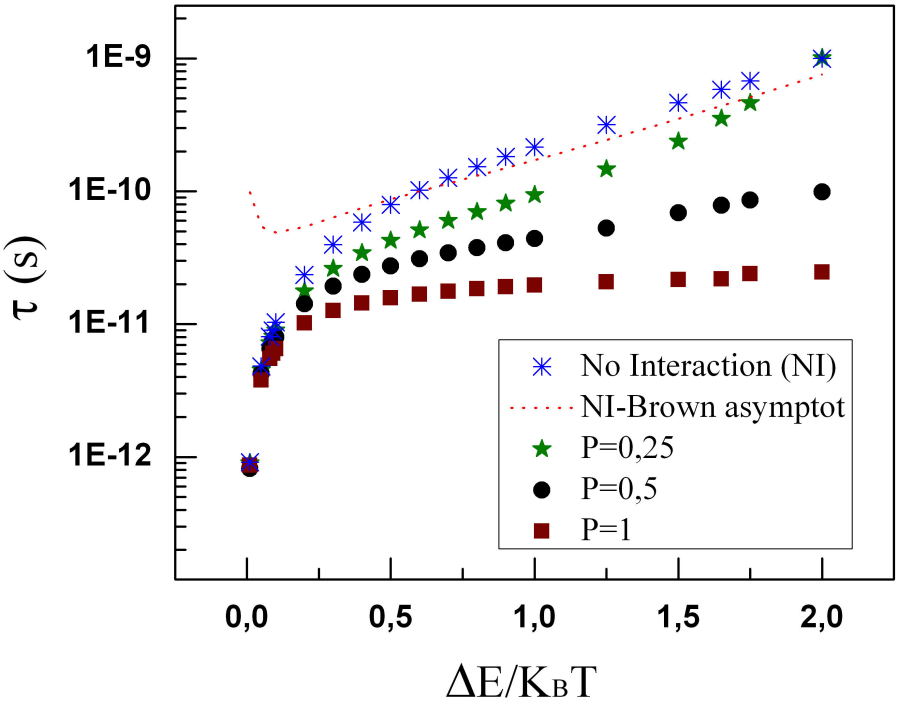

Figure 6.15: The variation of τ as a function of $1/T^{-1}$ for different occupation numbers: numerical results (blue) and brown asymptote for no interaction (dashed line), dipolar interaction for probability of occupation: 0.25 (green), 0.5 (black) and 1 (wine). d= 25 nm and α=1.

In our model 6.24, the parameter **p** represents the probability of occupation of the nanoparticles in a given lattice and it can be viewed as the density of the nanoparticles. What we observe from the numerical results plotted on figure 6.15

is that the relaxation time decreases as the density of particles increases meaning that the reversal process becomes faster. Actually, these findings confirm the preceding results and is consistent with the theoretical predictions.

6.4.3.4 Experimental Parameters

Following these important results on the effects of the dipolar interaction, we repeated the same simulations on another set of parameters corresponding to the native samples that we have studied experimentally.
The native samples are dense samples of Core/Shell CoPt nanoparticles with 4.75 nm Co core nanoparticle surrounded by a 1.82 nm platinum shell. Each two nanoparticles are separated by 0.2265 nm shell to shell distance.

- $V = 5.6115 * 10^{-26} m^3$ Total volume of the particle.
- $r = 2.375$ nm Radius of the particle.
- $K = 4.2 * 10^5 J/m^3$ Anisotropy Constant.
- $\mu_s = N\mu_B * 1.7 = 8.1 * 10^{-20} J/T$ Saturation magnetic moment.
- $Ms = \frac{\mu_s}{V} = 1.4 * 10^6 A/m$ Saturation magnetization.
- $S(\xi) \approx -1.129$.
- $d = 8.617$ nm Interparticle distance.
- $p = 1$ Occupation number.
- $\mid H_0 \mid = 0.2/\ \mu_0 A/m$ Intensity of the applied field.

6.4.3.5 Effect of the angle of the applied field ψ

Our model for the mean-field dipolar interaction (Denisov [1999]; Denisov et al. [2004]) supposes that the self-consistent dipolar field is always aligned with the axis of easy magnetization. Thus, it allows us to consider only the cases where the external field is either parallel (ψ =0°) or antiparallel (ψ=180°) to the axis of easy magnetization.

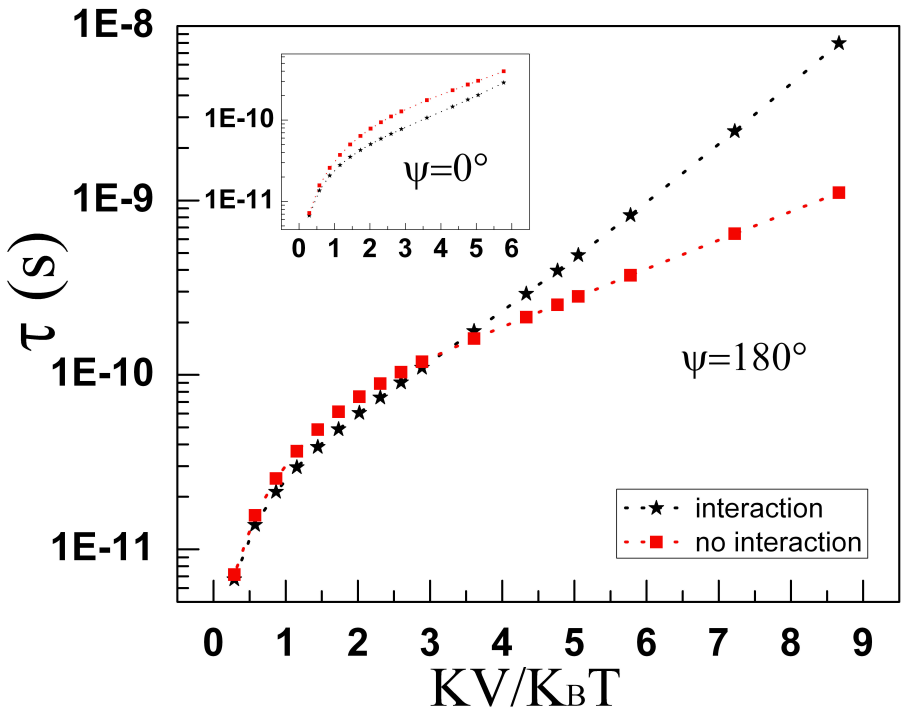

Figure 6.16: Relaxation time τ vs the normalized inverse temperature, for an external field applied antiparallel to the direction (ψ=180°).The inset shows the same result for of easy magnetization (ψ=0°)

The results which are plotted on figure 6.16 show that the angle of the external field influences remarkably the role of the dipolar interaction. We found that as a function of the angle, the dipolar interaction might accelerate or decelerate the reversal process. For instance, when the field is applied parallel to the z−axis (ψ=0°), the effect of the dipolar interaction is to shorten the relaxation time, i.e., to accelerate the reversal of the magnetization. In contrast, for the antiparallel configuration (ψ=180°), the relaxation time is longer when the interactions are taken into account, at least for temperatures below a certain threshold (here the threshold is situated near $KV/K_BT = 1.25$, corresponding to a temperature $T = 1365$ K).

We postulate the existence of a threshold angle, above which such an effect could be observed. However, this cannot be done with our model and a more sophisti-

cated approach would be needed to investigate this effect for arbitrary values of the angle ψ.
Actually, the dipolar field that we have used to account for the dipolar interaction, assumes that the magnetic moments are initially aligned parallel to the z−axis. The corresponding energy minima are at 0 and π. However, if the external magnetic field is applied with a given angle ψ, the moments will be aligned along the direction of the external field, and this violates our assumption. Besides, this will shift the energy minima. However, we think that we can still use the mean field approach, but we should adapt the equations so that to take into account this re−orientation of the moments as well as the shift in the energy minima.

b− Variation of τ with the p

In chapter 3 we mentioned that the dipolar contribution in the non−annealed sample is weak (hysteresis at 5K perpendicular direction). This result is numerically confirmed as can be seen from figure 6.17 where it shows that even if the lattice is fully occupied by the nanoparticles i.e. **p**=1, the obtained relaxation times are very close to those of the isolated nanoparticles.

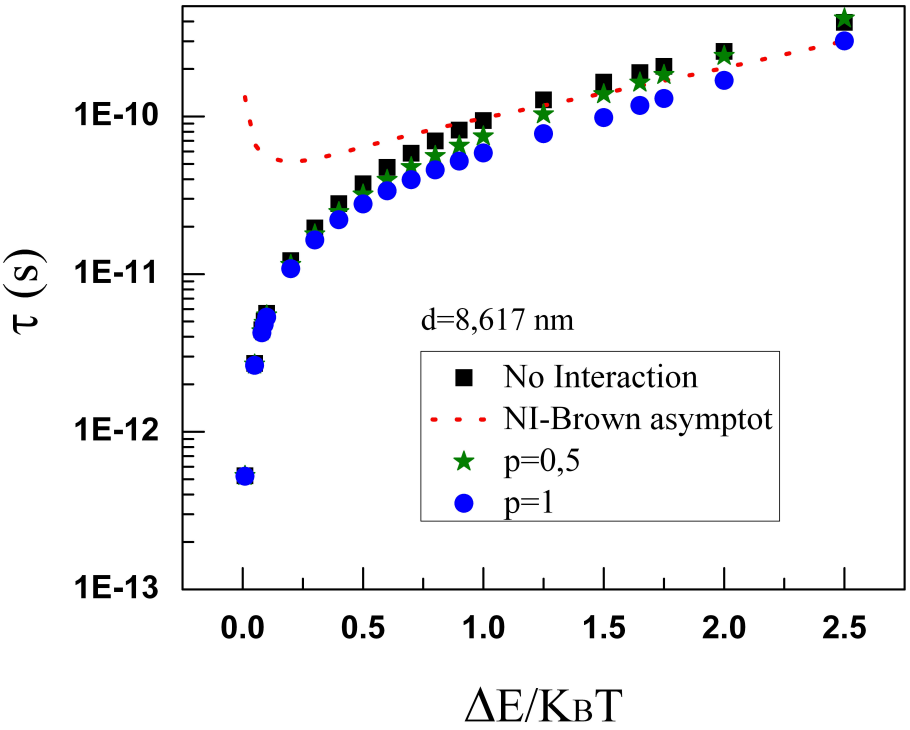

Figure 6.17: The variation of τ as a function of $1/T^{-1}$ for different occupation numbers: numerical results (black) and brown asymptote for no interaction (dashed line), dipolar interaction for probability of occupation: 0.5 nm (green) and 1 (blue). d=8.617 nm and α=1.

b– Variation of τ with the field

In this part, we compare the numerical and the experimental relaxation times. The experimental relaxation times correspond to the damping time of the magnetization vector precession which is obtained by fitting the differential magnetization signal measured for one field direction with a cosine function mentioned in section 5.2.2. Here the magnetic field direction is 0° with respect to the normal of the sample.

The simulations are made at T=520 K. The temperature was obtained form the two temperature simulations shown on figure 6.18.

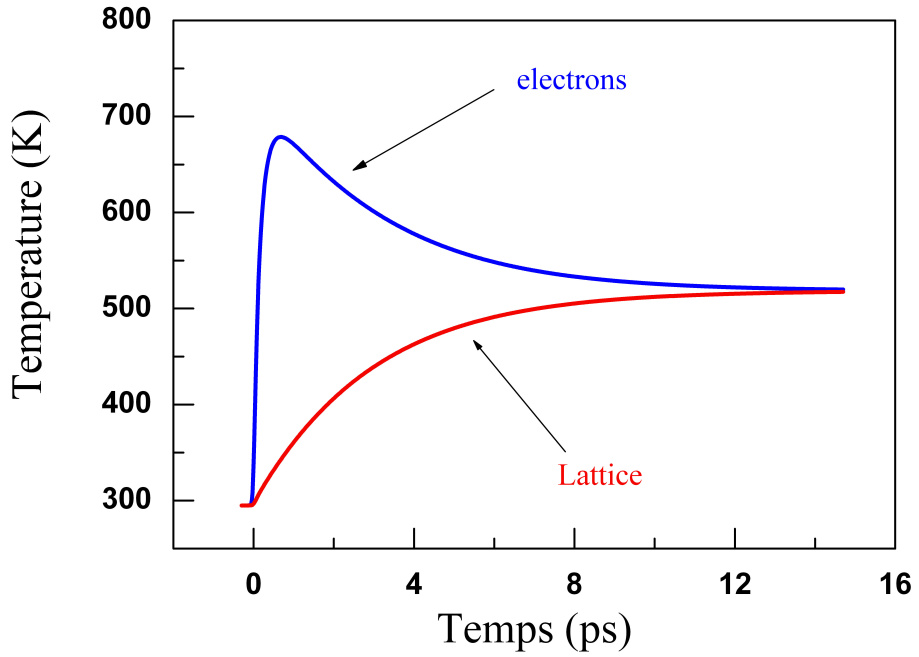

Figure 6.18: Two temperature simulations: electron temperature (blue) and lattice temperature (red).

The results show that when the interactions are taken into account, our numerical model produces relaxation times that are close to the experimental times. Also, it is observed that the relaxation time increases as the strength of the applied field increases. And this is compatible with the fact that the external field aligns the magnetic moments of the nanoparticles making the reversal process slower.

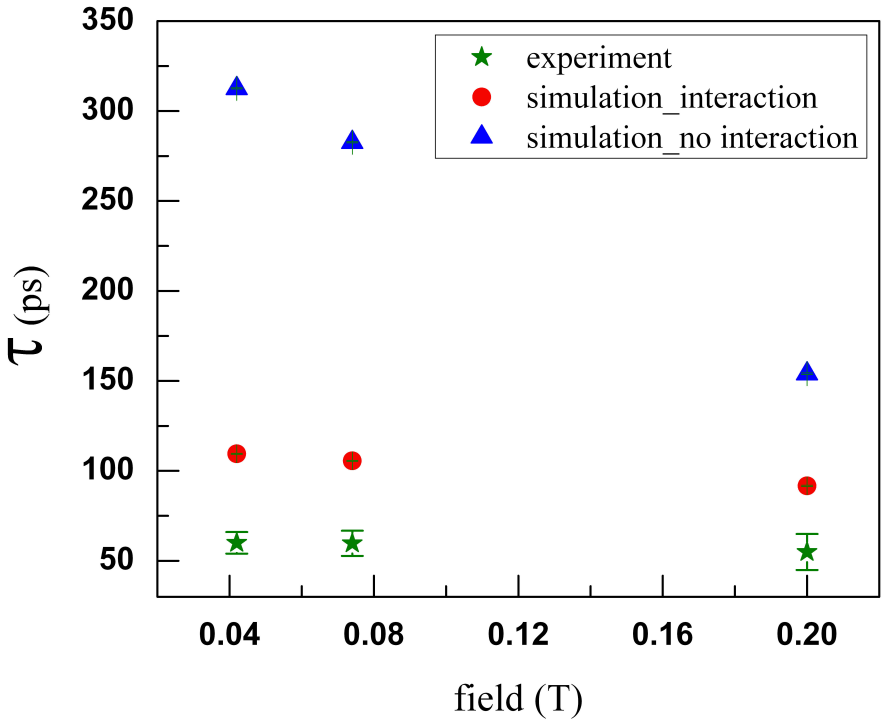

Figure 6.19: Comparison between the numerical and the experimental relaxation times. Parameters: S=-1.129, p=1, d=8.617 nm, α=1: experiment (olive), simulation with interaction (red) and simulation without interaction (blue).

The following table shows the different relaxation times:

Magnetic field (T)	Relaxation time (ps)		
	Experiment	Simulation	
		no interaction	interaction
0.04	60 ± 6	312.56 ± 0.29	109.5 ± 0.28
0.07	59.71 ± 7	282.63 ± 0.32	105.6 ± 0.29
0.2	54.89 ± 10	153.98 ± 0.42	91.7 ± 0.37

Figure 6.20: Relaxation times.

6.5 Conclusions

In this chapter, we have addressed the magnetization reversal process throughout the calculation of the corresponding relaxation times for both isolated and interacting nanoparticles.
In a first approach, we have studied isolated nanoparticles. Despite of a failure at high temperatures, the numerical results hold an important and clear evidence on the validity of the Néel−Brown model to describe the reversal processes in such types of nanoparticles. This validity is confirmed in paragraph 6.3.3.1.
A simple comparison of the obtained results with those of other numerical approaches (LD, MC,..) showed the reliability of the used numerical approach. Furthermore, it is demonstrated that the approach is capable of providing a precise description of the reversal process even in the limit of low damping.
The second part of the chapter was devoted to interacting nanoparticles. To account for the interparticle dipolar interaction in 2D ensembles of nanoparticles, a mean field approximation was introduced. The results show an important deviation from the asymptotic behavior of brown for non-interacting nanoparticles. The general conclusion about the effects of the dipolar interaction, is that they accelerate the reversal process. For that, we have tested the effects of the different parameters of the dipolar interaction such as the interparticle distance, the density of particles. It is found that the relaxation time decreases as the distance increases and also as the density of the particles increases.
In a direct connection to experiment, it is shown that the numerical results are in accordance with the experimentally measured values.

Chapter 7

Global Conclusions and Perspectives

My PhD Thesis is divided into two parts: an experimental part and a theoretical part. In the first part we have used Time Resolved Magneto Optical Kerr Effect TR−MOKE to study the magnetization dynamics in 3D arrangements of $Co_{core}Pt_{shell}$ nanoparticles. We come out with the following conclusions:

- TR−MOKE manifests itself is a performing tool to address the different dynamical magnetic processes that occur on ultrashort time scales. In addition, TR−MOKE provides the possibility to study the charge dynamics at the same time.
- The CoPt nanoparticles in core/shell configuration emerge as a serious candidate to be considered in future developments of the magnetic storage media.
- **Concerning the magnetization dynamics:** We have studied two types of $Co_{core}Pt_{shell}$ samples: non−annealed and annealed samples (annealing temperature=650K). The overall dynamics observed on both types, occur during the thermalization of the electrons and it is followed by a re−magnetization. However, the details of the dynamics are completely different. For example, both thermalization and relaxation processes are observed to be slower on the annealed samples with respect to those on the non−annealed samples.

More importantly, on the long timescale we have observed a precessional dynamics of the magnetization vector on the annealed samples that does not exist on the non−annealed samples.
This difference in the dynamics is caused by the thermal annealing. Indeed, the thermal annealing induced a diffusion of platinum in the cobalt core leading to the formation of a CoPt crystalline phase which is an indication of ferromagnetism. In other words, the thermal annealing induced a magnetic phase transition in the nanoparticles from superparamagnetic with a blocking temperature T_B=66 K to ferromagnetic with a blocking temperature (T_B >350 K).
The induced ferromagnetic phase has two main features: first an increase of the values of magnetization at saturation of the samples. Second, an increase in the anisotropy constant K_1.

- **Concerning the charge dynamics:** We reported a typical charge dynamics on both types of the samples: a laser excitation is followed by a thermalization of the highly excited electrons to the fermi level, then a relaxation to the lattice and finally a lattice heat diffusion process. We have observed two types of oscillations: the first one has a characteristic period of $\sim$ 2 ps corresponding to the the breathing mode vibrations of the individual nanoparticles. The second oscillatory behavior was observed only on the non−annealed samples. It corresponds to a collective coherent vibration of the nanoparticles with a 146 $\pm$ 2 ps. These oscillations are attributed to a local supracrystalline ordering induced by a mild laser annealing.
  It is Due to the thermal annealing of the samples that these oscillations completely disappeared. Also, the thermal annealing resulted in faster thermalization of the electrons as it increased the scattering cross−section of the electrons.

In the second part, a numerical studies of the magnetization reversal processes in isolated and interacting nanoparticles as well are presented. We come out with the following conclusions:

- Indeed, numerical simulations appears as an effective player at the interface

between theoretical models and experiments capable of producing reliable physical results.

- For isolated nanoparticles, we have found that the N*é*el−Brown model helps to have better understanding of the main aspects of the magnetization dynamics at low temperatures.

- For the interacting nanoparticles, we have used a mean field approximation to calculate a mean dipolar field. The obtained relaxation times deviates from the Arrhenius law:

$$\frac{1}{\tau} = \frac{1}{\tau_0} exp\Big(- \frac{KV}{K_B T}\Big)$$

  Generally, we have found that the dipolar interactions accelerates the reversal process. Also, we have studied the effect of a magnetic field applied with a given angle with respect to the easy axis of magnetization. We have found that above a given temperature, there exist a threshold angle at which the effect of the dipolar interactions is completely reversed.

Perspectives

There are still many things that could be done experimentally with the pellets especially for the characterization of the dipole−dipole interactions. For the non−annealed samples, it would be good to study them at low temperatures (below the corresponding T_B) to characterize the effects of the dipole−dipole interactions on the magnetization dynamics.
For the theoretical study:

- Study the annealed samples where the effects of the dipolar interactions are strong with respect to the native samples.

- Study the effects of the temperature on the reversal process.

- Develop the study to 3D systems of nanoparticles.

- Study the effects of the precession of magnetization vector on the reversal process.

Appendix A: Boundary Conditions

Consider the equation that we want to solve numerically:

$$\frac{\partial W}{\partial \widehat{t}} = \frac{\partial}{\partial x}\Big(U(x)W\Big) + \frac{\partial}{\partial x}\Big(D(x)\frac{\partial W}{\partial x}\Big) \tag{7.1}$$

To find the suitable boundary conditions: 1− we decompose the above equation into two parts, 2− find the boundary conditions of each, and finally 3− combine them to get the boundary conditions of the main equation.

The first part is :

$$\frac{\partial W}{\partial \widehat{t}} = \frac{\partial}{\partial x}\Big(U(x)W\Big) \tag{7.2}$$

- at $x = -1$, the equation is discretized as follows:

$$\frac{\partial}{\partial x}\Big(U(x)W\Big) = \beta\Big(\frac{U_{j+1}W^i_{j+1} - U_jW^i_j}{\Delta x}\Big)$$

  the point $x = -1$ corresponds to the grid node j=0 on the spatial grid,thus

$$\frac{\partial}{\partial x}\Big(U(x)W\Big)_{-1} = \beta\Big(\frac{U_1W^i_1}{\Delta x}\Big)$$

- at $x = 1$, the equation is discretized as follows:

$$\frac{\partial}{\partial x}\Big(U(x)W\Big) = \beta\Big(\frac{U_jW^i_j - U_{j-1}W^i_{j-1}}{\Delta x}\Big)$$

the point $x = 1$ corresponds to the grid node j=s on the spatial grid,thus

$$\frac{\partial}{\partial x}\Big(U(x)W\Big)_1 = -\beta\Big(\frac{U_{s-1}W^i_{s-1}}{\Delta x}\Big)$$

therefore, the boundary conditions for this part are:

- $W_0^{i+1} = W_0^i + \beta\Big(\frac{U_1 W_1^i}{\Delta x}\Big)$
- $W_s^{i+1} = W_s^i - \beta\Big(\frac{U_1 W_1^i}{\Delta x}\Big)$

To find β, we need to calculate the summation $\sum_{j=0}^{s} W_j^{n+1}$, knowing that for 1$\leq$ j$\leq$ s$-$1 the first part is discretized as follows:

$$\frac{\partial}{\partial x}\Big(U(x)W\Big) = \frac{U_{j+1}W^i_{j+1} - U_{j-1}W^i_{j-1}}{2\Delta x}$$

we find that:

$$\sum_{j=0}^{s} W_j^{n+1} = \sum_{j=0}^{s} W_j^n + (2\beta - 1)\frac{\Delta t}{2\Delta x}U_1 W_1 - (2\beta - 1)\frac{\Delta t}{2\Delta x}U_{s-1}W_{s-1} \tag{7.3}$$

provided that the total number of configurations should be conserved,i.e

$$\sum_{j=0}^{s} W_j^{n+1} = \sum_{j=0}^{s} W_j^n$$

we conclude that β should be 1/2.

The second part is :

$$\frac{\partial W}{\partial \widehat{t}} = \frac{\partial}{\partial x}\Big(D(x)\frac{\partial W}{\partial x}\Big) \tag{7.4}$$

- at $x = -1$, the equation is discretized as follows:

$$\frac{\partial}{\partial x}\left(D(x)\frac{\partial W}{\partial x}\right) = \phi\Big(\frac{\Big(D_{j+1} - D_j\Big)\Big(W^i_{j+1} - W^i_j\Big)}{\Delta x^2}\Big)$$

the point $x = -1$ corresponds to the grid node j=0 on the spatial grid,thus

$$\frac{\partial}{\partial x}\left(D(x)\frac{\partial W}{\partial x}\right)_{-1} = \phi\Big(\frac{\Big(D_1\Big)\Big(W_1^i - W_0^i\Big)}{\Delta x^2}\Big)$$

- at $x = 1$, the equation is discretized as follows:

$$\frac{\partial}{\partial x}\left(D(x)\frac{\partial W}{\partial x}\right) = \phi\Big(\frac{\Big(D_j - D_{j-1}\Big)\Big(W_{j-1}^i - W_{j-1}^i\Big)}{\Delta x^2}\Big)$$

the point $x = 1$ corresponds to the grid node j=s on the spatial grid,thus

$$\frac{\partial}{\partial x}\left(D(x)\frac{\partial W}{\partial x}\right)_{1} = -\phi\Big(\frac{\Big(D_{s-1}\Big)\Big(W_s^i - W_{s-1}^i\Big)}{\Delta x^2}\Big)$$

therefore, the boundary conditions for this part are:

- $W_0^{i+1} = W_0^i + \phi\frac{\Delta t}{\Delta x^2}\Big(D_1\Big)\Big(W_1^i - W_0^i\Big)$
- $W_s^{i+1} = W_s^i - \phi\frac{\Delta t}{\Delta x^2}\Big(D_{s-1}\Big)\Big(W_s^i - W_{s-1}^i\Big)$

for 1≤ j≤ s-1 this part is discretized as follows:

$$\begin{aligned}\frac{\partial}{\partial x}\left(D(x)\frac{\partial W}{\partial x}\right) &= (D_{j+1} + D_j)\Big(\frac{W_{j+1}^i}{2\Delta x^2}\Big) + (D_{j-1} + D_j)\Big(\frac{W_{j-1}^i}{2\Delta x^2}\Big)\\ &- (D_{j+1} + D_{j-1} + 2D_j)\Big(\frac{W_j^i}{2\Delta x^2}\Big)\end{aligned}$$

and the summation $\sum_{j=0}^{s} W_j^{n+1}$ gives:

$$\sum_{j=0}^{s} W_j^{n+1} = \sum_{j=0}^{s} W_j^n + (2\phi - 1)\frac{\Delta t}{\Delta x^2}\Big(W_0^i - W_1^i - W_{s-1}^i + W_s^i\Big) \tag{7.5}$$

for the same reason as β, ϕ should be 1/2.

Therefore, the boundary conditions are:

- at j=0:

$$W_0^{i+1} = W_0^i + \frac{1}{2}U_1\frac{\Delta t}{\Delta x}W_1^i + \frac{1}{2}D_1\frac{\Delta t}{\Delta x^2}(W_1^i - W_0^i) \tag{7.6}$$

- at j=s:

$$W_s^{i+1} = W_s^i - \frac{1}{2}U_{s-1}\frac{\Delta t}{\Delta x}W_{s-1}^i - \frac{1}{2}D_{s-1}\frac{\Delta t}{\Delta x^2}(W_s^i - W_{s-1}^i) \tag{7.7}$$

References

Acremann, Y., Back, C. H., Buess, M., Portmann, O., Vaterlaus, A., Pescia, D., and Melchior, H. (2000). Imaging precessional motion of the magnetization vector. *Science*, 290:492. 7

Agranat, M. B., Ashitkov, S. I., Granovskii, A. B., and Rukman, G. I. (1984). Interaction of picosecond laser pulses with the electron, spin and phonon subsystems of nickel. *Sov. Phys. JETP*, 59:804–806. 39

Aharoni, A. (1973). Relaxation time of superparamagnetic particles with cubic anisotropy. *Phys. Rev. B*, 7(3):1103–1107. 37

Aharoni, A. (1996). *Introduction to the Theory of Ferromagnetism*. Oxford University Press. 21

Andrade, L. H. F., Laraoui, A., Vomir, M., Muller, D., Stoquert, J.-P., Estournès, C., Beaurepaire, E., and Bigot, J.-Y. (2006). Damped precession of the magnetization vector of superparamagnetic nanoparticles excited by femtosecond optical pulses. *Phys. Rev. Lett.*, 97(12):127401. 37

Argyres, P. N. (1955). Theory of the faraday and kerr effects in ferromagnetics. *Phys. Rev.*, 97(2):334–345. 56

Arias, P., Altbir, D., and Bahiana, M. (2005). Geometric aspects of the dipolar interaction in lattices of small particles. 17:16251633. 73

Atxitia, U., Chubykalo-Fesenko, O., Kazantseva, N., Hinzke, D., and Nowak, U.and Chantrell, R. W. (2007). Micromagnetic modeling of laser-induced magnetization dynamics using the landau-lifshitz-bloch equation. *Appl. Phys. Lett.*, 91:232507. 99

Barnett, S. J. (1915). Magnetization by rotation. *Phys. Rev.*, 6(4):239–270. 1

Beaurepaire, E., Merle, J.-C., Daunois, A., and Bigot, J.-Y. (1996). Ultrafast spin dynamics in ferromagnetic nickel. *Phys. Rev. Lett.*, 76(22):4250–4253. viii, 9, 39, 40, 47

Bigot, J.-Y. (2001). Femtosecond magneto-optical processes in metals. *C. R. Acad. Sci., Ser IV: Phys., Astrophys.* 39, 46, 57

Bigot, J.-Y., Guidoni, L., Beaurepaire, E., and Saeta, P. N. (2004). Femtosecond spectrotemporal magneto-optics. *Phys. Rev. Lett.*, 93(7):077401. 39, 68, 69

Bigot, J.-Y., Halté, V., Merle, J.-C., and Daunois, A. (2000). Electron dynamics in metallic nanoparticles. *Chem. Phys.*, 251:181–203. 85

Bigot, J.-Y., Vomir, M., Andrade, L., and Beaurepaire, E. (2005). Ultrafast magnetization dynamics in ferromagnetic cobalt : The role of the anisotropy. *Chemical Physics*, 318:137 – 146. 39, 48, 96

Bigot, J.-Y., Vomir, M., and Beaurepaire, E. (2009). Coherent ultrafast magnetism induced by femtosecond laser pulses. *Nature Physics*, 5. 46

Bloch, F. (1946). Nuclear induction. *Phys. Rev.*, 70(7-8):460–474. 49

Boeglin, C., Beaurepaire, E., Halt, V., Lpez-Flores, V., Stamm, C.and Pontius, N., Drr, H., and Bigot, J.-Y. (2010). Distinguishing the ultrafast dynamics of spin and orbital moments in solids. *Nature*, 465:458461. 10, 41

Brown, W. F. (1959). Relaxational behavior of fine magnetic particles. *Journal of Applied physics*, 30(4):130S. 30

Brown, W. F. (1963). Thermal fluctuations of a single-domain particle. *Phys. Rev.*, 130(5):1677–1686. 8, 11, 18, 23, 99, 100, 102, 106, 118

Chikazumi, S. and Charap, S. (1964). *Physics of Magnetism*. John Wiley & Sons, Inc., New York. 18

Chubykalo, O., Nowak, U., Smirnov-Rueda, R., Wongsam, M. A., Chantrell, R. W., and Gonzalez, J. M. (2003). Monte carlo technique with a quantified time step: Application to the motion of magnetic moments. *Phys. Rev. B*, 67(6):064422. 99, 114

Coffey, W. T., Crothers, D. S. F., Dormann, J. L., Geoghegan, L. J., Kalmykov, Y. P., Waldron, J. T., and Wickstead, A. W. (1995). Effect of an oblique magnetic field on the superparamagnetic relaxation time. *Phys. Rev. B*, 52(22):15951–15965. 36

Coffey, W. T., Crothers, D. S. F., Dormann, J. L., Geoghegan, L. J., and Kennedy, E. C. (1998). Effect of an oblique magnetic field on the superparamagnetic relaxation time. ii. influence of the gyromagnetic term. *Phys. Rev. B*, 58(6):3249–3266. 99

Del Fatti, N., Bouffanais, R., Vallée, F., and Flytzanis, C. (1998). Nonequilibrium electron interactions in metal films. *Phys. Rev. Lett.*, 81(4):922–925. 43

Del Fatti, N., Voisin, C., Chevy, F., Vallée, F., and Flytzanis, C. (1999). Coherent acoustic mode oscillation and damping in silver nanoparticles. *J. Chem. Phys.*, 110:11484. 83

Denardin, J. C., Brandl, A. L., Knobel, M., Panissod, P., Pakhomov, A. B., Liu, H., and Zhang, X. X. (2002). Thermoremanence and zero-field-cooled/field-cooled magnetization study of $co_x(sio_2)_{1-x}$ granular films. *Phys. Rev. B*, 65(6):064422. 71

Denisov, S. I. (1999). Long-range order and magnetic relaxation in a system of single-domain particles. *Physics of the Solid State*, 41:1672. 118, 120, 125

Denisov, S. I., Lyutyy, T. V., and Trohidou, K. N. (2004). Dipolar interaction effects on the thermally activated magnetic relaxation of two-dimensional nanoparticle ensembles. *Appl. Phys. Lett.*, 84:4672. 99, 125

Devolder, T., Crozat, P., Kim, J., Chappert, C., Ito, K., Katine, J. A., and Carey, M. J. (2006). Magnetization switching by spin torque using subnanosecond

current pulses assisted by hard axis magnetic fields. *Applied Physics Letters*, 88:152502. 7

Djurberg, C., Svedlindh, P., Nordblad, P., Hansen, M. F., Bødker, F., and Mørup, S. (1997). Dynamics of an interacting particle system: Evidence of critical slowing down. *Phys. Rev. Lett.*, 79(25):5154–5157. 37, 100, 117

Dormann, J. L., Bessais, L., and Fiorani, D. (1988). A dynamic study of small interacting particles: superparamagnetic model and spin-glass laws. *Journal of Physics C: Solid State Physics*, 21:2015. 118

Einstein, A. and De Haas, W. J. (1915a). Experimental proof of the existence of ampre's molecular currents (in english). *Koninklijke Akademie van Wetenschappen te Amsterdam*, Proceedings, 18 I:696–711. 1

Einstein, A. and De Haas, W. J. (1915b). Experimenteller nachweis der amperechen molekularstrme. *Deutsche Physikalische Gesellschaft*, 17:152–170. 1

El-Hilo, M., O'Grady, K., and Chantrell, R. (1992). Susceptibility phenomena in a fine particle system: I. concentration dependence of the peak. *Journal of Magnetism and Magnetic Materials*, 114:295. 118

Faraday, M. (1846). On the magnetization of light and the illumination of magnetic lines of force. *Trans. Roy. Soc. London*, 5:592. 54

Ferziger, J. and Peric, M. (1996). *Computational Methods for Fluid Dynamics*. Springer-Verlag Berlin Heidelberg. 104

Fowler, M. (1997). Historical beginnings of theories of electricity and magnetism. 1

Frenkel, V. Y. (1979). On the history of the einstein-de haas effect. *Soviet Physics Uspekhi*, 7:580–587. 1

Garcia-Palacios, J. (2000). On the statics and dynamics of magneto-anisotropic nanoparticles. *Advances in Chemical Physics*, 112:1–210. 22, 23, 30, 31

García-Palacios, J. L. and Lázaro, F. J. (1998). Langevin-dynamics study of the dynamical properties of small magnetic particles. *Phys. Rev. B*, 58(22):14937–14958. 101

Güdde, J., Conrad, U., Jähnke, V., Hohlfeld, J., and Matthias, E. (1999). Magnetization dynamics of ni and co films on cu(001) and of bulk nickel surfaces. *Phys. Rev. B*, 59(10):R6608–R6611. 39

Gerrits, T., Van den Berg, H. A. M., Hohlfeld, J., Bär, L., and Rasing, T. (2002). Ultrafast precessional magnetization reversal by picosecond magnetic field pulse shaping. *Nature*, 418:509–512. 7

Gilbert, T. (1955). A lagrangian formulation of the gyromagnetic equation of the magnetic field. *Phys.Rev.*, 100:1243. 20

Glauber, R. J. (1963). Time-dependent statistics of the ising model. *Journal of Mathematical Physics*, 2:294. 102

Greiner, A., Strittmatter, W., and Honerkamp, J. (1988). Numerical integration of stochastic differential equations. *J. Magn. Magn. Mater*, 51:95. 101

Grimvall, G. (1976). The electron-phonon interaction in normal metals. *Physica Scripta*, 14:63–78. 45

Guidoni, L., Beaurepaire, E., and Bigot, J.-Y. (2002). Magneto-optics in the ultrafast regime: Thermalization of spin populations in ferromagnetic films. *Phys. Rev. Lett.*, 89(1):017401. ix, 9, 41, 42, 86, 92

Halté, V., Bigot, J.-Y., Palpant, B., Broyer, M., Prével, B., and Pérez, A. (1999). Size dependence of the energy relaxation in silver nanoparticles embedded in dielectric matrices. *Appl. Phys. Lett.*, 75:3799–3801. 91

Hansen, M. and Mørup, S. (1998). Models for the dynamics of interacting magnetic nanoparticles. *Journal of Magnetism and Magnetic Materials*, 184:L262. 118

Hübner, W. and Bennemann, K. H. (1996). Simple theory for spin-lattice relaxation in metallic rare-earth ferromagnets. *Phys. Rev. B*, 53(6):3422–3427. 39

Hecht, E. (2002). *Optics*. Addison Wesley. 54

Heisenberg, W. (1928). Zur theorie des ferromagnetismus. *Z. Phys.*, 49:619–636. 13

Hodak, J. H., Heinglein, A., and Hartland, G. V. (2000). Photophysics of nanometer sized metal particles: electron-phonon coupling and coherent excitation of breathing vibrational modes. *J. Phys. Chem B.*, 104:9954–9965. 83

Hohlfeld, J., Matthias, E., Knorren, R., and Bennemann, K. H. (1997). Nonequilibrium magnetization dynamics of nickel. *Phys. Rev. Lett.*, 78(25):4861–4864. 39

Hulme, H. R. (1932). The faraday effect in ferromagnetics. *Proc. R. Soc. Lond. A135*, pages 237–257. 56

Ju, G., Nurmikko, A. V., Farrow, R. F. C., Marks, R. F., Carey, M. J., and Gurney, B. A. (1998). Ultrafast optical modulation of an exchange biased ferromagnetic/antiferromagnetic bilayer. *Phys. Rev. B*, 58(18):R11857–R11860. 39

Ju, G., Nurmikko, A. V., Farrow, R. F. C., Marks, R. F., Carey, M. J., and Gurney, B. A. (1999). Ultrafast time resolved photoinduced magnetization rotation in a ferromagnetic/antiferromagnetic exchange coupled system. *Phys. Rev. Lett.*, 82(18):3705–3708. 95

Kaganov, M., Lifshits, I., and Tanatarov, L. (1957). Relaxation between electrons and crystalline lattices. *Sov. Phys. JETP*, 4:173. 44

Kampen, M. V., Jozsa, C., Kohlhepp, J. T., LeClair, P., Lagae, L., de Jonge, W. J. M., and Koopmans, B. (2002). All-optical probe of coherent spin waves. *Phys. Rev. Lett.*, 88(22):227201. 96

Kechrakos, D. and Trohidou, K. N. (2008). Dipolar interaction effects in the magnetic and magnetotransport properties of ordered nanoparticle arrays. *Journal of Nanoscience and Nanotechnology*, 8:1–15. 73

Kerr, J. (1877). On the rotation of the plane of polarization by reflection from the pole of a magnet. *Phil. Mag.*, 3:339–343. 54

Kittel, C. (1986). *Introduction to Solid State Physics*. John Wiley & Sons, Inc., New York, 6th edition. 3, 4, 14, 15, 16, 17, 45

Kleemann, W. (2009). Switching magnetism with electric fields. *Physics*, 2:105. 6

Koopmans, B., van Kampen, M., Kohlhepp, J. T., and de Jonge, W. J. M. (2000). Ultrafast magneto-optics in nickel: Magnetism or optics? *Phys. Rev. Lett.*, 85(4):844–847. ix, 40, 41

Landau, L. D. and Lifshitz, E. M. (1935). On the theory of the dispersion of magnetic permeability in ferromagnetic bodies. *Phys. Z. Sowjet.*, 8:153. 20

Laraoui, A., Albrecht, M., and Bigot, J.-Y. (2007). Femtosecond magneto-optical kerr microscopy. *Optics Letters*, 32:936–938. 9

Lee, W., Kim, M. G., Choi, J., Park, J., Ko, S. J., Oh, S. J., and Cheon, J. (2005). Redox-transmetalation process as a generalized synthetic strategy for core-shell magnetic nanoparticles. *J. Am. Chem. Soc.*, 127:1609016097. 69

Link, S. and El Sayed, M. A. (1999). Spectral properties and relaxation dynamics of surface plasmon electronic oscillation in gold and silver nanodots and nanorods. *J. Phys. Chem B.*, 103:8410–8426. 83, 89

Lisiecki, I., Halté, V., Petit, C., Piléni, M.-P., and Bigot, J.-Y. (2008). Vibration dynamics of supra-crystals of cobalt nanocrystals studied with femtosecond laser pulses. *Adv. Mat.*, 20:1–4. 85

Lopez-Diaz, L., Torres, L., and Moro, E. (2002). Transition from ferromagnetism to superparamagnetism on the nanosecond time scale. *Phys. Rev. B*, 65(22):224406. 99

Luttinger, J. M. and Tisza, L. (1946). Theory of dipole interaction in crystals. *Phys. Rev.*, 70(11-12):954–964. 117

Lyberatos, A., Berkov, D. V., and Chantrell, R. W. (2010). A method for the numerical simulation of the thermal magnetization fluctuations in micromagnetics. *Journal of Physics: Condensed Matter*, 22:296007. 100

Mamiya, H., Nakatani, I., and Furubayashi, T. (1999). Slow dynamics for spin-glass-like phase of a ferromagnetic fine particle system. *Phys. Rev. Lett.*, 82(21):4332–4335. 37, 100, 117

Mayergoyz, I., Bertotti, G., and Serpico, C. (2009). *Nonlinear Magnetization Dynamics in Nanosystems*. Elsevier Series in Electromagnetism. 21

Metropolis, N. and Ulam, S. (1949). The monte carlo method. *Journal of the American Statistical Association*, 44:335. 101

Morrish, A. H. (1966). *The Physical Principles of Magnetism*. John Wiley & Sons, Inc., New York. 16, 49

Mørup, S. and Elisabeth, T. (1994). Superparamagnetic relaxation of weakly interacting particles. *Phys. Rev. Lett.*, 72(20):3278–3281. 12, 118

Mørup, S., Morten Bo Madsena, Franck, J., Villadsenb, J., and Kochc, J. (1983). A new interpretation of mssbauer spectra of microcrystalline goethite: super-ferromagnetism or super-spin-glass behaviour? *J. Magn. Magn. Mater*, 40:163. 37, 100, 117

Néel, L. (1949). Théorie du trainage magnétique des ferromagnétiques en grains fins avec applications aux terres cuites. *Ann. Géophys.*, 5:99. 8, 11, 18, 23, 29, 99

Nisoli, M., De Silvestri, S., Cavalleri, A., Malvezzi, A. M., Stella, A., Lanzani, G., Cheyssac, P., and Kofman, R. (1997). Coherent acoustic oscillations in metallic nanoparticles generated with femtosecond optical pulses. *Phys. Rev. B*, 55(20):R13424–R13427. 83

Nowak, U. (2001). Thermally activated reversal in magnetic nanostructures. *Ann. Rev. of computational physics*, 9:105. 101

Nowak, U., Chantrell, R. W., and Kennedy, E. C. (2000). Monte carlo simulation with time step quantification in terms of langevin dynamics. *Phys. Rev. Lett.*, 84(1):163–166. xiii, 102, 110, 112, 113, 114

Ogasawara, T., Ohgushi, K., Tomioka, Y., Takahashi, K. S., Okamoto, H., Kawasaki, M., and Tokura, Y. (2005). General features of photoinduced spin dynamics in ferromagnetic and ferrimagnetic compounds. *Phys. Rev. Lett.*, 94(8):087202. 39

Paige, D.M., S. B. and tanner, B. (1984). Redox-transmetalation process as a generalized synthetic strategy for core-shell magnetic nanoparticles. *J. Mag. Mag. Mat.*, 44:239–248. 80

Park, J. and Cheon, J. (2001). Synthesis of "solid solution" and "core-shell" type cobalt-platinum magnetic nanoparticles via transmetalation reactions. *J. Am. Chem. Soc.*, 123:5743. 10, 69

Philip, A. (1987). Theory of thermal relaxation of electrons in metals. *Phys. Rev. Lett.*, 59(13):1460–1463. 44

Plumer, M. L., van Lierop, J., Southern, B. W., and Whitehead, J. P. (2010). Micromagnetic simulations of interacting dipoles on an fcc lattice: application to nanoparticle assemblies. *Journal of Physics: Condensed Matter*, 22:296007. 99

Rancourt, D. G. and Daniels, J. M. (1984). Influence of unequal magnetization direction probabilities on the mössbauer spectra of superparamagnetic particles. *Phys. Rev. B*, 29(5):2410–2414. 37, 100, 117

Respaud, M., Goiran, M., Broto, J. M., Yang, F. H., Ould Ely, T., Amiens, C., and Chaudret, B. (1999). High-frequency ferromagnetic resonance on ultrafine cobalt particles. *Phys. Rev. B*, 59(6):R3934–R3937. 21

Rosei, R. and Lynch, D. W. (1972). Thermomodulation spectra of al, au, and cu. *Phys. Rev. B*, 5(10):3883–3894. 63

Schmitt, R. (2002). *Electromagnetics Explained: A Handbook for Wireless/ RF, EMC, and High-Speed Electronics (EDN Series for Design Engineers)*. Elsevier. 3

Scholl, A., Baumgarten, L., Jacquemin, R., and Eberhardt, W. (1997). Ultrafast spin dynamics of ferromagnetic thin films observed by fs spin-resolved two-photon photoemission. *Phys. Rev. Lett.*, 79(25):5146–5149. 39

Scholz, W., Suess, D., Schrefl, T., and Fidler, J. (2004). Micromagnetic simulation of magnetization reversal in small particles with surface anisotropy. *Journal of applied physics*, 95:6807–6809. 99

Stancil, D. and Prabhakar, A. (2009). *Spin Waves: Theory and Applications*. Springer Science+Business Media. viii, 2

Staunton, J. B., Ostanin, S., Razee, S. S. A., Gyorffy, B. L., Szunyogh, L., Ginatempo, B., and Bruno, E. (2004). Temperature dependent magnetic anisotropy in metallic magnets from an ab initio electronic structure theory: $l1_0$-ordered fept. *Phys. Rev. Lett.*, 93(25):257204. 49

Stoner, E. C. and Wohlfarth, E. (1948). A mechanism of magnetic hysteresis in heterogenous alloys. *Phil. Trans. Lond. Ser.A240*, pages 599–642. 11, 23, 36, 99

Suárez, C., Bron, W. E., and Juhasz, T. (1995). Dynamics and transport of electronic carriers in thin gold films. *Phys. Rev. Lett.*, 75(24):4536–4539. 44

Swendsen, R. H. and Wang, J.-S. (1987). Nonuniversal critical dynamics in monte carlo simulations. *Phys. Rev. Lett.*, 58(2):86–88. 102

Tsiantos, V., Schrefl, T., Scholz, W., Forster, H., Suess, D., Dittrich, R., and Fidler, J. (2007). Thermally activated magnetization rotation in small nanoparticles. *IEEE Transactions on Magnetics*, 39:2507–2509. 99

Tsukamoto, A. andNakagawa, K., Itoh, A., Kimel, A., Tsvetkov, A., Awano, H., Ohta, N., Kirilyuk, A., and Rasing, T. (2004). Excitation of coherent spin waves at ultrafast thermomagnetic writing. *Trans. Magn. Magn. Mat.*, 40:2543 – 2545. 96

Vaterlaus, A., Beutler, T., Guarisco, D., Lutz, M., and Meier, F. (1992). Spin-lattice relaxation in ferromagnets studied by time-resolved spin-polarized photoemission. *Phys. Rev. B*, 46(9):5280–5286. 39

Voisin, C., Christofilos, D., Del Fatti, N., Vallée, F., Prével, B., Cottancin, E., Lermé, J., Pellarin, M., and Broyer, M. (2000). Size-dependent electron-electron interactions in metal nanoparticles. *Phys. Rev. Lett.*, 85(10):2200–2203. 89

Vomir, M., Andrade, L. H. F., Guidoni, L., Beaurepaire, E., and Bigot, J.-Y. (2005). Real space trajectory of the ultrafast magnetization dynamics in ferromagnetic metals. *Phys. Rev. Lett.*, 94(23):237601. 94, 96

Weiss, P. (1907). L'hypothèse du champ moléculaire et la propriété ferromagnétique. *Journal de Physique Théorique et Appliquée*, 6:667–690. 4, 13, 16

Wernsdorfer, W., Orozco, E. B., Hasselbach, K., Benoit, A., Barbara, B., Demoncy, N., Loiseau, A., Pascard, H., and Mailly, D. (1997). Experimental evidence of the néel-brown model of magnetization reversal. *Phys. Rev. Lett.*, 78(9):1791–1794. 99

Wolf, D. (1997). *Advances in computer simulation*. Springer-Verlag Berlin Heidelberg. 101

Wolff, U. (1989). Collective monte carlo updating for spin systems. *Phys. Rev. Lett.*, 62(4):361–364. 102

You, C. Y. and Shin, S. (1998). Generalized analytic formulae for magneto-optical kerr effects. *Jornal of applied physics*, 84:541. ix, 58, 61

Zener, C. (1954). Classical theory of the temperature dependence of magnetic anisotropy energy. *Phys. Rev.*, 96(5):1335–1337. 49

Zhang, G., Hübner, W., Beaurepaire, E., and Bigot, J.-Y. (2002). *Spin Dynamics in Confine Magnetic Structures I :(laser-induced demagnetization Femtomagnetism, a new frontier?)*. Springer-Verlag Berlin Heidelberg. 46

Zhang, G. P. and Hübner, W. (2000). Laser-induced ultrafast demagnetization in ferromagnetic metals. *Phys. Rev. Lett.*, 85(14):3025–3028. 46